Ana Telma da Silva Santos

Treatments in Chronic Hepatic Encephalopathy: an *in vivo* and longitudinal Magnetic Resonance Spectroscopy study on a rat model of Biliary Cirrhosis

Dissertation presented to the University of Coimbra in fulfillment of the requirements necessary for obtaining a MSc degree in Biomedical Engineering

October 2014

· U C ·

UNIVERSIDADE DE COIMBRA

• U C •

FCTUC FACULDADE DE CIÊNCIAS
E TECNOLOGIA
UNIVERSIDADE DE COIMBRA

Ana Telma da Silva Santos

Treatments in Chronic Hepatic Encephalopathy: an *in vivo* and longitudinal Magnetic Resonance Spectroscopy study on a rat model of Biliary Cirrhosis

Dissertation presented to the University of Coimbra
in fulfillment of the requirements necessary for
obtaining a MSc degree in Biomedical Engineering

Supervisors:
Dr. Cristina Cudalbu[1]
Prof. Dr. Miguel Castelo-Branco[2]
[1]Centre d'Imagerie Biomédicale, École Polytechnique Fédérale de Lausanne, Switzerland
[2]Instituto de Imagem Biomédica e Ciências da Vida (IBILI), Faculdade de Medicina da Universidade de Coimbra (FMUC), Portugal

Coimbra, 2014

This project was developed in collaboration with:

Centre d'Imagerie Biomédicale (CIBM), École Polytechnique Fédérale de Lausanne (EPFL)

ACKNOWLEDGEMENTS

I owe my sincere gratitude to the people who are part of CIBM for having contributed, in some way, to the wonderful experience during my master's project. Gratitude and the utmost regard are owed to:

The Director, Prof. Rolf Gruetter, for allowing me to undertake this project and also for the clarifying classes on Biomedical Imaging.

My supervisor, Dr. Cristina Cudalbu, and to the PhD student, Veronika Rackayová, for their encouragement, wisdom and patience.

The veterinarian, Dr. Corina Berset, for being such an amazing professional and an extremely approachable person.

Dr. Carole Poitry-Yamate for the highest possible levels of enthusiasm and kindness.

Dr. Bernard Lanz and Dr. Nicolas Kunz for contributing with their extensive knowledge to this project.

Quero também expressar a minha gratidão para com o Prof. Miguel Castelo-Branco, por se ter disponibilizado a ser meu orientador na Universidade de Coimbra.

Ao André Morais, por toda a sua amizade e apoio ao longo da minha estadia na Suíça. Foi um prazer trabalhar contigo!

"O melhor de ir é poder voltar". Agradeço, portanto:

Às pessoas que fui conhecendo ao longo do meu percurso académico, pela sua contribuição para o meu crescimento pessoal e intelectual.

Ao Luiz, por nunca ter desistido de mim e por constantemente me fazer ver do que eu sou capaz. Por ter encurtado a distância sempre que possível e por toda a sua amizade, amor e companheirismo.

À minha família, e em especial à minha mãe, por ser o meu porto seguro e fonte de inspiração. Por me apoiar incondicionalmente e por toda a confiança depositada em mim.

RESUMO

A encefalopatia hepática é uma síndrome neuropsiquiátrica decorrente de distúrbios cerebrais induzidos por doenças do fígado. A encefalopatia hepática crónica é associada com a cirrose e é caracterizada por uma fibrose progressiva do parênquima do fígado, o que conduz à hipertensão portal e à deterioração da função do fígado. A alteração na síntese e secreção de ácidos e de outros componentes biliares contribui para a disbiose intestinal, a qual, juntamente com a hipertensão portal, altera a permeabilidade intestinal e, consequentemente, promove a translocação bacterial. A hipertensão portal, em associação com um comprometido processo de detoxificação, permite que toxinas, entre as quais amónia, passem para a circulação sistémica. O aumento de amónia em circulação, denominado hiperamonémia, é uma das principais características da encefalopatia hepática. Os probióticos surgem assim como uma possível forma de tratamento para a encefalopatia hepática, uma vez que estes previnem a translocação bacterial e reduzem a produção e consequente absorção de amónia. A encefalopatia hepática é também acompanhada por um défice cerebral de creatina e, assim, a suplementação oral com creatina emerge também como um potencial tratamento. Esta tese é baseada em estudos preliminares para avaliar o papel do VSL#3®, um *cocktail* probiótico, e da suplementação oral com creatina na neuroprotecção, em ratos com o ducto colédoco obstruído, um modelo de doença do fígado crónica. Para isso, a técnica de espectroscopia de protões por ressonância magnética foi utilizada, permitindo a análise do metabolismo cerebral, dado que a encefalopatia hepática induz alterações na osmorregulação, neurotransmissão e metabolismos antioxidante e energético cerebrais. Os nossos resultados foram promissores, demonstrando a viabilidade dos estudos e permitindo-nos melhorar o protocolo experimental para estudos futuros.

ABSTRACT

Hepatic encephalopathy is a neuropsychiatric syndrome that stems from liver disease-induced cerebral disorders. Chronic hepatic encephalopathy is associated with cirrhosis and is characterized by a progressive fibrosis of the liver parenchyma, which leads to portal hypertension and deterioration of liver function. Altered synthesis and secretion of bile acids and other biliary components contributes to gut dysbiosis that, along with portal hypertension, alters intestinal permeability and consequently promotes bacterial translocation. Portal hypertension, along with a defective detoxification process, allows intestinal toxins, namely ammonia, to bypass the liver into systemic circulation. The increased circulating ammonia, named hyperammonemia, is one of the main features of hepatic encephalopathy. Probiotics emerge, therefore, as a possible treatment strategy for hepatic encephalopathy, since they prevent bacterial translocation and reduce the production and consequent absorption of ammonia. Furthermore, hepatic encephalopathy is accompanied by a cerebral creatine deficiency and, in that sense, creatine oral supplementation may also arise as a treatment approach. This thesis is based on preliminary studies designed to assess the neuroprotective roles of VSL#3®, a probiotic cocktail, and creatine oral supplementation in bile duct-ligated rats, a model of chronic liver disease. For that purpose, proton magnetic resonance spectroscopy was performed longitudinally and the cerebral metabolism analyzed, given that hepatic encephalopathy induces alterations in cerebral osmoregulation, neurotransmission, and antioxidant and energy metabolisms. Our results were promising, showing the feasibility of the studies and opening the way to improve our experimental protocol for future studies.

ABBREVIATIONS

ADP, adenosine diphosphate

Ala, alanine

ALF, acute liver failure

Asc, ascorbate

Asp, aspartate

AST-120, spherical carbon adsorbent

ATP, adenosine triphosphate

BBB, blood-brain barrier

BDL, bile duct-ligated

cGMP, cyclic guanosine monophosphate

CHE, chronic hepatic encephalopathy

CK, creatine kinase

CLD, chronic liver disease

CNS, central nervous system

Cr, creatine

CRLB, Cramer-Rao lower bound

CsA, cyclosporin A

DON, 6-diazo-5-oxo-L-norleucine

DTI, diffusion tensor imaging

EDTA, ethylenediaminetetraacetic acid

emf, electromotive force

ESP, echo spacing

ETL, echo train length

FASTMAP, fast automatic shimming technique by mapping along projections

FOV, field of view

FSEMS, fast spin echo sequence

GABA, γ-aminobutyric acid

GEMS, gradient echo sequence

Glc, glucose

Gln, glutamine

GLT, glutamate transporter

Glu, glutamate

GPC, glycerophosphorylcholine

GS, glutamine synthetase

GSH, glutathione

HE, hepatic encephalopathy

IL, interleukin

Ins, *myo*-inositol

ISIS, image-selected *in vivo* spectroscopy

Lac, lactate

LPS, lipopolysaccharides

MARS, molecular adsorbent recirculating system

mGluR, metabotropic glutamate receptors

MPT, mitochondrial permeability transition

MRI, magnetic resonance imaging

MRS, magnetic resonance spectroscopy

MRSI, magnetic resonance spectroscopic imaging

NAA, N-acetylaspartate

NMDA, N-methyl-D-aspartate

NMR, nuclear magnetic resonance

NO, nitric oxide

OVS, outer volume suppression

PAG, phosphate-activated glutaminase

PAMP, pathogen-associated molecular pattern

PC, phosphorylcholine

PCr, phosphocreatine

PFA, paraformaldehyde

ppm, parts per million

PRESS, point-resolved spectroscopy

RARE, rapid acquisition with relaxation enhancement

RF, radio frequency

ROS, reactive oxygen species

SNAT, small neutral aminoacid transporter

SNR, signal-to-noise ratio

SPECIAL, spin echo, full intensity acquired localized

STEAM, stimulated-echo acquisition mode

Tau, taurine

tCho, choline-containing compounds

TE, echo time

TLRs, Toll-like receptors

TMS, tetramethylsilane

TNF, tumor necrosis factor

TR, repetition time

VAPOR, variable power radio frequency pulses with optimized relaxation delays

VOI, volume of interest

INDEX

CHAPTER 1

Basics of the Hepatic Encephalopathy (HE) and Treatment Strategies

1.1. Introduction to HE

Liver failure and its concomitant liver-dependent processes impairment often result in a wide range of harmful events, which affect several systems and associated functions. Among them, one can distinguish liver disease-induced cerebral disorders that collectively constitute the neuropsychiatric syndrome termed hepatic encephalopathy (HE) (Morgan et al., 2007).

According to the type of hepatic abnormality, the encephalopathy can be classified in type A, associated with acute liver failure (ALF) and resulting from severe inflammatory and/or necrotic liver disease of rapid onset; type B, associated with portacaval shunting in the absence of parenchymal liver disease, which is normally a consequence of congenital disorders; and type C, associated with chronic liver disease (CLD), i.e. cirrhosis, due to alcoholism, viral infection, biliary obstruction, drugs or toxins. Cirrhosis is the end stage of a wide range of liver diseases and is characterized by progressive fibrosis of the liver parenchyma, which leads to portal hypertension and deterioration of liver function. Portal hypertension compromises the detoxification process by allowing intestinal toxins to bypass the liver into systemic circulation through the high portal pressure-stimulated opening of embryonic venous channels (Butterworth et al., 2009). Cirrhosis is associated with a variety of complications, such as ascites and variceal hemorrhage, that together with an

increased susceptibility to infections in general, account for a high morbidity and mortality (Schuppan and Afdhal, 2008).

While an abrupt loss of hepatic function occurs in ALF and leads to a rapid deterioration in consciousness and high mortality rate, the chronic form of HE progresses slowly, accompanied principally by neuropsychiatric manifestations consisting of personality disorders, altered mood, increased irritability, altered changes in sleep/wake cycles, decline in intellectual capacity and abnormal muscle tone (Jones and Weissenborn, 1997), collectively causing a serious impact in the health-related quality of life of the patients.

Based on the characteristics of the neurologic manifestations in CLD, HE has been subdivided into minimal or covert, associated with subtle cognitive impairments of attention, response inhibition and executive function detectable only by neuropsychological and neurophysiological testing; and overt. The latter is further separated according to the duration of the neurologic manifestations into episodic, occurring over a short time span and fluctuating in severity; and persistent as a chronic clinical condition of cognitive deficits that affects social and occupational functioning. Additionally, overt HE is routinely graded according to the West Haven criteria, which assesses the severity of disease taking into account the changes of consciousness, intellectual function and behavior (Ferenci et al., 2002). The classification ranges from 1 to 4 and is linked, respectively, to mild, moderate, severe and coma status of disease.

Different types of liver disease, i.e. ALF and CLD, have different etiologies, lead to different cerebral and neurological alterations and, thus, to different forms of HE. Besides, HE can affect both the developing and adult brain in different ways. Expectedly, each mentioned situation is mediated by dissimilar pathophysiological mechanisms and, so, requires different therapeutic approaches. This thesis will be focused on the chronic hepatic encephalopathy (CHE, type C), thus enabling long-term progressive disease

studies in an adult animal model submitted to a persisting and prolonged hepatic insult.

1.1.1. Pathogenesis of HE

The pathogenesis of HE is not completely understood yet, but it seems to be a result of a complicated interplay of multiple factors and abnormalities involving gut-derived nitrogenous compounds, specifically ammonia. In fact, the gut is the main source of ammonia production (Solga, 2003) through both intestinal urease-producing bacteria, being urease a catalytic enzyme that hydrolyses urea into carbon dioxide and ammonia; and phosphate-activated glutaminase (PAG) activity in the enterocytes, which catalyzes the deamination of glutamine (Gln) to glutamate (Glu) and yields ammonia as an end product. Additionally, amino acid metabolism is also a pathway of ammonia production.

Under normal circumstances, ammonia is detoxified in the liver through the urea cycle, which is located near the portal vessels as first line of defense and converts ammonia to urea prior to renal excretion, thus maintaining circulating concentrations of ammonia within 35 – 65 μM (Rose, 2014). In patients with cirrhosis, the metabolic capacity of the liver is exceeded giving rise to an increase of circulating ammonia, named hyperammonemia, which is a major and commonly observed feature of HE. Glutamine synthetase (GS), which is present in muscle, kidney, liver and brain, tries to compensate for this dysfunction by catalyzing the condensation of Glu and the surplus ammonia, forming Gln (Figure 1).

Besides the neurotoxic effects that arise from brain tissue exposure to ammonia, some of which are related to Gln, other cirrhosis-induced noxious events, such as systemic inflammation, seem to contribute and/or exacerbate the manifestations of HE.

Several interactive metabolic and signaling axes exist and physiologically connect gut, liver, muscle and brain through neurotransmitters, bile acids, short chain fatty acids, choline degradation products, aromatic acids and phenolics, inflammatory mediated lipids and endocannabinoids (Holmes et al., 2012), supporting the notion of HE as a multifactorial disease, but also offering up a series of potential targets for therapeutic interventions.

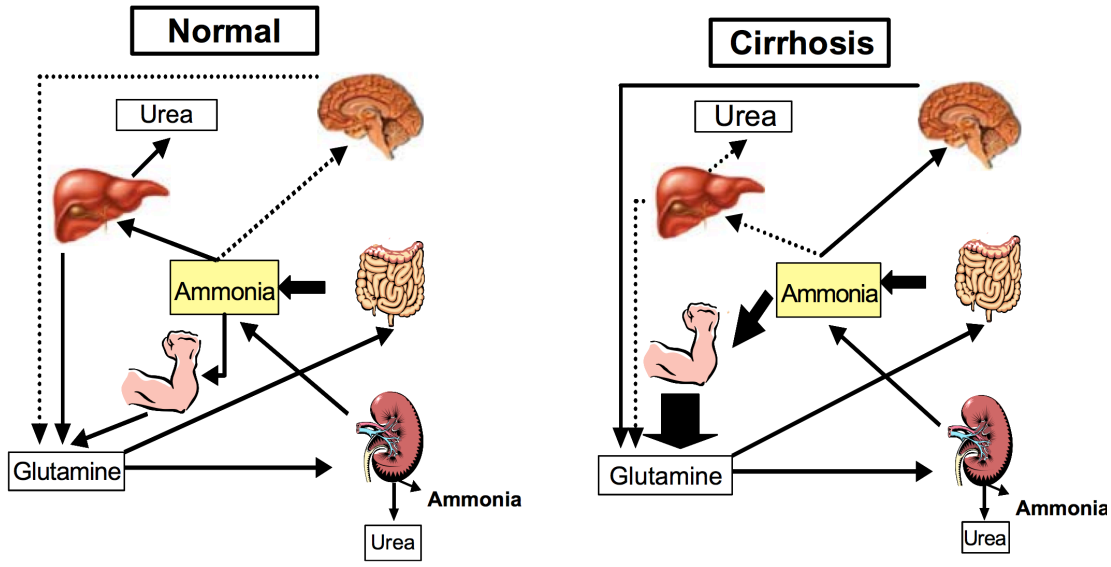

Figure 1 - Inter-organ trafficking of ammonia in healthy individuals and in patients with cirrhosis. Under healthy conditions, ammonia is mainly detoxified in the liver, but also in the muscle and, to a lesser extent, in brain. In patients with cirrhosis, the metabolic capacity of the liver is exceeded, resulting in an increase in circulating ammonia. Under these circumstances, the surplus ammonia is mainly detoxified in muscle, but also in brain and, to a lesser extent, in the liver, with the production of glutamine (Gln); this is in turn broken down to ammonia by phosphate-activated glutaminase (PAG) in enterocytes or else excreted by kidneys as ammonia. Figure taken from Morgan et al. (2007).

1.1.1.1. In the Brain

The blood-brain barrier (BBB) is the largest physical and metabolic barrier between periphery and the brain and helps regulate brain homeostasis

and protects it from endogenous and exogenous toxins arising from systemic circulation. However, BBB is easily crossed by ammonia, either by diffusion of its gaseous form (NH_3), or through potassium (K^+) channels crossing of its ionic form (ammonium, NH_4^+). At physiological pH, more than 98% of ammonia is present as NH_4^+ (Rose, 2014). Under hyperammonemia, the incorporation of blood-borne ammonia, in addition to the one derived from endogenous reactions, into the amide position of Gln is largely confined to astrocytes and represents the main route of central nervous system (CNS) ammonia removal (Brusilow et al., 2010).

Accordingly, in the setting of HE and unlike most neurodegenerative diseases, astrocytes rather than neurons primarily exhibit critical morphological and functional alterations, with both astrocyte swelling and Alzheimer type II astrocytosis being the hallmarks of the disease. However, functional derangements of astrocytes can lead to neuronal abnormalities, since astrocytes are highly regulated cells, which communicate directly with neurons and participate in neurotransmitter processing, regulation of the ionic milieu in the brain and substrate provision for neurons. Notably, the Gln-Glu cycle, whose role is to recycle the Glu that has been released from neurons, thus avoiding neuron excitotoxicity, is performed between GS, specifically found in astrocytes, and PAG, primarily found in neurons (Rama Rao et al., 2012). Furthermore, astrocytes' feet line BBB and uptake of substances from the blood into the brain requires transastrocytic transport. Thus, systemic-derived ammonia entering the brain is readily converted to Gln in astrocytes, confirmed by the increased brain levels of Gln that have been reported, which seem to correlate better with the severity of HE than plasma ammonia concentration (Laubenberger et al., 1997).

Gln is a neutral and electrophysiological inert but osmotically active amino acid, and although it is generally believed to be innocuous, it is indeed the precursor of several deleterious effects induced by ammonia in the CNS in HE, namely astrocyte swelling and consequent cerebral edema. Although

there is not a consensus on how Gln exerts its toxicity on astrocytes, one can mention three well-accepted hypotheses to explain it.

According to the Trojan Horse Hypothesis (Albrecht and Norenberg, 2006), Gln enters astrocyte mitochondria via the Small Neutral Aminoacid Transporter (SNAT), a process potentiated by ammonia, being hydrolyzed by PAG, which is located in the inner mitochondrial membrane, yielding Glu and ammonia. The generation of high levels of ammonia can lead to an excessive production of reactive oxygen species (ROS) and, consequently, induction of the mitochondrial permeability transition (MPT), resulting in mitochondrial dysfunction. The ensuing mitochondrial dysfunction leads to the impairment of the sodium (Na^+) pump, resulting in the influx of Na^+ and obliged water (Norenberg et al., 2005). In support of this theory, the blockage of the Gln transport into mitochondria and its hydrolysis by, respectively, L-histidine and 6-diazo-5-oxo-L-norleucine (DON) markedly attenuated the noxious effects of ammonia. Accordingly, cyclosporin A (CsA), an inhibitor of MTP, and the use o antioxidants abrogated the ammonia-induced astrocyte swelling, which suggests MTP and oxidative stress as key factors in its cause. However, the presence of PAG in astrocytes *in vivo* is still not clear.

The increased brain levels of Gln followed by a decrease of *myo*-inositol (Ins) represent a common pattern observed in cirrhotic patients with HE using the proton magnetic resonance spectroscopy (^{1}H MRS) technique (Shawcross et al., 2004; Cudalbu, 2013). This pattern can be explained based on the Glutamine Hypothesis, which proposes that the accumulation of Gln in astrocytes causes changes in brain osmolarity resulting in cell swelling and brain edema. The activation of osmoregulatory mechanisms induces the release of osmolytes, such as Ins, taurine (Tau) and choline-containing compounds (total choline, tCho) (Brusilow et al., 2010). However, the cerebral edema is usually less pronounced in CLD patients compared to the ALF group, implicating not only the several-fold increase of brain Gln concentrations but also the duration of this increase on the development of

brain edema. In an initial phase, a very pronounced osmotic stress occurs in the astrocytes due to increased Gln synthesis in these cells, similarly to what follows acute hyperammonemia. However, with time in the chronically hyperammonemic patients, there is a gradual compensation as reflected by a diminution in other osmolytes. This compensation is accompanied by increased water in the extracellular space; however, astrocyte swelling remains even in chronic hyperammonemia, as a consequence of an incomplete osmoregulatory effect.

Under normal conditions, a significant proportion of newly synthesized Gln rapidly leaves astrocytes, both by diffusion and by specific Gln transporters (mainly the N/A-system transporter SNAT3 and SNAT5, formerly known, respectively, as SN1 and SN2). The Transporter Hypothesis postulates that the increased Gln synthesis coupled with a partial suppression of SNAT3 and SNAT5-mediated efflux of Gln from astrocytes observed in acute hyperammonemic rat studies (Kanamori and Ross, 2005; Desjardins et al., 2012), result in an accumulation of Gln in the astrocytic compartment, which originates an osmotic stress. However, since astrocytes are the major source of extracellular Gln in brain, a commensurate reduction of brain extracellular levels of Gln does not occur as expected according to this hypothesis.

Since all the hypotheses have its advantages and drawbacks, a combination of mechanisms seem to be behind the action of Gln in the CNS. It is, however, noteworthy that in the absence of irreversible cerebral edema, HE symptoms in adults are largely reversible when ammonia returns to normal levels, a fact that, apparently, can only be explained by the glutamine hypothesis.

Other clinical observations possibly involved in the pathogenesis of HE are decreased serum levels of branched-chain amino acids and increased levels of aromatic amino acids. The principal neuroinhibitory neurotransmitter, γ-aminobutyric acid (GABA), is also increased in the

cerebral spinal fluid of patients with encephalopathy. Other toxins identified in the CNS include increased levels of endogenous benzodiazepine-like compounds, ROS, nitric oxide (NO) and inflammatory cytokines, and a depletion of endogenous antioxidants is also observed.

1.1.1.2. In the Gut

Although the recognition of the relationship between hepatic coma and the absorption of nitrogenous substances from the intestine emerged in the middle of the last century (Phillips et al., 1952), it took until the last few years for the symbiotic relationship between the mammalian host and its gut microbial community, i.e. gut microbiota, to gain a tremendous research interest.

The composition and activity of the gut microbiota codevelop with the host continually through lifetime, varies topographical and temporally, and is influenced by extrinsic factors, with particular bacterial species occupying specific niches in the body habitat or being associated with particular growth or maturation phases of the host. The microbiota of infants is seeded at birth and seems to be influenced by a variety of factors, such as method of delivery, breast or bottle-feeding and epigenetics. Subsequent modulation of the microbial landscape is then driven by a series of complex and dynamic interactions throughout life, including diet, life-style, disease, antibiotic use and the mammalian host genome that together shape a series of unique habitats within and between individuals.

The intimate coevolution of the microbiota with their mammalian hosts has resulted in an interlocked mutually beneficial relationship with the microbiota controlling or contributing to essential host functions such as harvesting energy, shaping the host immune system, metabolism of xenobiotics (compounds of nonhost origin that enter the gut with the diet or are produced by the microbiota), and metabolic signaling, and, thus,

collectively providing critical biosynthetic pathways that significantly extend host metabolic capacity. The developmental trajectory of the microbiome, incorporating the microbes and their collective genomes, modulates the metabolic phenotype of the host and greatly influences host biochemistry and susceptibility to disease. The changing relationships between the microbiome and host biochemistry during development also offers a series of interventional windows that can be aligned with disease prevention during early life and treatment of specific conditions later in life (Nicholson et al., 2012).

A close anatomic and functional relationship between liver and gut originate the gut-liver axis, with the intestine supplying the major part of the blood to the liver through the portal vein, which carries various toxic compounds such as bacteria and their derivatives, including ammonia, to be filtrated. In return, liver secretes bile acids to the intestine and modulates its activity.

Under healthy conditions, microbiota is predominantly constituted by gram-negative bacteria and anaerobes, which are estimated to be 100 to 1000 times more than aerobic ones. Anaerobic species have a critical role in producing short-chain fatty acids that reduce colonic inflammation and nourish colonocytes, limiting the growth and colonization of pathogen bacteria through the competition for nutrients, adhesion to intestinal mucosa and production of anti-bacterial peptides (Bajaj et al., 2014).

Any disruption in the amount and composition of gut microbiota can result in a disturbance to the intestinal homeostasis and lead to gut dysbiosis, where potentially hostile microbes proliferate at the expense of normal commensal and symbiont microbes. In the context of cirrhosis, altered synthesis and secretion of bile acids and other biliary components together with abnormal intestinal motility may explain this imbalance.

Bacterial overgrowth interferes with intestinal permeability through the increased synthesis of NO, which leads to an impaired intestinal structure

due to oxidative stress, and the high concentration of toxic acetaldehyde produced via metabolism of ethanol (Imani Fooladi et al., 2013). Additionally, portal hypertension influences intestinal permeability by decreasing the thickness of mucosa, one of the constituents of intestinal wall. An impaired intestinal permeability allows bacterial translocation, i.e. the migration of bacteria and/or their products from the intestinal lumen to mesenteric lymph. As a consequence of intestinal bacterial overgrowth, impaired host defenses, and/or disruption of the gut mucosal barrier, some gram-negative species belonged to enterobacteriaceae, enterococci and streptococci families, especially some strains of *Escherichia coli* adhere to the mucosal surface of intestinal walls and pass across them efficiently.

Thus, a release of bacterial endotoxins occurs, mainly consisting of lipopolysaccharides (LPS), together with flagellin, peptidoglycan and microbial nucleic acids, collectively termed as pathogen-associated molecular patterns (PAMPs). Through the portal blood flow draining the gastrointestinal tract, intestinal bacteria and bacterial products, such as LPS, reach the liver for filtration; the increase in PAMPs and accumulation of metabolites in the liver can cause liver harm. This happens through the recognition of PAMPs by Toll-like receptors (TLRs) expressed on the kupffer cells, the resident macrophages of the liver, thus modulating kupffer cells' activity and cytokine production and causing inflammation stimulation and oxidative damage in the liver (Figure 2.a.). Proinflammatory cytokines such as interleukin (IL)-1β, tumor necrosis factor (TNF)-α and IL-6 modulate the cerebral effect of ammonia and there is mounting evidence that systemic inflammation results in exacerbation of the symptoms of HE in cirrhotic patients across all grades of HE (Tranah et al., 2013). Thus, proinflammatory mechanisms may act synergistically with ammonia in producing cognitive impairment of varying degree.

Therefore, gut microbiota represents a more recently discovered target on the treatment of HE, by the manipulation of its composition to benefit

host health. A better understanding of how interindividual variation in microbial composition contribute to disease risk or health sustainability may point to new therapeutic interventions and disease prevention strategies (Holmes et al., 2012).

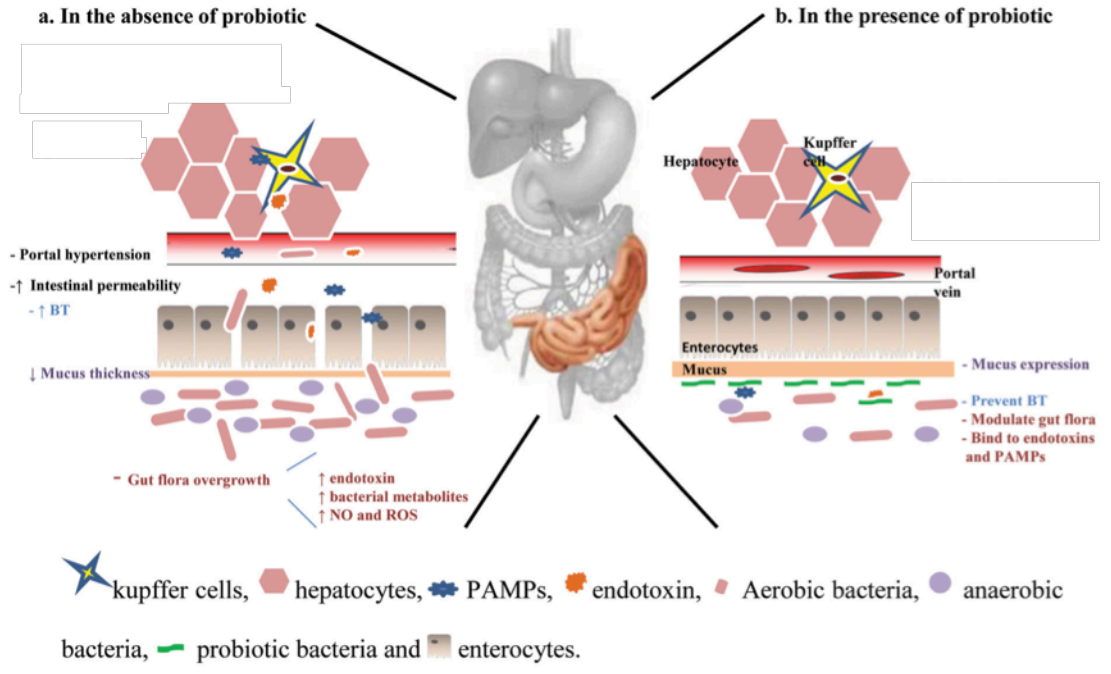

Figure 2 – a. Schematic illustration of multifarious mechanisms involved in liver diseases and **b.** probiotic influences on them. The intestinal mucosa functions as the local defense barrier that helps to prevent the invasion and systemic spread of bacteria and endotoxins, which are mostly LPS from the cell walls of gram-negative bacteria. However, under certain conditions, intestinal barrier function can be impaired or overwhelmed, allowing bacteria and endotoxins within the gastrointestinal tract to reach systemic organs and tissues, a process termed bacterial translocation. The liver is an important site for bacterial phagocytosis and clearance as it contains the largest population of tissue macrophages. Activated kupffer cells exposed to pro-inflammatory mediators, such as LPS or other bacterial products, are the major source of inflammatory mediators including pro-inflammatory cytokines, chemokines and reactive oxygen/nitrogen species, which contribute to liver injury. Through pattern recognition receptors, including TLRs, the innate immune system recognizes conserved PAMPs. The beneficial effect of probiotics relies in the reduction of pathogenic bacteria through the competitive inhibition and in the improvement of nutritional status of gut epithelium, thus preventing bacterial translocation. BT: bacterial translocation; NO: nitric oxide; ROS: reactive oxygen species; PAMPs: pathogen-associated molecular patterns. Figure modified from Imani Fooladi et al. (2013).

1.2. Treatment Options for HE

To date, the available HE treatment options are limited to correct or remove precipitating causes, dietary changes and pharmacologic approaches. Surgical techniques and liver transplant arise as the ultimate and, if possible, avoidable ways of treatment, taking into account their invasiveness and, in the case of liver transplant, also the lack of organs donation.

The prompt identification and correction of precipitating factors can prevent the deterioration of hepatocellular function, emerging as a beneficial approach for most episodes of HE, since it is potentially caused by reversible factors, such as infection, diuretic overdose and hemorrhage.

In addition to HE, malnutrition is a common complication of cirrhosis, marked by loss of skeletal mass. As it was mentioned above muscle tissue plays an important role in removing the circulating ammonia and, in that context, optimizing nutritional status is crucial. The recent consensus achieved by the members of the International Society for Hepatic Encephalopathy and Nitrogen Metabolism (ISHEN) provides several guidelines on the nutritional management of HE in patients with cirrhosis (Amodio et al., 2013). Generally, one can detach the timing of caloric ingestion, with the advise of taking small, frequent meals, evenly distributed throughout the day, in order to avoid the utilization of amino acids for glucose (Glc) production since it depletes tissue protein stores and produces ammonia. Furthermore, the ingestion of proteins is recommended, with vegetable proteins being preferred over meat and fish ones. Among other reasons, vegetable protein diets contain significantly more dietary fiber than isonitrogenous meat protein ones, and a high fiber diet may be beneficial for HE patients by decreasing gastrointestinal transit time, reducing intraluminal pH and increasing fecal ammonia excretion. The mechanism of action and efficacy of additional dietary supplements, namely probiotics and creatine (Cr), which are the motivations of this thesis, will be further discussed below.

Although some general rules on the dietary modulation can be established, mainly based on its efficacy on a few studies and on previous disease knowledge, the guidance of dietary changes should be directed to each individual, based on the assessment of body composition, in order to unveil the specific needs of each patient, that can, for instance, range from depletion to weight gain.

Few of the pharmacological agents used to treat HE, at the present time, have been subject to rigorous evaluation by way of placebo-controlled trials. Additionally, most of the studies lacked standard definitions and grading scales of HE and included small samples sizes. Despite these limitations, the treatment of HE is generally aimed at decreasing and/or modifying the production and absorption of intestinal toxins, mainly ammonia, either by stimulating its detoxification, adsorbing it or altering the bacterial flora. Furthermore, oral supplementation of branched-chain amino acids and micronutrients, as well as pharmacological normalization of the neurotransmission system can resolve several abnormalities and symptoms during the disease. Non-absorbable disaccharides and non-absorbable or poorly absorbed antibiotics are the most widely used agents. However, treatment with non-absorbable disaccharides, most commonly lactulose, is limited by side effects and narrow therapeutic window and, consequently, the compliance with the treatment may be suboptimal. On the other hand, non-absorbable or poorly absorbed antibiotics, especially rifaximin, have fewer side effects, but costs, at least in the short-term, are high and long-term safety is undetermined. Hence, potentially new agents, namely probiotics, are emerging and their efficacy being tested.

1.2.1. Prebiotics, Probiotics and Synbiotics

Prebiotics, probiotics and synbiotics are functional food components that modulate gut microbiota to benefit host well-being and health. A meta-

-analysis performed by Shukla and colleagues and the only comparing the effects of gut flora modulation using prebiotics, probiotics and synbiotics on minimal HE showed that, although a significant improvement stemmed from all of the treatments, lactulose, a non-absorbable disaccharide and classified by some as prebiotic, appeared to have the most beneficial effect, followed closely by probiotics and synbiotics (Shukla et al., 2011).

Prebiotics are non-digestible food ingredients that are selectively metabolized by colonic bacteria that have the capacity to improve health, thus allowing specific changes in both the composition and/or activity of the gastrointestinal microbiota (Manning and Gibson, 2004). Currently, non-absorbable disaccharides, especially lactulose, represent the most widely used prebiotics on the treatment of HE.

The beneficial effect exerted by the non-absorbable disaccharides is due to a reduction of the ammonia intestinal production by coliform bacteria and of its consequent absorption, mainly through a cathartic effect and gastrointestinal tract acidification. However, side effects like diarrhea, abdominal bloating and low Na+ levels are common. As its name implies, these disaccharides are not absorbed in the small intestine, passing intact into the large intestine where they are metabolized by colonic bacteria. Among non-absorbable disaccharides one can distinguish lactulose (β-galactosidofructose) and lactilol (β-galactosidosorbitol) as standard pharmacological agents for the treatment of HE, with the former being the first line pharmacological treatment for this condition (Blei and Cordoba, 2001).

Als-Nielsen and colleagues performed a systematic review on the efficacy of non-absorbable disaccharides for HE, where they included randomized controlled trials that assessed lactulose or lactilol *versus* placebo, no treatment, or antibiotics, for a median treatment duration of 15 days, in cirrhotic patients with overt HE. Although low quality trials were included, from the high quality ones they were able to conclude that they "did not find

sufficient evidence to determine whether lactulose or lactilol have a significant beneficial effect in patients with hepatic encephalopathy" (Als-Nielsen et al., 2004b). More recently, Gluud and colleagues were able to update this review by adding randomized controlled trials assessing the effect of lactulose *versus* no intervention, which were performed in the meantime, proving the beneficial effects of lactulose and lactilol on the improvement of manifestations of HE and prevention of clinically overt HE and thereby supporting the use of non-absorbable disaccharides in clinical practice (Gluud et al., 2013b).

Probiotics are live microorganisms that, when administered in adequate amounts, confer a health benefit on the host. Many probiotic species are used for the production of fermented food and have been consumed safely as part of these foods for millennia. Furthermore, many bifidobacteria and lactobacilli species are normal, nonpathogenic inhabitants of the human gastrointestinal tract, oral cavity, skin, and, in women, of the vagina (Sanders, 2003).

Besides improving host health, probiotics must be safe, persist on the gastrointestinal tract long enough to elicit an effect and should be amenable to and remain viable during the production and storage processes. Probiotics exert their beneficial effects in the treatment of HE at multiple levels, namely by decreasing the production and absorption of ammonia and increasing the hepatic clearance of ammonia and other toxins. While the first effect is achieved through a reduction of bacterial urease activity through the competitive inhibition, the second stems from a decrease in both intestinal pH and permeability through the improvement of nutritional status of gut epithelium. The latter effect is originated by a diminution of both inflammation and oxidative stress in hepatocytes (Figure 2.b.). Additionally, there are various probiotic strains that can help remove several nitrogenous waste products and uremic toxins from the gastrointestinal tract and the blood stream, which are utilized as nutrients for microbes' growth. Thereby,

microbial load increases, thus generating a greater potential for diffusion of the uremic toxins from systemic circulation through the intestinal walls into the gut. Collectively, probiotics consumption lowers circulating ammonia concentration and attenuates its consequent deleterious effects.

Presently, the clinical use of probiotics for patients with HE can not be recommended mainly because of two reasons: current evidence suggest that most trials evaluating the role of probiotics in the treatment of HE are of not high quality and have high risk of both systematic and random errors (McGee et al., 2011); and the concerns about the probiotics treatment safety with immunocompromised individuals and patients exhibiting pre-existing digestive lesions/syndromes, who may, in theory, be more vulnerable to the translocation of bacteria from the gut lumen. However, clinical studies have indicated already that a wild spectrum of probiotics can be consumed safely in patients with various gastrointestinal diseases (Chermesh and Eliakim, 2006) and immunocompromised conditions (Homayouni Rad et al., 2013). In fact, there is evidence that probiotics represent a safer, better tolerated (Ding et al., 2014) and perhaps less expensive therapy, in comparison with disaccharides and antibiotics, and thus more appropriated for long-term use in CHE. It is, however, noteworthy, that experimentation on the efficacy and safety of probiotics is limited compared with the available literature on lactulose and rifaximin. Additionally, the types and dosages of probiotics used in trials have been variable (Shukla et al., 2014), which may critically influence the results from study to study, since properties and effective actions of each probiotic are unique. Therefore, and taking into account one of the aims of this thesis, one must focus on the probiotic strains that collectively compose the VSL#3®.

VSL#3® is a probiotic cocktail comprised of eight different lyophilized bacterial cultures, among which four belong to the genus *Lactobacillus*, three belong to the genus *Bifidobacterium* and one is a strain of *Streptococcus thermophilus*. The strains present in VSL#3® are non-pathogenic, non-

-toxigenic bacteria and their survival and growth in the environment is not favorite, since they are asporogenes, facultative anaerobic bacteria, with high nutritional requirements. Additionally, by being gram-positive organisms, these bacteria do not produce endotoxins.

Lactobacillus acidophilus is a normal inhabitant of the human gastrointestinal tract and has a safe history of use in foods in fermented milks and probiotics since 1950. *Lactobacillus plantarum* is a normal inhabitant of plant material, which is routinely isolated from silage of fermented vegetables and has a safe history of use in food since 1965. *Lactobacillus paracasei* was firstly isolated from cheddar cheese and has a safe history of use in food as a dairy starter culture since 1970. *Lactobacillus delbrueckii* subsp. *bulgaricus* was firstly isolated from cheddar cheese and has a safe history of use in food as a dairy started culture since 1970. *Bifidobacterium infantis* has a safe history of use in fermented milks and infant formulas since 1980 (Mountzouris et al., 2002). *Bifidobacterium longum* was firstly isolated from the intestines of a human adult and has been commercialized as a probiotic in yoghurts and dietary supplements for more than fifteen years. *Bifidobacterium breve* is a normal inhabitant of the human gastrointestinal tract and has a safe history use in fermented milks and infant formula since 1980 (Sanders, 2003). *Streptococcus thermophilus* is the principal component of the natural flora of yoghurt and certain cheese types (Brigidi et al., 2003) and has a documented history of use in food since 1930.

So far, some studies in humans have assessed the efficacy of VSL#3® on the treatment of HE. It has been shown that VSL#3® is effective in treating patients to prevent development of a first episode of HE, i.e. primary prophylaxis, and in preventing its recurrence in patients who had a previous episode of HE, i.e. secondary prophylaxis. To obtain the former result, Lunia and colleagues performed a single-center, prospective, open-labeled randomized trial in 160 cirrhotic patients and compared the efficacy of VSL#3® with placebo during a three-month period, through the evaluation of

hepatic and intestinal function (Lunia et al., 2014). Concerning the proven efficacy of VSL#3® on the secondary prophylaxis, Dhiman and colleagues performed a double blind, randomized, placebo controlled study during a six-month period and assessed the hospitalizations for overall complications of liver cirrhosis and for those involving HE, hepatic function and blood cytokine levels (Dhiman, 2013).

On the other hand, although the efficacy of VSL#3® on the treatment of HE has not ever been tested in animal models, studies on certain beneficial mechanisms of action of VSL#3® in rats have been performed. Sánchez and colleagues demonstrated that VSL#3® probiotic treatment decreases bacterial translocation, the pro-inflammatory state, with reduction of serum TNF-α and ascites formation in rats with carbon tetrachloride-induced cirrhosis. For that, a group of adult male Sprague-Dawley rats drank an approximate dose of 12.8 billion bacteria per kilogram of rat body weight with the treatment beginning at six weeks after the cirrhosis induction and during an average of 8.6 weeks. The results were compared with two other groups treated with water: one composed of cirrhotic and another of non-cirrhotic rats (control) (Sanchez et al., 2014). In addition, Chang and colleagues showed that VSL#3® exerts a protective effect on intestinal permeability using a wild type rat model of acute alcoholic intestinal injury. For that, they assessed the expression of proteins that compose tight junctions, which connect gut epithelial cells and so prevent the bacterial translocation**,** and plasma levels of endotoxins and TNF-α. The comparison was made between a control group of adult rats, a group to which only alcohol was given and others treated either with VSL#3®, Gln, or the combination of both, or placebo, being Gln the traditional agent used on the treatment of such pathology (Chang et al., 2013). Another study with bile duct-ligated (BDL) adult male Wistar rats, a model of CLD and the one that will be used on this thesis, showed that VSL#3® prevents endothelial dysfunction, an abnormality caused by portal hypertension and consequent oxidative stress and to which bacterial

translocation seems to play a role. In that sense, a group of rats was treated with VSL#3® in a daily dose of 50 billion bacteria per kilogram of rat body weight, since three weeks before the cirrhosis induction and during seven weeks. This group was compared with a sham group receiving VSL#3® and also with another two control groups: a BDL and a sham groups, both receiving vehicle (Rashid et al., 2014).

Synbiotics, i.e. the mixture of pre- and one or more probiotic strains, also appear as a promisor option for the management of HE. Knowing the beneficial effects of both prebiotics, especially lactulose, and probiotics, a combination of them may provide a synergistic or additive effect towards removal of ammonia and other nitrogenous wastes from the gut and blood stream (Sekhar et al., 2013).

1.2.2. Non-absorbable Antibiotics

By altering the gastrointestinal flora through a reduction of the urease-producing bacteria, certain oral antibiotics can decrease the production and, consequently, the absorption of ammonia. In addition to patients that are symptomatic on non-absorbable disaccharides and due to its extreme sweet taste, non-absorbable disaccharides can not be well tolerated in the longer-term giving rise to antibiotics used as second agents on the treatment of HE. As with antibiotics in general, the disadvantage of its prolonged use is the emergence of multiresistant organisms. One solution might be the administration of antibiotics and probiotics alternately (Lighthouse et al., 2004).

The proven efficacy and safety of rifaximin, a synthetic and also poorly absorbed antibiotic used as first line therapy in several countries in Europe, Asia, Africa and Latin America, make it the actual option with the highest benefit–risk ratio for treating HE (Morgan et al., 2007). However, its costs

remain an important concern, limiting its long-term and/or larger patient populations use.

The meta-analysis on non-absorbable disaccharides for the treatment of HE included five trials testing the efficacy of rifaximin *versus* lactulose or lactilol in cirrhotic patients with overt HE, over a median treatment duration of fifteen days (Als-Nielsen et al., 2004b). Rifaximin administration resulted in a beneficial effect on HE manifestations, which was further confirmed by two randomized controlled trials in cirrhotic patients with minimal HE for a rifaximin treatment lasting eight weeks (Bajaj et al., 2011; Sidhu et al., 2011). Furthermore, a large high quality randomized controlled trial evaluated the longer-term effect of rifaximin administration *versus* placebo, during six months (Bass et al., 2010; Sanyal et al., 2011). It included cirrhotic patients who had at least two episodes of overt HE during the previous six months and 91% of the patients received lactulose at baseline. Compared with placebo, rifaximin reduced the risk of HE and improved the quality of life, supporting its use in clinical practice and raising the interest on a treatment modality combining lactulose and rifaximin.

Although not widely used for the treatment of HE mainly due to the limited studies performed, discouraging previous results and/or adverse effects found, one can also designate other antibiotic types: neomycin, ribostamycin, vancomycin and paromomycin (aminoglycosides), metronidazole and nitazoxanide.

1.2.3. Creatine (Cr)

The system comprising Cr, phosphocreatine (PCr) and creatine kinase (CK) is essential to maintain the high energy levels necessary for CNS development and functions, since its principal roles are the regeneration and cell buffering of adenosine triphosphate (ATP). In addition, Cr is important for dendritic and axonal elongation (growth cone migration), Na^+-K^+-ATPase

activity, neurotransmitters release, maintenance of membrane potential, calcium (Ca^{2+}) homeostasis, and restoration of ion gradients in CNS. There is also evidence for Cr to act as a true neurotransmitter (Almeida et al., 2006), antioxidant (Sestili et al., 2011) and one of the main CNS osmolytes (Bothwell et al., 2002).

The potential neuroprotective effect of Cr in HE has been studied using an *in vitro* model of cultured embryonic rat brain cell aggregates exposed to NH_4^+. Braissant and colleagues were able to demonstrate that ammonia exposure to developing brain cells impairs axonal and dendritic growth, accompanied by a Cr deficiency. The adding of Cr to the culture medium partially prevented the impairment of axonal growth in a glial-dependent manner (Braissant et al., 2002).

Although ammonia-induced neurotoxicity was not observed after axonal maturation supporting the fact that ammonia does not induce irreversible damage to CNS in adults, Cr has also been found decreased in adult BDL rats (see below), possible due to an osmoregulatory mechanism. In addition, Cr has been shown to exert protective effects in various degenerative processes, including Huntington and Parkinson diseases, amyotrophic lateral sclerosis or cerebral ischemia (Klein and Ferrante, 2007).

Under physiological conditions in adults, BBB is low permeable for Cr bloodstream taking up, partly because astrocytes do not express SLC6A8, the Cr specific transporter. However, astrocytic SLC6A8 expression seems to be induced by NH_4^+ exposure (Braissant et al., 2008). Thus, oral Cr supplementation should be considered as a therapeutic option for HE.

1.2.4. Branched-Chain Amino Acids

The low plasmatic levels of branched-chain amino acids (valine, leucine and isoleucine) observed in patients with advanced liver disease raised the interest in their oral supplementation as a potential treatment for

HE. Under hyperammonemic circumstances, the degradation of branched-chain amino acids is promoted by the stimulation of Gln synthesis, which induces the cerebral afflux of aromatic amino acids, since there is a competition between branched-chain amino acids and aromatic amino acids for the transporter at the BBB. Consequently, a disturbance of neurotransmitter synthesis may occur. Besides the reversal of the deleterious events that may arise from its deficiency, supplements with branched-chain amino acids potentiate several cerebral, metabolic and nutritional positive effects that may benefit patients with HE (Tajiri and Shimizu, 2013). In fact, Gluud and colleagues concluded in a systematic review with meta-analyses of randomized controlled trials in cirrhotic patients with recurrent minimal or overt HE that oral branched-chain amino acids supplements improve manifestations of HE but have no effect on mortality, through comparison with control supplements or placebo (Gluud et al., 2013a).

1.2.5. Supplementation of Micronutrients

Zinc deficiency is frequently observed in patients with CLD and may explain a number of abnormalities that have been reported in that condition, namely immune dysfunction. Oral zinc supplementation arises therefore as a solution to correct zinc deficiency, which is associated with an impaired nitrogen metabolism by decreasing the activity of urea cycle enzymes in the liver and GS in muscle that are zinc-dependent. Chavez-Tapia and colleagues performed a meta-analysis on the use of oral zinc in the treatment of cirrhotic patients with different stages of HE and found a neuropsychological melioration, without evident improvement on HE or HE-related quality of life (Chavez-Tapia et al., 2013).

Furthermore, low circulating levels of Na^+ can alter brain function both directly or by interacting with the mechanisms causing HE, and is recognized as a risk factor for the development of HE. Moreover, and not directly

implicated in the pathophysiology of HE, deficiencies of the water-soluble vitamins, particularly thiamine, are associated with a wide range of neuropsychiatric symptoms. In addition, changes in circulating levels of Ca^{2+}, magnesium and iron can produce changes in the mental function, ranging from confusion to coma or secondary dementia. Therefore, the levels of these micronutrients must be controlled and orally supplemented, if needed (Amodio et al., 2013).

1.2.6. L-Ornithine Phenylacetate, Sodium Benzoate and Sodium Phenylacetate

L-ornithine phenylacetate, sodium benzoate and sodium phenylacetate are used in the treatment of urea cycle enzyme deficiencies since they metabolically fix ammonia by utilizing alternative pathways for waste nitrogen excretion. While L-ornithine acts as a substrate for Gln synthesis from ammonia in skeletal muscle, phenylacetate and benzoate conjugate, respectively, with Gln and glycine, and both end products are excreted by kidneys. Thereby, these therapies may not be appropriated for patients with significant fluid retention or kidney dysfunction because of the kidneys' role on excretion and the significant dose-dependent Na^{+} content in the case of sodium benzoate and sodium phenylacetate.

A recent study with BDL rats provided new insights into the mechanism of action of L-ornithine phenylacetate by showing that this compound reduces plasma ammonia by modulating muscle GS and gut PAG activities, which seem to be, respectively, decreased and increased in hyperammonemia (Jover-Cobos et al., 2014). Additionally, in consequence of the ammonia lowering, L-ornithine phenylacetate reduced the systemic and brain inflammation in BDL rats (Balasubramaniyan et al., 2012; Wright et al., 2012). Although it seems to be safe when administered to patients with

compensated and decompensated cirrhosis (Jover-Cobos et al., 2013), there is a lack of clinical trials to prove its efficacy on HE.

A study with eight cirrhotic patients with chronic stable HE demonstrated that, although sodium benzoate may be superior to sodium phenylacetate when added to a diet restriction and neomycin or lactulose, the combination of both agents might be better than either agent used alone. A non-controlled trial evaluating the efficacy and safety of a six-month administration of sodium benzoate in eighteen patients with CHE have shown improvements in their condition, although the score used to assess HE is no longer in use (Misel et al., 2013). Adverse effects like gastrointestinal symptoms are among the most reported during sodium benzoate utilization.

1.2.7. L-Ornithine-L-Aspartate

Lowering of ammonia through the stimulation of Gln synthesis and ureagenesis, the key metabolic pathways for ammonia detoxification, is the mechanism of action of L-Ornithine-L-Aspartate, a salt of the amino acids ornithine and aspartate (Asp). With a low incidence of side effects except for mild gastrointestinal disturbances, the administration of L-Ornithine-L-Aspartate has resulted in a more prominent improvement of HE and reduction of serum ammonia compared to placebo/no-intervention in cirrhotic patients with minimal and overt HE (Bai et al., 2013).

1.2.8. L-Carnitine

Therrien and colleagues performed a study on portacaval-shunted rats, where a protective effect of L-carnitine on ammonia-precipitated encephalopathy was evident (Therrien et al., 1997).

Up to date, almost all the randomized controlled trials evaluating the efficacy and safety of acetyl-L-carnitine, the acetylated form of L-carnitine,

on the treatment of HE were carried in a single center, in Italy, and an improvement in the quality of life, anxiety, depression (Malaguarnera et al., 2011) and cognitive functions (Malaguarnera et al., 2008) accompanied by a reduction in serum ammonia levels have been observed in cirrhotic patients with minimal HE without significant side effects.

The therapeutic effect of L-carnitine on HE is achieved by acting at several levels, namely through the activation of metabotropic glutamate receptors (mGluR) at the level of brain ammonia uptake and/or mitochondrial energy metabolism (Jiang et al., 2013).

1.2.9. Pharmacological Modulation of Glutamate (Glu), γ-Aminobutyric Acid (GABA), Benzodiazepine, Dopamine and Endocannabinoid Receptors

The increase of cerebral ammonia levels enhances glutamatergic activity and, consequently, overstimulation of N-methyl-D-aspartate (NMDA) receptors, leading to excitotoxicity and cellular pathways alteration.

Some reports suggest that activation of the Glu – NO – cyclic guanosine monophosphate (cGMP) pathway associated to NMDA receptors plays a role in learning. The impaired cognitive function and learning observed in patients with liver disease and in animal models of CLD or hyperammonemia seems to be related with alterations in the mentioned pathway, which result in the extracellular decrease of cGMP. Sildenafil, a pharmacological inhibitor of the cGMP-degrading phosphodiesterase that crosses BBB, exerts a protective effect on the brain possibly by modulating the extracellular concentration of cGMP and has shown to restore learning ability in rats with CLD or hyperammonemia without liver failure (Rodrigo et al., 2006).

Additionally, memantine, a non-competitive NMDA receptor antagonist improved hyperammonemia-induced encephalopathy in portacaval-shunted rats (Vogels et al., 1997).

Furthermore, ammonia exposure of the brain tissue can result in alterations of other glutamatergic receptors such as mGluR, and other neurotransmission systems like the activation of GABA receptors, and reduction in dopaminergic neurotransmission. In that sense, pharmacological modulators of these receptors have been emerging as potential therapies.

The psychomotor slowing and hypokinesia observed in patients with HE seem to be related with alterations in glutamatergic neurotransmission in the *substantia nigra pars reticulata* and the blockage of mGluR1 at this site by antagonists have normalized the motor activity in portacaval shunt-induced CLD in rats (Cauli et al., 2006).

Through a review on the randomized controlled trials, Als-Nielsen and colleagues evaluated the efficacy and safety of flumazenil, a benzodiazepine antagonist, in cirrhotic patients with HE. In spite of not having effects neither on recovery nor on mortality and to possibly be associated with adverse events, flumazenil had a significant short-term improvement on HE and a highly favorable prognosis in comparison with placebo (Als-Nielsen et al., 2004a).

Patients with HE may present with extrapyramidal symptoms and changes in basal ganglia, symptoms also associated with Parkinson disease. Concerning the improvement of extrapyramidal symptoms, dopamine receptors agonist, such as bromocriptine and levodopa may represent a treatment option. However, a recent review on randomized trials evaluating the beneficial and harmful effects of bromocriptine and levodopa *versus* placebo or no intervention in patients with HE found no arguments to refute or recommend the use of dopamine agents on the treatment of HE, since more randomized placebo-controlled clinical trials without risks of systematic and random errors are needed (Junker et al., 2014).

1.2.10. Molecular Adsorbent Recirculating System (MARS) and Spherical Carbon Adsorbent (AST-120)

The selective removal of toxic substances accumulated in the body as a consequence of liver-dependent processes impairment should prevent their deleterious effects and improve the clinical outcome of patients with HE.

The molecular adsorbent recirculating system (MARS) consists of elements for extracorporeal renal replacement techniques, i.e. hemodialysis and hemofiltration, as well as adsorption using albumin to remove both albumin-bound and water-solved toxins (e.g. ammonia) from plasma. A randomized controlled trial with seventy cirrhotic patients with grade 3 or 4 of HE assessed the efficacy, safety and tolerability of standard medical therapy with or without MARS device additional use and showed a good tolerability, with no unexpected adverse events and an earlier and more frequent improvement of severe HE (Hassanein et al., 2007).

The spherical carbon adsorbent (AST-120) is an oral adsorbent constituted by engineered activated carbon microspheres with high nonspecific adsorptive surface area that pass intact through the gastrointestinal tract, where they adsorb to toxins and mediators of inflammation, including ammonia. A phase 2, multicenter, randomized study with 47 cirrhotic patients with grade 1 or 2 of HE showed that AST-120 is as effective as lactulose for treatment of low-grade HE and better tolerated (Pockros et al., 2009). Furthermore, AST-120 has proved to lower arterial plasma ammonia levels, attenuate brain edema and normalize locomotor activity in adult BDL Sprague-Dawley rats (Bosoi et al., 2011).

1.3. Non-Invasive Techniques to Study HE in Chronic Liver Disease (CLD)

Based on the previous knowledge about the pathogenic events behind HE, assessing the alterations on the concentration of certain brain metabolites represents a task of extreme importance on the diagnosis, study of the disease progression and treatment efficacy evaluation.

Therefore, ^{1}H MRS arises as a powerful technique that allows an *in vivo* and non-invasive study of HE. This technique, in conjugation with a high magnetic field, allows the tracking of approximately twenty metabolites from different brain regions, from which Gln, tCho, Tau, Ins and Cr, involved in osmoregulation; Asp and Glu, involved in neurotransmission; alanine (Ala), lactate (Lac), Cr and PCr, involved in energy metabolism; and glutathione (GSH), an antioxidant, are mandatory for the characterization of brain metabolism in HE.

1.4. Current State of Research on Chronic Hepatic Encephalopathy (CHE)

1.4.1. Importance of *in vivo* Studies

Cudalbu and colleagues assessed recently and for the first time the *in vivo* and longitudinal progression of HE in BDL rats using ^{1}H MRS, Proton Spectroscopic Imaging (^{1}H MRSI) and diffusion tensor imaging (DTI) (Cudalbu et al., 2012). Although few studies using biochemical methods were performed ex-vivo (brain extracts) or on cultured cells (astrocytes or neurons), studies on *in vivo* models of CLD are preferred since they reproduce better the disease-induced effects on the human organism. The primordial

motivation of experimentation in animal models in general has to do with its posterior application for the benefit of human beings.

At the present time, an optimal model of CHE does not exist. However, the surgically obstruction of the common bile duct induces a reproducible model of biliary cirrhosis in rats, which was approved as an animal model of type C HE by members of the ISHEN (Butterworth et al., 2009). The bile duct ligation induces liver failure and BDL rats develop jaundice, portal hypertension, portal-systemic-shunting, bacterial translocation and immune system dysfunction, and show decreased locomotor activities.

1.4.2. Previous Results on Bile Duct-Ligated (BDL) Rats

1.4.2.1. Brain Edema and Osmolytes

There is only one recent *in vivo* study in BDL Sprague-Dawley rats using ^{1}H MRS and performed on a 7T magnetic resonance system, at 4, 5 and 6 weeks after the surgery. Changes in very few metabolites (i.e. Gln, Ins, tCho, Glu and N-acetylaspartate (NAA) were shown at late time points (Chavarria et al., 2013).

Another study in BDL Sprague-Dawley rats has shown a significant increase of brain water content, an indicator of brain edema, at six weeks after the bile duct obstruction. The brain edema appearance was correlated to a prominent increase of blood ammonia and systemic oxidative stress levels but not with any BBB extravasion (Bosoi et al., 2012).

As it was already mentioned, HE-related learning and memory abnormalities have been associated with disturbances in different neurotransmitter pathways. Behavioral studies have been undertaken to explore the spatial and temporal structure of behavior, as well as to investigate the cognitive function in BDL rats. The open-field task in adult

female Wistar rats showed altered spatio-temporal locomotor and exploratory activities, characterized by a decrease in the total distance traveled, increased immobility time and smaller total number of rearings (Leke et al., 2012). In addition, an object recognition task conducted in adult male Wistar rats demonstrated an impairment of short-term memory for recognition and unaffected long-term memory (Leke et al., 2013).

1.4.2.2. Preliminary Studies: Research done in CIBM/LIFMET

Several *in vivo* and longitudinal studies have taken place in Centre d'Imagerie Biomédicale (CIBM) and Laboratory of Metabolic Imaging (LIFMET) (Cudalbu et al., 2012; Braissant et al., 2013; Cudalbu, 2013), allowing the chronological assessment of metabolic concentrations in some brain regions known to be linked to cognitive impairments in patients and animals with CHE. For that, ^{1}H MRS at a 9.4T main magnetic field have been performed in adult BDL rats during eight weeks after biliary cirrhosis-induced operation.

On hippocampus, a gradual increase of Gln has been observed, reaching more than two-fold increase at eight weeks. On the other hand, other metabolites were found to be decreased: firstly, Ins (~30-35%), followed, respectively, by Tau (~10-20%) and tCho (~30-40%). However, the sum of the osmolytes remained roughly constant over time. Furthermore, Cr decreased gradually, reaching ~13-20% at 8 weeks, as well as the brain neurotransmitters Glu, Asp and GABA (~10-30%) and the brain antioxidants ascorbate (Asc) and GSH (~9-15%). Brain histology by immunofluorescence assessed the morphology of the astrocytes and the water channels expression at the eighth week post bile-duct ligation and showed swollen astrocytes and a slight increase of the water channels expression. Furthermore, plasma ammonia levels were measured and found increased.

Based on these results, the authors were able to conclude that an osmotic regulation is triggered by the Gln increase, resulting in a reduction of other osmolytes. However, this balance attempting seems to be not completely satisfactory, since a low-grade edema is still formed, with evidence based on astrocyte swelling. The increased expression of water channels contributes to an increased BBB permeability, which can be also related to cerebral edema.

CHAPTER 2

Introduction to Proton Magnetic Resonance Spectroscopy (^{1}H MRS)

This chapter was generally based on information taken from de Graaf (2008), Kunz (2010) *and* Lanz (2012).

2.1. Nuclear Magnetic Resonance (NMR)

Nuclear magnetic resonance (NMR) is the study of magnetic properties and energies of nuclei.

2.1.1. Nuclear Spin and Magnetic Moment

The nucleus is a dense region composed of protons and neutrons, which have a half-integer spin equal to ½. The number of protons and neutrons, as well as the nuclear spin quantum number, I, which represents the vectorial combination of the spins of protons and neutrons characterize the nucleus.

Although classical physics is incapable of describing the quantum mechanical spin, it can be used to create a familiar frame of reference in which the existence of a spin angular momentum can be visualized. The nuclear spin, I, represents the rotation of the nucleus around its own axis at a constant velocity. This motion is described by an angular momentum vector $\vec{L}$. Since the rotating nucleus carries an electrical charge, conferred by protons, a current loop is created that, consequently, generates a magnetic field characterized by the nuclear magnetic moment or magnetic dipole moment, $\vec{\mu}$. As a result, the nucleus can be thought of as a minute bar

magnet. The angular momentum is directly proportional to the magnetic moment through the expression:

$$\vec{\mu} = \gamma \vec{L} \tag{2.1}$$

where γ is the gyromagnetic ratio of the nucleus.

In quantum mechanics, the intrinsic angular momentum of elementary particles and nuclei is quantized and its projection in the z direction, L_z, and amplitude, $|\vec{L}|$, are given, respectively, by:

$$L_z = \left(\frac{h}{2\pi}\right) m \tag{2.2}$$

$$|\vec{L}| = \frac{h}{2\pi} \cdot \sqrt{I \cdot (I+1)} \tag{2.3}$$

where h is Planck's constant and m is the magnetic quantum number that specifies the direction of angular momentum and can have $2I + 1$ values, given by:

$$m = I, I-1, I-2, \dots, -I \tag{2.4}$$

Due to the intricate interactions between nucleons, i.e. the components of the nucleus, the nuclear spin quantum number I cannot simply be calculated by summation of the nuclear individual components. However, by using the mass number A, which represents the total number of nucleons, and the atomic number or protons number Z of a given atom, I can be deduced from the following rules:

1. For nuclei with an odd mass number, I is half-integral ($^1/_2$, $^3/_2$, $^5/_2$, ..., e.g. ^{1}H, ^{13}C, ^{15}N, ^{23}Na and ^{31}P).

2. For nuclei with even mass and atomic numbers, I is zero (e.g. ^{12}C, ^{16}O and ^{32}S).
3. For nuclei with an even mass and an odd atomic numbers, I is an integral number (1, 2, 3, ... e.g. ^{2}H and ^{14}N).

In order to be NMR active, a nucleus must have $I > 0$, since nuclei with zero nuclear spin do not interact with magnetic fields. However, many other factors, which will be further discussed bellow, influence the NMR signal.

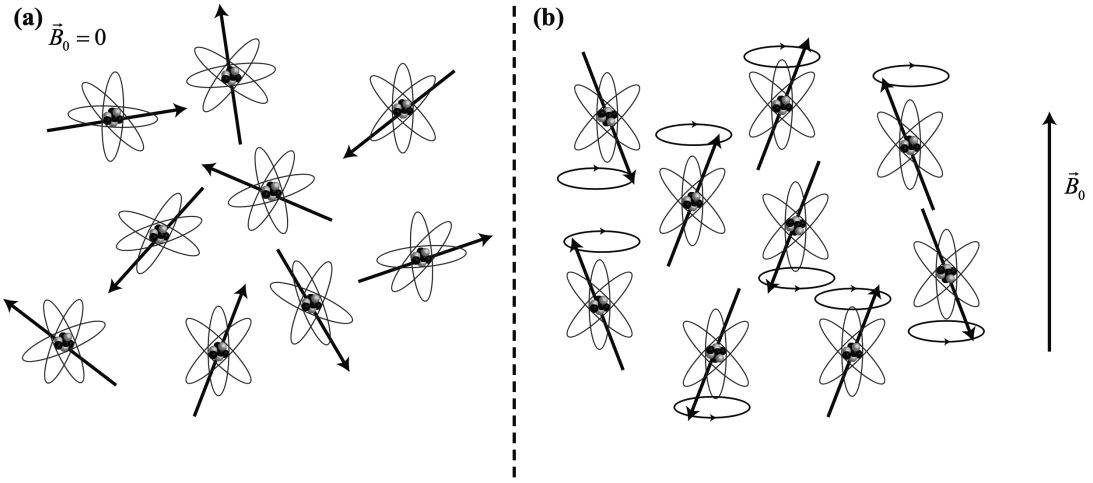

Figure 3 - Bulk magnetization **(a)** in the absence and **(b)** in the presence of an external magnetic field. In the absence of an external magnetic field ($\overrightarrow{\mathbf{B_0}}$), the nuclear magnetic moments are oriented randomly, while in the presence of $\overrightarrow{\mathbf{B_0}}$ the nuclear magnetic moments get aligned to it, in respect to their discrete energetic sublevels. Figure taken from Kunz (2010).

2.1.2. Magnetization

In the absence of an external magnetic field, the magnetic moment of a NMR active nucleus is oriented randomly (Figure 3.(a)). When a static magnetic field $\overrightarrow{B_0}$ oriented along z, by convention, is applied, its interaction with the nuclear magnetic moment will create a magnetic energy, E, given by:

$$E = -\vec{\mu} \cdot \overrightarrow{B_0} = -\mu \cdot \cos\theta \cdot B_0 = -\mu_z \cdot B_0 \qquad (2.5)$$

The projection of the nuclear magnetic moment in the z direction, μ_z, is given by the association of Equations (2.1) and (2.2). The combination of the classical description of the magnetic energy [Equation (2.5)] with the quantum mechanical formulation of the nuclear magnetic moment [Equations (2.1) and (2.2)] gives:

$$E = -\gamma \cdot \left(\frac{h}{2\pi}\right) \cdot m \cdot B_0 \tag{2.6}$$

Since m is a discrete quantum number, the energy levels are also quantized. For a particle of spin $I = {}^1/_2$, two distinct energy levels associated with different electronic states are possible: $m = {}^1/_2$ and $m = -{}^1/_2$. While the former corresponds to a lower energy level (α spin state) where the nuclear magnetic moments are parallel with $\overrightarrow{B_0}$, the latter is associated with a higher energy level (β spin state) and the spins have an antiparallel alignment with $\overrightarrow{B_0}$ (Figure 3.(b)). The energy difference between the two states is given by:

$$\Delta E = \gamma \left(\frac{h}{2\pi}\right) B_0 \tag{2.7}$$

and corresponds to electromagnetic radiation in the radio frequency (RF) range. The interaction between atoms and electromagnetic radiation is characterized by the absorption and emission of photons, such that the energy of the photons exactly matches an energy level difference in the atom. Therefore, the transition between two spin states can be achieved by applying an external oscillating magnetic field perpendicular to μ_z with a frequency ν, such that the energy carried by the photon of this magnetic field corresponds to the energy splitting between the two spin states:

$$\Delta E = h\nu \Leftrightarrow \nu = \frac{\gamma}{2\pi} B_0 \tag{2.8}$$

The induced energy level difference of nuclei in an external magnetic field is very small when compared with the thermal energy, making it that the levels are almost equally populated at room or body temperature. The ratio of the α and β spin states at any specific temperature T in kelvin and in the presence of a static magnetic field due to their difference in energy levels ΔE is given by:

$$\left(\frac{n_\beta}{n_\alpha}\right) = e^{-\frac{\Delta E}{\kappa_B T}} = e^{-\frac{\gamma B_0}{2\pi\kappa_B T}} \tag{2.9}$$

where κ_B is the Boltzmann constant.

As mentioned before, each nucleus can be seen as a minute bar magnet and, therefore, is associated with a magnetic dipole moment $\vec{\mu}$. When placed in an external magnetic field $\overrightarrow{B_0}$, the nuclear magnetic moment will feel a torque given by:

$$\vec{\tau} = \vec{\mu} \times \overrightarrow{B_0} \tag{2.10}$$

According to Newton's second law for rotations:

$$\vec{\tau} = \frac{d\vec{L}}{dt} \tag{2.11}$$

The combination of the Equations (2.1), (2.10) and (2.11) originates:

$$\frac{d\vec{\mu}}{dt} = \vec{\mu} \times \gamma\overrightarrow{B_0} \tag{2.12}$$

Since the amplitude of $\vec{\mu}$ is constant, the differential equation in Equation (2.12) expresses the fact that $\vec{\mu}$ changes its orientation relative to $\overrightarrow{B_0}$, i.e. $\vec{\mu}$

precesses about $\overrightarrow{B_0}$ at a frequency ω_0, named Larmor frequency and defined as:

$$\omega_0 = \gamma B_0 \tag{2.13}$$

The total net magnetic moment, i.e. the magnetization $\vec{M}$, of a macroscopic sample is the resultant of the sum over all individual nuclear magnetic moments $\vec{\mu_i}$:

$$\vec{M} = \sum_{i=1}^{n} \vec{\mu_i} \tag{2.14}$$

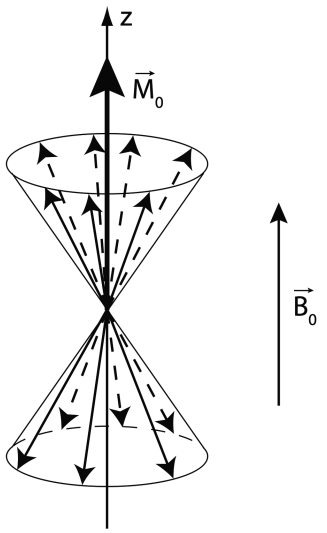

Figure 4 - Distribution of the individual magnetic dipole moments of a population of identical nuclei with spin ½ in an external magnetic field ($\overrightarrow{\mathbf{B_0}}$). The nuclear magnetic moments are divided in two populations that precess on a cone around $\overrightarrow{\mathbf{B_0}}$. Their vector sum results in a net macroscopic magnetization ($\overrightarrow{\mathbf{M_0}}$) aligned along $\overrightarrow{\mathbf{B_0}}$. Figure taken from Lanz (2012).

Due to quantization of the nuclear magnetic moment [see Equations (2.2) and (2.3)], each individual spin is oriented according to θ, the angle between $\vec{\mu}$ and $\overrightarrow{B_0}$. In the general case of a spin I nucleus, the magnetic moments will be randomly distributed on $2I + I$ cones at discrete angles θ. In

that sense, there will be no net component of $\overrightarrow{M_0}$ in the transverse xy plane, given that $\overrightarrow{M_0}$ is the macroscopic magnetization vector at thermal equilibrium. However, due to the spin state population difference, there will be a net component of $\overrightarrow{M_0}$ parallel with $\overrightarrow{B_0}$ (Figure 4) with magnitude:

$$\left|\overrightarrow{M_0}\right| = \left(n_\alpha - n_\beta\right) \cdot \mu_z \tag{2.15}$$

Since at normal temperature $\Delta E \ll \kappa_B T$, the exponent in Equation (2.9) can be simplified through an expansion and truncation of a Taylor series to give:

$$\left(\frac{n_\beta}{n_\alpha}\right) = 1 - \left(\frac{\Delta E}{\kappa_B T}\right) \tag{2.16}$$

Assuming $n = n_\alpha + n_\beta$ and $n_\alpha \approx n_\beta \approx \frac{n}{2}$ where n is the total number of nuclear spins in the macroscopic sample, the population difference $\left(n_\alpha - n_\beta\right)$ is approximately given by:

$$\left(n_\alpha - n_\beta\right) \approx \left(\frac{n\Delta E}{2\kappa_B T}\right) \tag{2.17}$$

The association of Equations (2.7), (2.15) and (2.17) gives, at thermal equilibrium, the amplitude of the macroscopic magnetization vector $\overrightarrow{M_0}$:

$$\left|\overrightarrow{M_0}\right| = \frac{h\mu_z}{4\pi\kappa_B T}\gamma B_0 n \tag{2.18}$$

The intensity of the final received signal is proportional to the spin state population difference and, thus, to the amplitude of the macroscopic magnetization vector. The small energy level difference between the two spin states makes NMR, on the one hand, an insensitive technique and, on the other, a noninvasive and nondestructive technique, ideally suited for *in vivo*

measurements, since only non-ionizing electromagnetic fields are involved. However, the experiment sensitivity is determined by other factors, some of which can be deduced from Equation (2.18). Firstly, one can mention the intrinsic properties of the chosen nuclei, essentially the natural abundance and gyromagnetic ratio γ. In that sense, the proton nucleus (^{1}H) is the most commonly used nuclei as it yields the strongest NMR signal due to a combination of its high natural abundance (99.98%) and high intrinsic NMR sensitivity (high gyromagnetic ratio γ: $42.58\,\mathrm{MHz}\cdot\mathrm{T}^{-1}$). Additionally, the linear dependence of M_0 on the magnetic field strength B_0 implies that higher magnetic fields improve the sensitivity, and the inverse proportionality of M_0 to the temperature T indicates that sensitivity can be enhanced at lower sample temperatures. Obviously, the latter option is unrealistic for *in vivo* applications, which results in a constant interest in building higher magnetic field systems.

2.1.3. Excitation

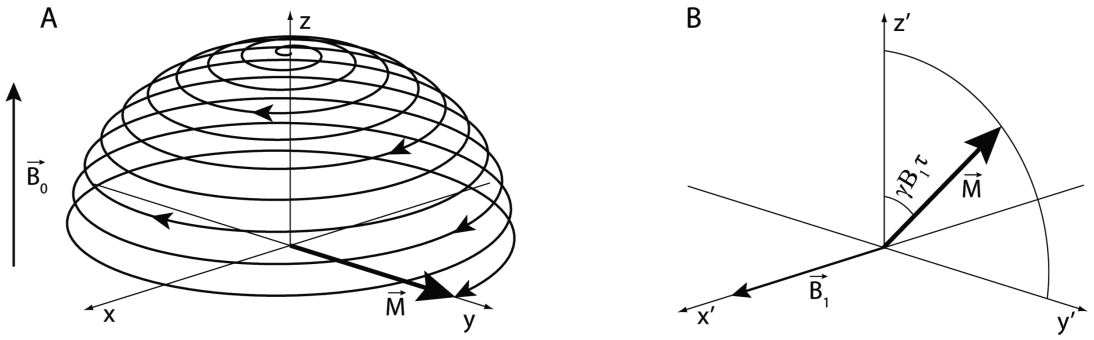

Figure 5 - Excitation of the magnetization **(A)** in the laboratory frame and **(B)** in the rotating frame of reference. Using an additional oscillating magnetic field ($\overrightarrow{\mathbf{B_1}}(\mathbf{t})$), the macroscopic magnetization can be tilted towards the transverse plane while it simultaneously precesses around the static magnetic field ($\overrightarrow{\mathbf{B_0}}$) and $\overrightarrow{\mathbf{B_1}}(\mathbf{t})$. The problem can be analyzed in a simpler way in the rotating frame, which spins about z at the Larmor frequency and where the macroscopic magnetization simply rotates about $\overrightarrow{\mathbf{B_1}}$. In the rotating frame, $\overrightarrow{\mathbf{B_1}}(\mathbf{t})$ appears static since it oscillates at the same frequency as the frame rotates. Figure taken from Lanz (2012).

The quantum mechanical representation is convenient to illustrate the spin distribution, but it is not very suitable to illustrate the interaction of the spins with external magnetic fields. Therefore, the classical picture of the net macroscopic magnetization $\vec{M}$ will be used in further discussions.

The signal detection in NMR is based in the Faraday's law of electromagnetic induction stipulating that a time-varying magnetic field can induce and electromotive force (emf) in a receiver coil surrounding the sample. Therefore, in order to obtain a signal, a precessional motion of the macroscopic magnetization needs to be detected. However, at thermal equilibrium, the spins have no phase coherence in the transverse plane and the net longitudinal magnetization is a static vector. Nuclear magnetization can only be observed by rotating the net longitudinal magnetization towards or onto the transverse plane. As mentioned before, the resonance phenomenon in NMR is achieved by applying an oscillating magnetic field, $\overrightarrow{B_1}(t)$, in the transverse plane with a frequency ν, such that the energy equals the energy splitting between the two spin states. From Equations (2.8) and (2.13) one can deduce that ν corresponds to the Larmor frequency ($\nu = \nu_0$), which is the one required to excite spins from the α state to the β one. $\overrightarrow{B_1}(t)$ is applied as a RF pulse, i.e. turned on for a finite time and turned off again and, with a sinc shape, since it has the interesting property of presenting an excitation profile close to an ideal square function. The receiver coil, also called RF coil, can also be used as transmitter during the excitation process to generate the $\overrightarrow{B_1}(t)$ magnetic field. It has two effects on the spins: firstly, the two spin states become more equally populated as a 90° nutation (rotation) is approached; and secondly the spins come into a state of phase coherence, i.e. the $\overrightarrow{B_1}(t)$ magnetic field forces the phases of the spins to attain coherence thereby generating transverse magnetization.

The expression of motion for a single nuclear magnetic moment [Equation (2.12)] can be generalized for the total magnetization, originating:

$$\frac{d\vec{M}(t)}{dt} = \vec{M}(t) \times \gamma \vec{B}(t) \tag{2.19}$$

the so-called Larmor equation, where $\vec{B}(t)$ may include time-varying components in addition to the static magnetic field $\overrightarrow{B_0}$. At thermodynamic equilibrium, $\vec{B}(t) = \overrightarrow{B_0}$ and, therefore, $\frac{d\overrightarrow{M_0}}{dt} = 0$ since $\overrightarrow{M_0}$ is parallel to $\overrightarrow{B_0}$. However, during the RF pulse, $\vec{B}(t) = \overrightarrow{B_0} + \overrightarrow{B_1}(t)$, thus giving:

$$\frac{d\vec{M}(t)}{dt} = \vec{M}(t) \times \gamma \left(\overrightarrow{B_0} + \overrightarrow{B_1}(t) \right) \tag{2.20}$$

As a result, the initially longitudinal magnetization experiences a torque from the applied perpendicular $\overrightarrow{B_1}(t)$ field, which results in the precession of $\vec{M}(t)$ around both $\overrightarrow{B_0}$ and $\overrightarrow{B_1}(t)$ progressively tilting towards the transverse plane (Figure 5.A).

Until this point, the NMR experiment has been described in a Cartesian frame fixed with respect to the laboratory, i.e. the “laboratory” frame. However, in order to simplify the description of motion of the magnetization vector, one must introduce the rotating frame. The rotating frame consists in a new set of Cartesian axes that rotates about the static magnetic field $\overrightarrow{B_0}$ with frequency ω. The z and z’ axes of the laboratory and rotating frames, respectively, are collinear with the external magnetic field $\overrightarrow{B_0}$. The conversion to a rotating frame of reference has consequences for the magnetic field vectors encountered in that frame. Firstly, the precessional motion of the magnetization ω_0 appears to be reduced to a value $(\omega_0 - \omega)$. It is convenient to define an effective magnetic field, $\overrightarrow{B_{eff}}$, since the magnetization precesses about the effective field:

$$\overrightarrow{B_{eff}}(t) = \overrightarrow{B_1}(t) + \frac{(\omega_0 - \omega)}{\gamma} \hat{e}_z \tag{2.21}$$

On-resonance, i.e. when the frequency of the applied RF pulse, ω_{RF}, equals the Larmor frequency ω_0, Equation (2.21) reduces to $\overrightarrow{B_{eff}}(t) = \overrightarrow{B_1}(t)$ and the magnetization simply rotates about $\overrightarrow{B_1}(t)$. In a frame that rotates with a frequency equal to the frequency of $\overrightarrow{B_1}(t)$, $\overrightarrow{B_1}(t)$ appears static ($\overrightarrow{B_1}$) (Figure 5.B). The extent to which $\vec{M}$ is rotated, which can be described by the nutation angle, θ, depends directly on the duration, τ, and amplitude of $\overrightarrow{B_1}$:

$$\theta(\tau) = \gamma B_1 \tau \tag{2.22}$$

When $\overrightarrow{B_1}$ is applied long enough, $\vec{M}$ can be completely excited onto the transverse plane or even inverted to the –z'-axis, giving rise to so-called 90° excitation and 180° inversion RF pulses, respectively. The longitudinal and transverse magnetizations in the rotating frame can be respectively written regarding θ as such:

$$M_z = M_0 \cos\theta \tag{2.23}$$

$$M_{xy} = M_0 \sin\theta \tag{2.24}$$

2.1.4. Relaxation

Relaxation is the process of return to thermal equilibrium after a perturbation. Components of the magnetization (M_x, M_y and M_z) return to the equilibrium, a process described by:

$$\frac{dM_x(t)}{dt} = -\frac{M_x(t)}{T_2} \tag{2.25}$$

$$\frac{dM_y(t)}{dt} = -\frac{M_y(t)}{T_2} \tag{2.26}$$

$$\frac{dM_z(t)}{dt} = -\frac{M_z(t) - M_0}{T_1} \tag{2.27}$$

where T_1 and T_2 are relaxation time constants; after a 90° excitation pulse, T_1 corresponds to the time at which 63% of M_z relaxed back and T_2 to the time at which 37% of M_{xy} decayed. As mentioned before, the equilibrium state is defined by two conditions: the population ratio should satisfy the Boltzmann distribution [Equation (2.9)] and the entropy should be on its maximum, which corresponds to a system with no phase coherence. Therefore, two spontaneous processes are involved in the exponential return to equilibrium: the longitudinal or spin-lattice relaxation, characterized by the time constant T_1; and the transverse or spin-spin relaxation, characterized by the time constant T_2. These relaxation processes are, respectively, described by:

$$M_z(t) = M_0 \cdot \left(1 - e^{-\frac{t}{T_1}}\right) + M_z(0)e^{-\frac{t}{T_1}} \tag{2.28}$$

$$M_{xy}(t) = M_{xy}(0)e^{-\frac{t}{T_2}} \tag{2.29}$$

While the former describes the return of longitudinal magnetization after a perturbation, the latter describes the disappearance of transverse magnetization. Longitudinal relaxation is in principle a process in which energy from the spins is transferred to the surrounding molecular environment, called the “lattice”, and during T_2 relaxation spins exchange energy between themselves. NMR relaxation mechanisms differ from interactions between other electromagnetic fields and matter, as there is no spontaneous emission of energy to the environment. The spin relaxation processes can only occur through a stimulated transition by a magnetic field that fluctuates in a broad range of frequencies that contains the Larmor frequency, which is the driving frequency for stimulating an energy state transition. The longitudinal relaxation is induced by random fluctuating

fields due to thermal energy-induced motion of the molecules in the environment of the nuclear spin. The sources of this fluctuating magnetic field are dipolar coupling between nuclei and interaction between nuclear magnetic dipoles. Besides being also influenced by fluctuating magnetic fields, the transverse relaxation is affected by a static magnetic contribution, which is caused by the imperfect homogeneity of the applied magnetic field $\overrightarrow{B_0}$ on a molecular level. Therefore, these T_2 relaxation mechanisms are combined with the effect of macroscopic $\overrightarrow{B_0}$ inhomogeneity, resulting in a total decay of transverse magnetization with a time constant T_2^*, which is always shorter than T_2 . Consequently, the individual nuclear spins accumulate progressively different phases and the coherence of the detectable transverse magnetization is lost.

2.1.5. Bloch Equations

Bloch equations provide a classical approach to describe the evolution of the macroscopic magnetization in the presence of an external magnetic field, i.e. under precession, excitation and relaxation.

The expansion of Equation (2.20) gives:

$$\frac{dM_x(t)}{dt} = \gamma\left[M_y(t)B_0 - M_z(t)B_{1y}\right] \tag{2.30}$$

$$\frac{dM_y(t)}{dt} = \gamma\left[M_z(t)B_{1x} - M_x(t)B_0\right] \tag{2.31}$$

$$\frac{dM_z(t)}{dt} = \gamma\left[M_x(t)B_{1y} - M_y(t)B_{1x}\right] \tag{2.32}$$

that in combination with Equations (2.25)-(2.27) yields Bloch equations in the laboratory frame of reference:

$$\frac{dM_x(t)}{dt} = \gamma\left[M_y(t)B_0 - M_z(t)B_{1y}\right] - \frac{M_x(t)}{T_2} \tag{2.33}$$

$$\frac{dM_y(t)}{dt} = \gamma[M_z(t)B_{1x} - M_x(t)B_0] - \frac{M_y(t)}{T_2} \tag{2.34}$$

$$\frac{dM_z(t)}{dt} = \gamma\left[M_x(t)B_{1y} - M_y(t)B_{1x}\right] - \frac{M_z(t) - M_0}{T_1} \tag{2.35}$$

In a rotating reference frame, Bloch equations can be written as:

$$\frac{dM'_x}{dt} = (\omega_0 - \omega) \cdot M'_y(t) - \gamma M'_z(t)B'_{1y} - \frac{M'_x(t)}{T_2^*} \tag{2.36}$$

$$\frac{dM'_y}{dt} = -(\omega_0 - \omega) \cdot M'_x(t) + \gamma M'_z(t)B'_{1x} - \frac{M'_y(t)}{T_2^*} \tag{2.37}$$

$$\frac{dM'_z}{dt} = \gamma\left(M'_x(t)B'_{1y} - M'_y(t)B'_{1x}\right) - \frac{(M'_z(t) - M_0)}{T_1} \tag{2.38}$$

where B'_{1x} and B'_{1y} correspond to the fixed coordinates of the $\overrightarrow{B_1}$ field in the rotating frame of reference.

2.2. Magnetic Resonance Imaging (MRI)

Magnetic resonance imaging (MRI) is, nowadays, an important imaging modality, since it allows the noninvasive and nondestructive generation of images in intact living objects. By taking advantage of the dissimilar NMR relaxation properties between different tissues and, thereby, choosing proper experimental parameters, excellent soft tissue contrast can be achieved. This allows the identification of spatial boundaries and

distribution of different tissues within the object under investigation. Besides the contrast between tissues, two other factors determine the quality and clarity of images: the signal-to-noise ratio (SNR), i.e. the signal intensity divided by the background noise, and the spatial resolution. In the setting of MRS, MRI is particularly useful for the accurate determination of the origin of the MRS signals taking into account that, for *in vivo* MRS studies, it is often of interest to obtain information on a specific region of the tissue, known as volume of interest (VOI). The principles underlying MRI also apply for many *in vivo* MRS techniques.

2.2.1. Magnetic Field Gradients

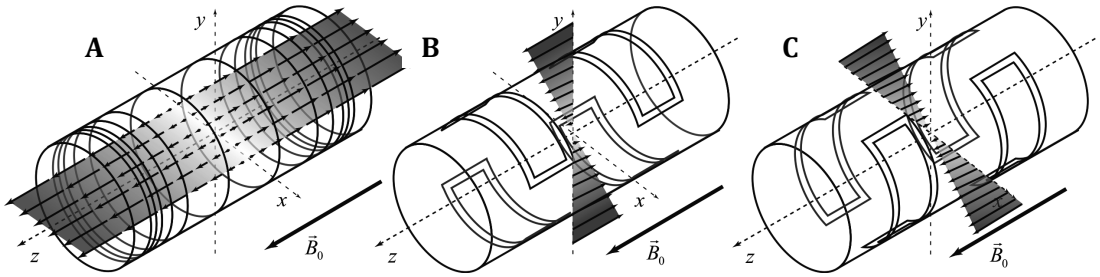

Figure 6 – Gradients' system. The three set of coils generate orthogonal linear gradients linearly varying with the position according to **(A)** z, **(B)** y and **(C)** x axes. The magnetic field strength of all gradients is zero in the magnet's isocenter. According to each direction, a gradient is progressively added or subtracted from the main magnetic field on each side of the middle. Figure taken from Kunz (2010).

The essential concept of MRI is that the resonant frequency ω_0 is made position-dependent, such that after Fourier transformation the different frequencies correspond to different spatial positions. This can be achieved by using a third static but spatially varying magnetic field, known as gradient, in addition to the main field $\overrightarrow{B_0}$, thus generating a total magnetic field at position r given by:

$$B(r) = B_0 + G_r \cdot r \tag{2.39}$$

where G_r is the gradient strength. The magnetic field gradient system is made up of three resistive coils that generate orthogonal magnetic fields, G_x, G_y and G_z, with intensity linearly varying according to x, y and z directions, respectively. As a consequence, if a linear term $G_r \cdot r$ is added to B_0, which always remains in the z direction, the resonant frequency will be linearly proportional to the position along r and is given by:

$$\omega(r) = \gamma(B_0 + G_r \cdot r) \tag{2.40}$$

The magnetic field gradient is positioned around the center of the magnet, i.e. a gradient adds to the main magnetic field on one side of the middle and subtracts from the static field in the other side. Therefore, the magnetic field strength of all gradients is zero in the magnet's isocenter (Figure 6).

Besides its linearity in space, important characteristics of a gradient system are its maximal strength and the minimum time needed to reach the maximum amplitude (i.e. rise time). The gradients strength is the main constraint for the spatial maximal resolution, while the rise time constrains the acquisition speed.

2.2.2. Slice Selection

To obtain an image of a 3D object, all three dimensions need to be encoded independently, which could be a time-consuming procedure. Therefore, one often reduces the problem to two dimensions by selecting a spatial slice out of a 3D object.

If a magnetic field gradient is applied during the RF pulse, the frequency of the RF pulse can be chosen in order to be in resonance

conditions only for the magnetization located at a chosen position r. Thereby, a slice perpendicular to the gradient direction will be selected, with its position given by the center frequency of the RF pulse, ω_{RF}, and with a thickness dependent on both bandwidth of the pulse and gradient strength (Figure 7), according to the following relationship:

$$\Delta r = \frac{\Delta\omega}{\gamma \cdot G_r} \tag{2.41}$$

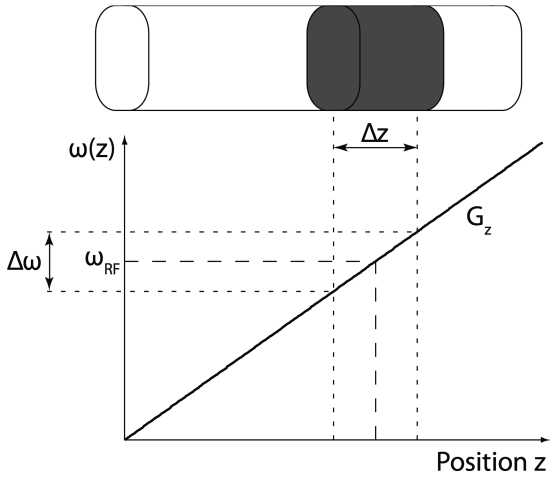

Figure 7 - Principle of NMR localization by slice selection. Using an additional gradient magnetic field, the Larmor frequency of a given nucleus becomes space-dependent along the direction of the gradient (z in the example). A radio frequency (RF) pulse with a carrier frequency $\boldsymbol{\omega_{RF}}$ and a bandwidth $\Delta\omega$ enables the selective excitation of the magnetization in a slice located at a desired position and with a specific thickness. Figure taken from Lanz (2012).

After selecting one or more spatial slices, the origin of the MR signal needs to be encoded in two dimensions, i.e. individualized into pixels. Therefore, two more gradients must be applied to encode frequency and phase. In a transverse slice, the horizontal axis is usually set as the frequency encoding direction, while the vertical axis is the phase encoding direction of excited protons. These gradients (G_x and G_y, respectively) are required to be

applied at different times, since they cannot be differentiated from one another if they overlap.

2.2.3. Frequency Encoding

The frequency encoding gradient, or readout gradient, is composed of two constant amplitude gradient pulses. One is applied prior to signal acquisition (prephasing gradient) while the other, being of opposite sign and typically having twice the area, is applied during the signal acquisition. The function of the prephasing gradient is to prepare the transverse magnetization for encoding spatial information during signal acquisition. At the end of it, the transverse magnetization at each position x is prepared with a specific phase shift given by:

$$\phi(x,t) = \gamma x G_x t \tag{2.42}$$

The second gradient pulse is of opposite sign and the total area is twice that of the first gradient. Therefore, the total applied gradient in the middle of the second gradient is zero and the dephasing caused by the initial gradient is completely undone. Since the transverse magnetization prior to signal acquisition had acquired a linear position-dependent phase shift during the first gradient, spins at different spatial positions have to rotate at different frequencies to fulfill the condition $\phi(x) = 0$ in the middle of the second gradient.

2.2.4. Phase Encoding

The principle of phase encoding is not much different from frequency encoding, i.e. the magnetic field gradient G_y encodes the phase of the

transverse magnetization as a function of position, and indirectly the frequency, since:

$$\omega(y) = \frac{d\phi(y,t)}{dt} \tag{2.43}$$

To obtain spatial information along the phase encoding dimension, a number of experiments need to be performed in which the amplitude of the gradient G_y, usually applied before G_x, is changed between $+G_{y,max}$ and $-G_{y,max}$ in fixed steps.

2.2.5. Spatial Frequency Space (*k*-space)

During the data acquisition of an MRI sequence, the transversal components of the magnetization in the imaging object after excitation are sampled from the receiver coil signal, i.e. are acquired analog and converted to a digital value. So far, the NMR signal has been described as a continuous, analog signal. Since many mathematical operations are most conveniently performed by digital computer algorithms, the digital signal is obtained by measuring the instantaneous value of the analog signal at equal time intervals. The raw data is then stored in a matrix, the *k*-space, as a function of time. Each of the data points is characterized by a k_f and k_p value, the k-parameters of frequency and phase-encoding directions, respectively, which are defined as following:

$$k_f = \gamma G_x \Delta t \tag{2.44}$$

$$k_p = \gamma G_y \tau \tag{2.45}$$

where Δt is the sampling time and τ is the duration of G_y. Therefore, the position in *k*-space is directly related to the gradient across the object being imaged. By using G_y and G_x sequentially, keeping the magnitude G_x the same but changing G_y's magnitude repeatedly at each repetition time (TR) interval, every line of the *k*-space must be filled in order to generate an optimum image. When the phase-encoding gradient is zero, the signal gives the spatial distribution of the object in the x direction.

The relationship between *k*-space data and image data is the Fourier transformation. Every point in the *k*-space contains part of the information for the complete image. However, a point in the *k*-space does not correspond to a point in the image matrix. While coordinates at the edges of the *k*-space - high spatial frequencies - provide information regarding the borders and contours of the image, i.e. the detail of the structures, coordinates near the middle of the matrix - low spatial frequencies - provide information on the general contrast of the image. The raw data from the MRI acquisition undergoes a 2D Fourier transformation, resulting in a representation of the magnetization amplitude distribution. Knowledge of the gradient strengths allows, in conjunction with Equation (2.40), the conversion of the frequency axes into spatial axes.

As mentioned before, the spatial information is primarily acquired as an analog time-dependent signal. This signal is termed echo; gradient-echo and spin-echo form the basis for the majority of MRI methods. The time between the slice selective RF pulse and the top of the echo, where optimum refocusing occurs, is referred to as echo time (TE).

2.2.6. Gradient Echo

An excitation pulse, i.e. a 90° RF pulse, followed by phase and frequency encoding, creates a gradient echo, which contributes to a line of *k*-space data. The gradient echo is formed when the transverse magnetization

signal is at a maximum, i.e. when the area under the second frequency encoding gradient pulse equals the one under the prephasing gradient. Due to the RF pulse between 0 and 90°, part or all the magnetization is in the transverse plane. The frequency encoding gradient causes, in a first stage, different sets of spins to acquire different phases; this dephasing is, however, reversed at a second stage, where spins return to their original phase-coherent state, thus forming the gradient echo (Figure 8).

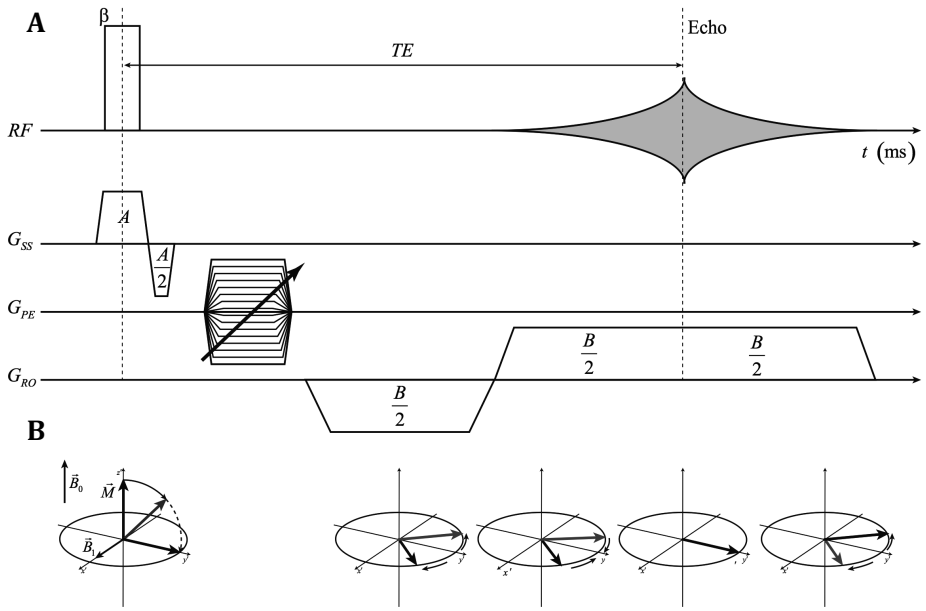

Figure 8 - (A) Gradient echo pulse sequence and **(B)** representation of its effect on macroscopic magnetization. A small flip angle β radio frequency (RF)-pulse is applied and, at the same time, a slice selection gradient (G_{SS}) is used to excite only a slice of the sample. At the end of the slice selective gradient, the signal through the slice thickness is slightly dephased. To compensate for this effect, a second gradient is applied along the same axis, with opposite polarity and half of the area, which result in complete rephasing of the signal. This is followed by the application of phase encoding gradients (G_{PE}). Finally the echo is generated by a fast dephasing and rephasing of the signal by the application of two gradients with opposite polarity (G_{RO}). At the time that the second gradient has completely compensated the first dephasing gradient, the echo is at its maximum amplitude, decaying exponentially afterwards with a time constant $\mathbf{T_2^*}$. Figure taken from Kunz (2010).

It is always possible to recover a dephased signal by applying a magnetic field gradient of opposite sign, provided that the signal has not

been irreversibly lost by T_2 relaxation. The gradient reversal in gradient-echo techniques refocuses only those spins that have been dephased by the action of the gradient itself; therefore, the relaxation due to T_2 relaxation and static field inhomogeneities is not reversed and the loss of signal results from T_2^* effects. These sequences are, thus, more sensitive to magnetic field inhomogeneities, leading to an additional phase evolution that is independent of the applied magnetic field gradients. On the other hand, gradient echo techniques offer the advantage of low-flip angle excitations, contributing to a faster acquisition and, therefore, decreased duration of scan. A flip angle lower that 90° decreases the amount of magnetization tipped into the transverse plane, thus inducing a faster recovery of longitudinal magnetization.

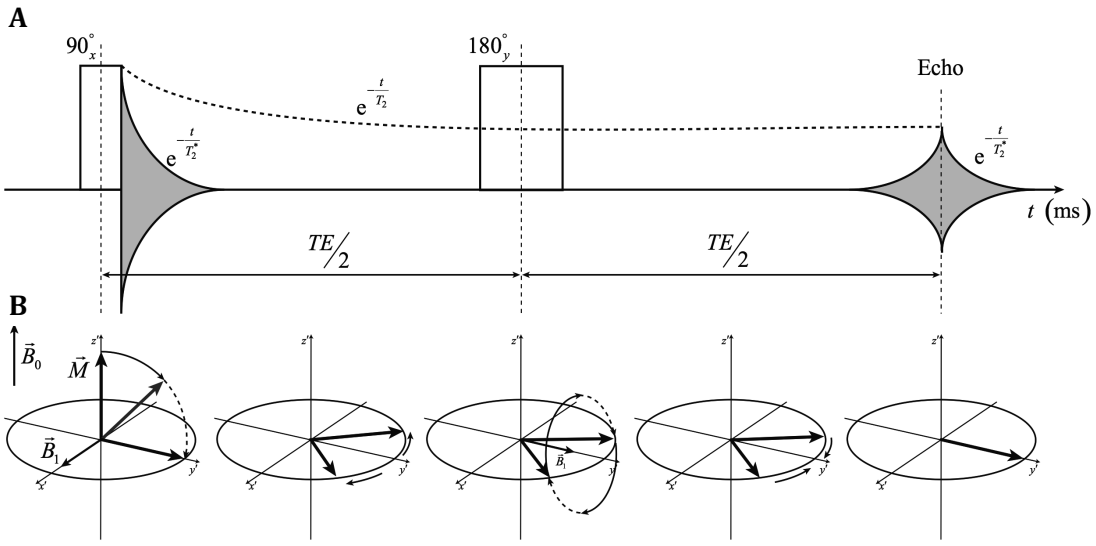

Figure 9 - (A) Spin echo radio frequency (RF) pulses and **(B)** representation of its effects on macroscopic magnetization. A 90° RF pulse is applied and flips the magnetization to the xy-plane, which starts to dephase with a time constant $\mathbf{T_2^*}$. The application of an inversion pulse after a delay TE/2 rotates the magnetization around the y'-axis, refocusing the spins and generating an echo after a delay TE/2. Even the relaxation due to fixed causes is reversed and the loss of signal results uniquely from $\mathbf{T_2}$ effects. TE: echo time. Figure taken from Kunz (2010).

2.2.7. Spin Echo

Unlike gradient echo sequences, spin echo sequences allow the separation of the contribution of T_2 and magnetic field inhomogeneity through the application of a 180° refocusing pulse. Briefly, an initial 90° RF pulse is applied, after which magnetization starts to loose coherence through T_2^* spin relaxation. After the delay TE/2, a 180° RF pulse is applied to the sample, which causes magnetization vector to rotate about y by 180°. Therefore, although spins continue to dephase, rotating at their local Larmor frequencies, after the 180° inverting pulse, instead of spreading further apart, they move closer together, being refocused along the y'-axis at the end of the second TE/2 delay to form a spin echo. During the inversion pulse, the slice selection gradient is repeated, improving the localization of the signal. Furthermore, since the refocusing pulse is applied, the second frequency encoding gradient pulse is of the same polarity as the prephasing gradient. At the top of the echo, the effects of the B_0 magnetic field inhomogeneities are refocused and the signal decrease is caused exclusively by inherent T_2 relaxation (Figure 9).

2.2.8. Rapid Acquisition with Relaxation Enhancement (RARE)

Through a standard fast imaging sequence - rapid acquisition with relaxation enhancement (RARE) - images can be acquired by exciting spins and refocusing the spins repeatedly with 180° pulses to give a series of independently phase-encoded spin echoes. Thereby, every single excitation pulse allows the acquisition of several lines of *k*-space. As expected, the signal strength decreases as the transverse magnetization decays (Figure 10); still, it represents a fast imaging technique producing high quality T_2-weighted images.

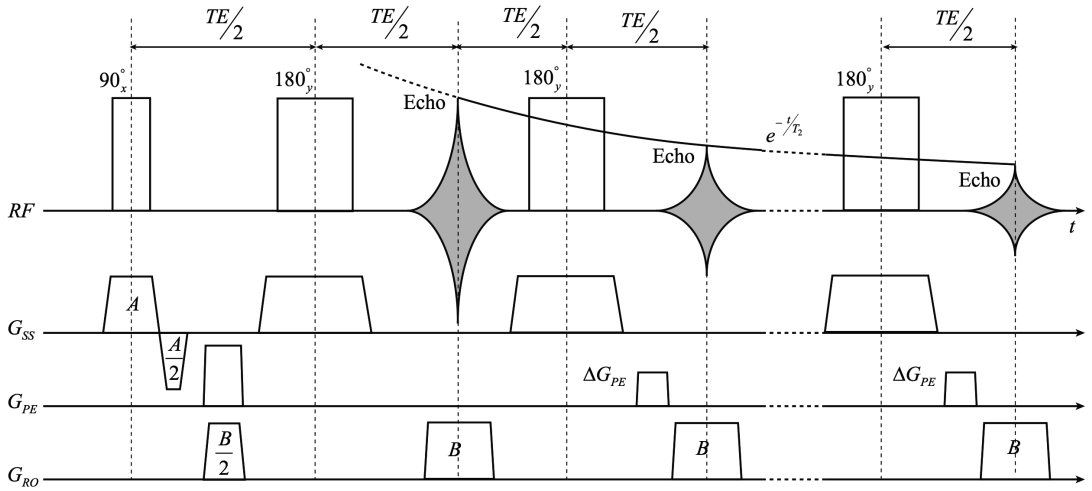

Figure 10 - Fast spin echo, an example of a rapid acquisition with relaxation enhancement (RARE) sequence. It is based on a spin echo sequence and starts with a 90° excitation pulse together with a slice selective gradient (G_{SS}). It allows the acquisition of multiple spatially encoded echoes through the sequentially application of inversion pulses. Obviously, the magnetization decays with $\mathbf{T_2}$ and so the amplitude of echoes, but this operation can be repeated as long as the echo amplitude is above the noise level. Figure taken from Kunz (2010).

2.3. ^{1}H MRS

Since nearly all metabolites contain protons, *in vivo* ^{1}H MRS is in principle a powerful technique to observe, identify and quantify a large number of biologically important compounds in intact tissues. The detection and quantification of a wide range of metabolites has led to the characterization of disease progression, allows the study of intervention by medication or surgery and identification or categorization of diseases by observing specific metabolic markers.

Up to now, it was assumed that the macroscopic magnetization was the sum of a population of spins having all the same resonant frequency. Following the Equation (2.13), nuclei of the same element (or isotope) even in different molecules, would resonate at the same frequency because of their

identical gyromagnetic ratio γ. Fortunately, however, besides depending on the gyromagnetic ratio γ and the external magnetic field B_0, the resonant frequency ω_0 is also highly sensitive to the chemical environment of the nucleus under investigation. This is commonly referred to as the chemical shift and can be used as a fingerprint to identify molecules.

2.3.1. Chemical Shift

The phenomenon of chemical shift is caused by the partial shielding of nuclei from the external magnetic field by electrons surrounding them. When placed in an external magnetic field, the electrons will rotate about $\overrightarrow{B_0}$ in an opposite sense to the proton spin precession. Since this movement of electrons involves motion of charge, there will be an associated magnetic moment μ_e that opposes the primary applied magnetic field $\overrightarrow{B_0}$ (Figure 11). Therefore, the electrons will reduce the magnetic field that is sensed by the nucleus, which can be expressed in terms of an effective magnetic field B_e at the nucleus:

$$B_e = B_0(1 - \sigma) \tag{2.46}$$

where σ is the shielding constant depending on the chemical environment of the nucleus. Thus, the Larmor frequency of a shielded nucleus is given by:

$$\omega_0 = \gamma B_0(1 - \sigma) \tag{2.47}$$

Because every chemically different nucleus has a different electronic environment, each one will resonate at a slightly different frequency. The Fourier transform of the echo gives a representation of the signal in the frequency domain (spectrum of resonances) and its result can be approximated by a Lorentzian lineshape centered at each resonant frequency

and with area under the peak proportional to the spins population. Usually, there is more than one hydrogen atom in a different chemical environment in a compound of interest. This leads to more than one resonance per compound.

Chemical shifts are expressed in parts per million (ppm), given that the differences in resonant frequency due to the chemical shift are usually small. Besides, expressing chemical shifts in ppm makes them independent of the strength of the magnetic field $\overrightarrow{B_0}$ applied and, therefore, comparable between different NMR instruments. The chemical shift δ is defined as:

$$\delta = \frac{\nu - \nu_{ref}}{\nu_{ref}} \times 10^6 \tag{2.48}$$

where ν and ν_{ref} are the resonant frequencies of, respectively, the compound under investigation and a reference compound, typically tetramethylsilane (TMS) for ^{1}H MRS to which $\delta = 0$ has been assigned. The reference compound should ideally be chemically inert and its chemical shift should be independent of external variables, such as temperature, and should produce a strong resonance signal well separated from all other resonances.

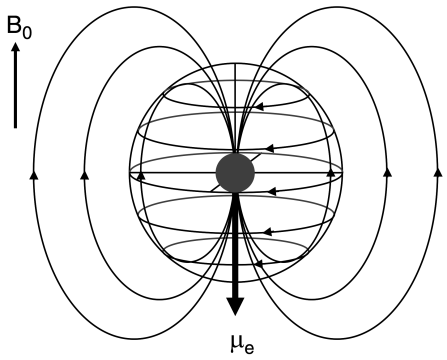

Figure 11 - Origin of the chemical shift. The electrons surrounding a nucleus can be regarded as small currents, giving rise to a magnetic moment $\boldsymbol{\mu_e}$ at the nucleus. Since the magnetic moment opposes the external magnetic field, the effective magnetic field at the nucleus is reduced, thereby leading to different Larmor frequency and hence a different chemical shift. Figure taken from de Graaf (2008).

2.3.2. Spin-Spin Coupling

Some resonances, on closer inspection, can be seen as one lineshape consisting of more than one peak. Besides being influenced by its own microscopic environment, i.e. the electrons around it, the nuclear spin is also affected by the surrounding nuclear spins. Spin-spin coupling originates from the fact that nuclei with magnetic moments can influence each other, besides directly through space (dipolar coupling) also through electrons in chemical bonds (scalar coupling). On a liquid environment, the dipolar coupling is canceled out due to the rapid molecular tumbling. However, the interactions through the electrons that form chemical bonds do not average to zero and give rise to the phenomenon of scalar coupling or, also termed, J-coupling.

J-coupling can be understood as a chain reaction from one nuclear to the next in a bonded network. The electrons taking part in the covalent bond propagate the influence of one nuclear spin on another. However, equivalent nuclei, i.e. nuclei having the same physical and chemical attributes cause no interaction with one another and, therefore, no J-coupling effects are observed. Let us consider two covalently bonded nuclei A and X with a nuclear spin ½ resonating at a frequency ν_A and ν_X, respectively. The electrons in this bond have to be antiparallel to one another according to the Pauli exclusion principle, which states that two identical fermions cannot occupy simultaneously the same quantum state. In addition, electrons in the s orbitals have a high probability of being close to the nucleus, with which they interact through the so-called Fermi contact interaction. This interaction energetically favors the antiparallel over the parallel arrangement of nuclear and electronic spins. However, nuclear spins can arrange themselves in any of these four combinations of spins states: αα, αβ, βα and ββ, where αα and ββ represent, respectively, the parallel and antiparallel alignment of both nuclear spins with the external magnetic field $\overrightarrow{B_0}$. These two states become energetically less favorable, since the two bonding

electrons cannot be both antiparallel to the nuclear spins (Figure 12.A). As a result for the nucleus A, the state (up or down) of the nucleus X influences its magnetic energy levels by splitting each of them into two, giving rise to two different transition energies ΔE between the states up and down of the nuclear spin A. This is reflected in the spectrum by a splitting of the resonance of the nucleus A into two lines, a doublet, centered at the resonant frequency of the nucleus A, ν_A, and separated by the characteristic coupling constant between nuclei A and X, J_{AX}, which is expressed in hertz and determines the strength of the force exerted in a interaction. The same process takes place for the nucleus X (Figure 12.B). The intensity of the two peaks of the doublet is equal in the case of a weakly coupled system, which is defined as:

$$|\nu_A - \nu_X| \gg J_{AX} \tag{2.49}$$

When more nuclei are coupled to each other through J-coupling, more complex patterns will appear. Depending on the magnetic equivalence of the coupled nuclei, the coupling can give rise to triplets, quadruplets or doublet of doublet patterns. Take for example a spin system comprising three non-equivalent nuclei, A, M and X, which have a large difference in resonant frequency between one another. The patterns of the nucleus A and X are only affected by M and, so, each pattern consists of a doublet whose peaks are split by J_{AM} and J_{XM}, respectively. On the other hand, M is affected by both A and X, originating a pattern split into four peaks of equal intensity, termed a doublet-of-doublets.

The total area of all the multiplets of a given resonance is proportional to the magnetization of the corresponding nucleus and, thus, to its concentration. However, the application of ^{1}H MRS to intact tissues is challenging for a number of reasons. Firstly, the water resonance is several orders of magnitude larger than the low concentration metabolites, making

metabolite detection difficult and ambiguous. Secondly, other large signals like extracranial lipids can also overwhelm small metabolite signal and thirdly, heterogeneous magnetic field distributions significantly decrease the spectral resolution.

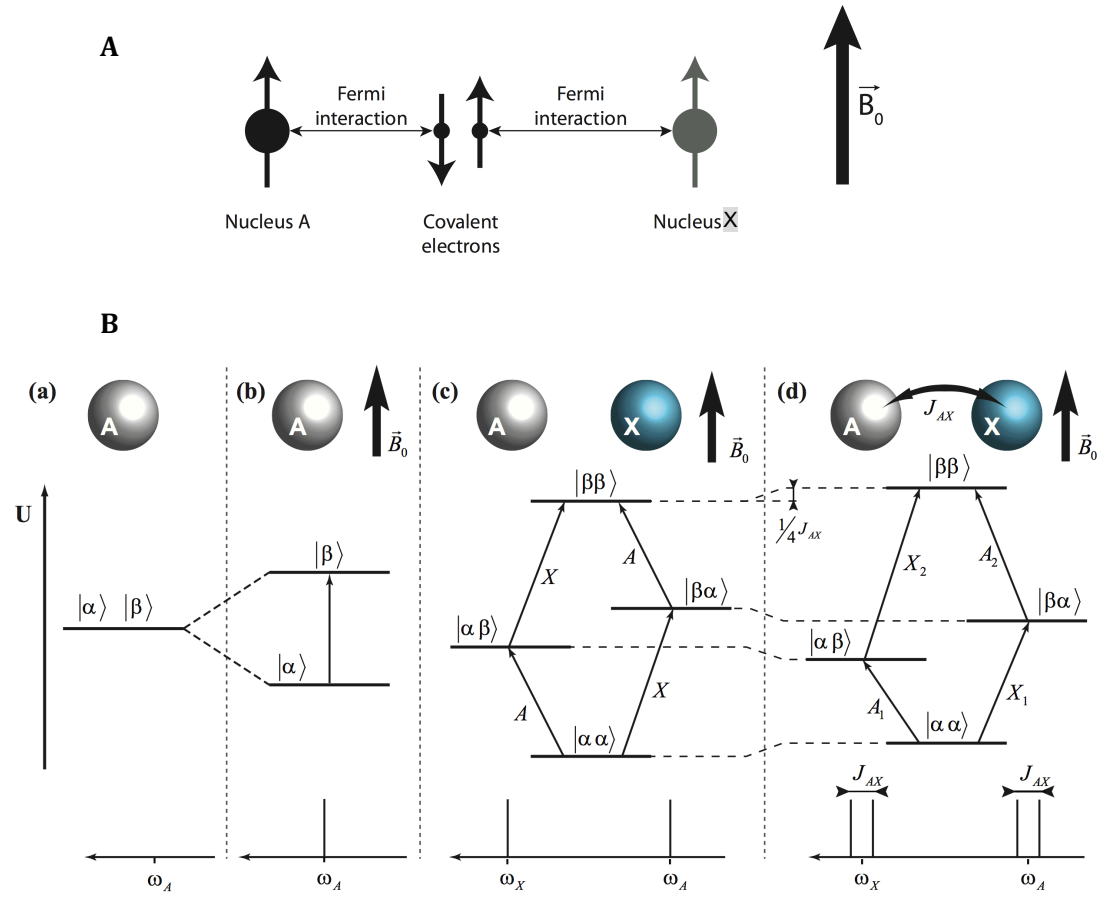

Figure 12 - J-coupling interaction between neighboring nuclei. **(A)** Representation of the αα state between two non-equivalent nuclei, A and X, with the respective nuclear and electronic arrangement. Figure taken from Lanz (2012). **(B) (a)** Nucleus in absence of a static magnetic field ($\overrightarrow{\mathbf{B_0}}$). **(b)** Nucleus in the presence of $\overrightarrow{\mathbf{B_0}}$ magnetic field. **(c)** Two unbounded non-equivalent nuclei, A and X, in the presence of $\overrightarrow{\mathbf{B_0}}$ magnetic field, characterized by two transition frequencies pertaining to changing of the spin state of either A or X. **(d)** The same two nuclei experiencing J-coupling due to chemical bonding, characterized by four separate transition frequencies, where each of two previous transition frequencies have been increased and decreased by a value of ½J_{AX}. J_{AX}: coupling constant between A and X. Figure taken from Kunz (2010).

2.3.3. MRS Experimental Design

These previously mentioned obstacles in obtaining a spectrum of quality can be minimized by integrating water suppression, localization and shimming routines in the MRS experiment before the acquisition of the signal.

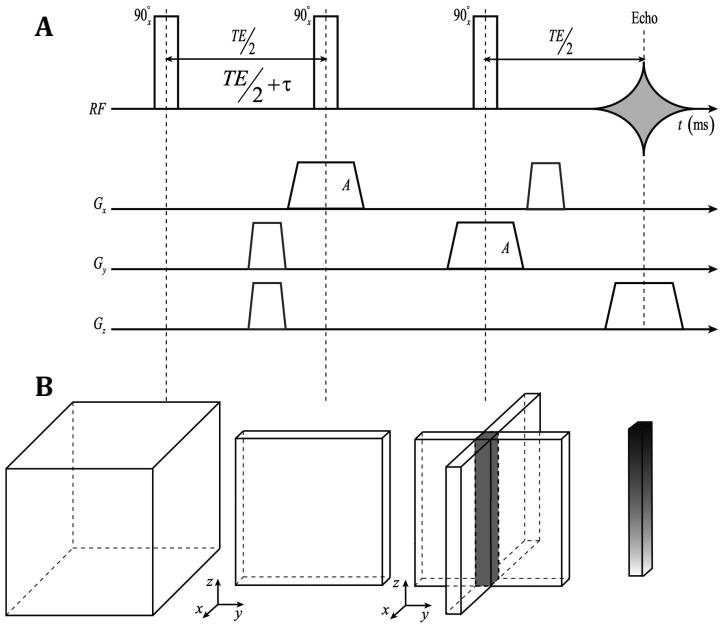

Figure 13 - (A) FASTMAP (fast automatic shimming technique by mapping along projections) pulse sequence and **(B)** correspondent column selection and frequency encoding. It starts with a non-selective 90° radio frequency (RF)-pulse, followed by two slice selection pulses. It results in the selection of a column, which is spatially encoded with a frequency gradient along its height. The measurement is repeated by adding a delay τ during the first TE/2 period. The phase difference between the two obtained signals is then estimated, providing a mapping of the static magnetic field ($\mathbf{B_0}$) inhomogeneities along the column. TE: echo time. Figure taken from Kunz (2010).

2.3.3.1. Active Shimming

Shimming is an essential step in a MRS experiment and is designed to provide an optimal $\overrightarrow{B_0}$ homogeneity in the VOI, making it possible to

investigate spectral fine *in vivo* structures, such as J-coupling splitting or resolving overlapping of adjacent resonances.

To correct for $\overrightarrow{B_0}$ inhomogeneities, a magnetic field mapping is first required, based on which a calculation of the needed corrections and application of the estimated currents in the shim coils to generate the desired magnetic field can be made. The $\overrightarrow{B_0}$ inhomogeneities minimization procedure is usually performed by fully automated, iterative methods based on quantitative magnetic field maps. FASTMAP (fast automatic shimming technique by mapping along projections) (Gruetter, 1993) is based on the notion that once the magnetic field is decomposed in spherical harmonics, mapping the effective field along six directions is sufficient to have an accurate estimation of the correction to apply in the entire VOI. Therefore, FASTMAP is a time-efficient shimming routine since it reduces the acquisition of a complete image of the external magnetic field B_0 to projections acquired along a set of noncollinear axes. The technique maps the effective magnetic field along a column of the sample by acquiring two times the same projection with the acquisition delayed by a time τ in the second acquisition (Figure 13). The delay added during the second acquisition results in a phase difference between the two signals that is proportional to the B_0 inhomogeneities.

2.3.3.2. Water suppression and Outer Volume Suppression (OVS)

In vivo MRS is a very challenging technique that is designed to quantify metabolite signals that are 10 000-fold smaller and overlapping that of water. In addition, the signal should be localized in a region 100-fold smaller than the sample size. Therefore, most of the signal generated during the experiment is unwanted and must be suppressed to provide a good SNR and avoid contamination from outer volume signals.

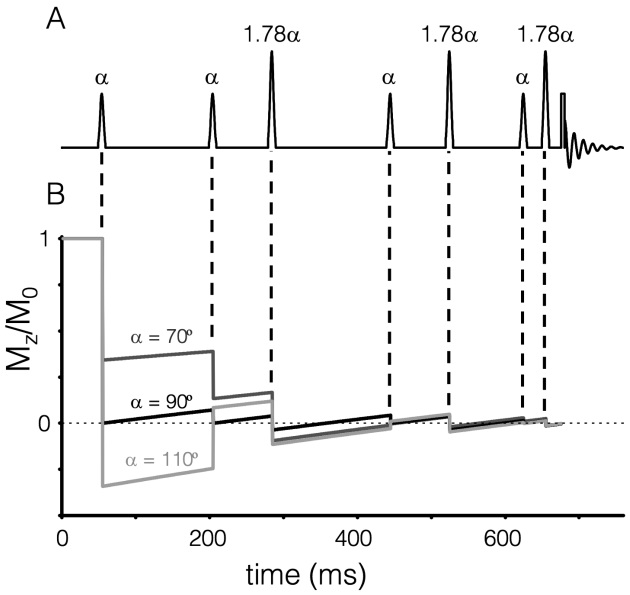

Figure 14 - Principle of variable power RF pulses with optimized relaxation delays (VAPOR) water suppression. **(A)** The specific radio frequency (RF) pulse and delay combination used in VAPOR leads to a water suppression largely independent of the nutation angle α. **(B)** Longitudinal magnetization ($\mathbf{M_Z}$) trajectory for $\boldsymbol{\alpha} = \mathbf{70}°$, 90° and 110° are shown ($\mathbf{T_1} = \mathbf{1500\ ms}$) and all end up close to zero at the end of the sequence. Figure taken from de Graaf (2008)**.**

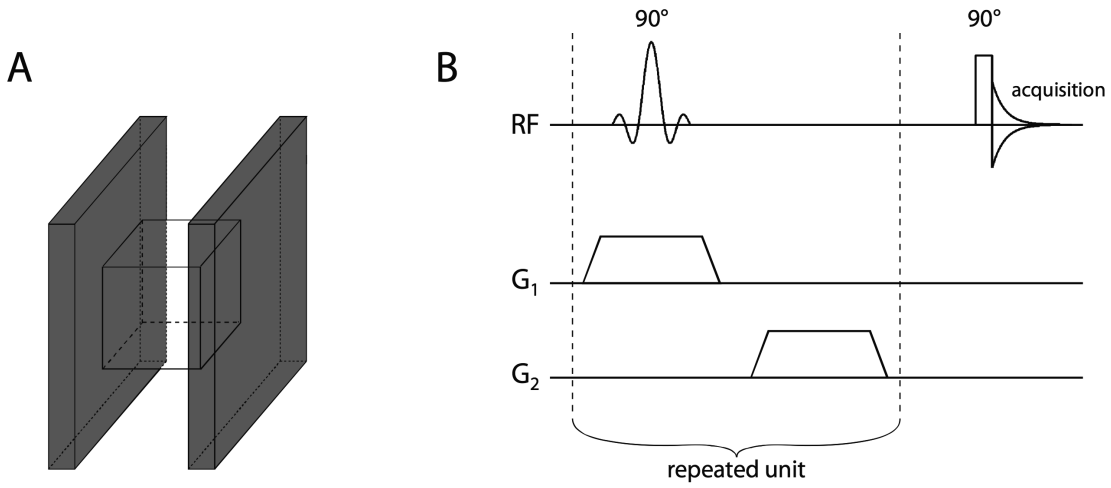

Figure 15 - OVS (outer volume suppression) localization on NMR spectroscopy. **(A)** The NMR signal is localized by successive excitations and dephasing of the magnetization in slices surrounding the VOI. **(B)** Each slice is selected with the gradient $\mathbf{G_1}$ and spoiled with the gradient $\mathbf{G_2}$. Figure taken from Lanz (2012).

Water is the most abundant compound in mammalian tissue and, as result, the proton NMR spectrum of almost all tissues is dominated by a

resonance at circa 4.7 ppm originating from the two protons of water. VAPOR (variable power RF pulses with optimized relaxation delays) is a water suppression technique designed to minimize sensitivity to $\overrightarrow{B_1}$ inhomogeneities. In addition, VAPOR is insensitive towards variations in T_1 relaxation. It consists of seven frequency selective RF pulses interspersed with optimized T_1 recovery delays. For a nutation angle α of 90°, the longitudinal magnetization of water prior to nonselective excitation ends up very close to zero despite the presence of T_1 relaxation. And even when the nutation angle is not calibrated correctly, the magnetization ends up close to zero due to the optimized pulse and delay combination (Figure 14).

Outer volume suppression (OVS) is an example of destructive localization. Prior to spectrum acquisition, a series of slice selective RF pulses excite narrow slices situated around the desired VOI, using an appropriate gradient for the slice selection. Following each slice-selective excitation, the transverse magnetization is dephased ("spoiled") by a subsequent magnetic field crusher gradient (Figure 15). The result of this dephasing is a zero net magnetization in the corresponding slices.

This technique is versatile, as the selected suppression bands can be rotated, shifted and changed in size arbitrarily by adapting the excitation RF pulse and gradient. However, it is limited by the T_1 recovery of the magnetization in the different slices before the actual acquisition sequence starts. OVS is often used in combination with other localization techniques.

Localization can be achieved in two distinct ways: by leaving the magnetization in the VOI unperturbed during the localization procedure and remove the unwanted external signal (destructive localization), which is the case of OVS, or by selectively exciting the signal in the VOI using a successive excitation of three orthogonal slices which intersection corresponds to the VOI, so that only the magnetization in the VOI generates signal (constructive localization).

2.3.3.3. Localization – SPin ECho, full Intensity Acquired Localized (SPECIAL) Sequence

The use of a gradient field enables a one-dimensional spatial selection, allowing the excitation of the magnetizations located in a sample slice. Constructive localized spectroscopy has been largely based on stimulated-echo acquisition mode (STEAM) or point-resolved spectroscopy (PRESS) methods. However, the SPin ECho, full Intensity Acquired Localized (SPECIAL) spectroscopy sequence (Mlynárik et al., 2006) is associated with improved localization performance and sensitivity. When used at high magnetic field strength with ultra-short TEs and sufficiently good shimming, approximately 21 metabolites can be detected and quantified accurately. High magnetic field affords increased intrinsic SNR (increased sensitivity), chemical shift dispersion (increased spectral resolution) and decreased strong coupling effects; it is useful for low concentration metabolites, strongly overlapped metabolites and for metabolites having complex multiplet patterns, leading to an improved quantification precision and accuracy. The ultra-short TE ensures the obtention of high quality spectra, with resolved lines of many metabolites due to minimal phase distortions of multiplets of coupled spin systems, and the minimization of signal loss due to T_2 relaxation, thus increasing the amount of biochemical information and contributing to a more precise quantification. In addition, acquisitions with a long TR minimize T_1 relaxation (Cudalbu, 2013).

The SPECIAL sequence (Figure 16) is based on a combination of the 1D image-selected *in vivo* spectroscopy (ISIS) technique and a slice-selective a spin-echo sequence.

The three-dimensional (3D) ISIS localization method employs three frequency-selective inversion pulses in the presence of three orthogonal magnetic field gradients. The inversion pulses are turned on or off according to a specific encoding scheme. For one-dimensional (1D) ISIS localization,

two experiments are required: one with and one without a spatially selective inversion pulse prior to excitation. Subtraction of the two datasets will only give signal from the localized volume. When zero or an even number of 180° pulses are executed, the desired magnetization in the cross-section of the three selected slices ends up along the positive longitudinal axis and following a $90°_{-x}$ excitation pulse will end up along the positive y'-axis. During a scan with an odd number of 180° pulses, the desired magnetization ends up along the negative longitudinal axis and is excited to the negative y'-axis by a $90°_{-x}$ pulse. Adding and subtracting the individually stored scans with even and odd number of 180° pulses, respectively, will constructively accumulate signal from the desired location while destructively canceling signal from all other locations.

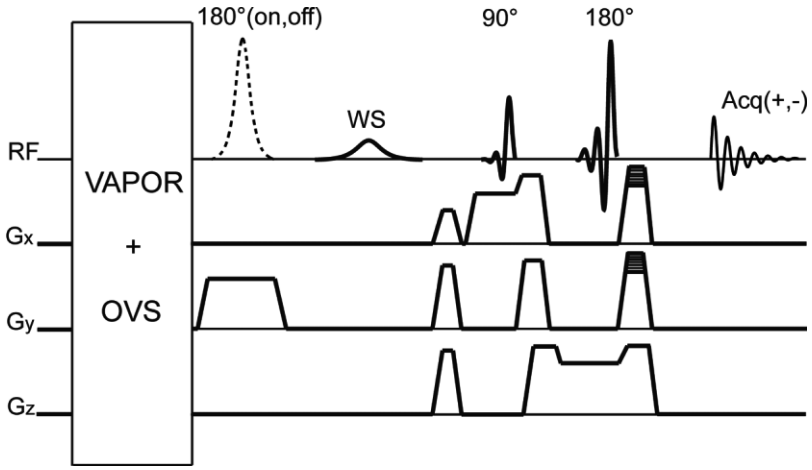

Figure 16 - SPin ECho, full Intensity Acquired Localized (SPECIAL) sequence, water suppression and outer volume suppression (OVS), followed by the one-dimensional (1D) image-selected *in vivo* spectroscopy (ISIS) consisting of a 180° pulse that is turned on and off according to a defined scheme. A second water suppression module (WS) then precedes the excitation and is followed by the Spin Echo (90 and 180° RF pulses) and finally the acquisition (Acq). Figure taken from Mlynárik et al. (2006).

The SPECIAL sequence uses a 2-ms slice-selective adiabatic 180° pulse in the y-direction in alternate scans, followed by a spoiling gradient to remove the potential transverse magnetization. Then a spin echo sequence is

applied using 0.5-ms 90° excitation and 1ms 180° inversion asymmetric slice-selective pulses in the x and z directions. Water signal suppression is accomplished by a series of seven 25-ms asymmetric VAPOR that are interleaved with OVS consisting of three modules of 1.2-ms adiabatic pulses. To further improve the efficiency of water suppression, another 15-ms Gaussian frequency-selective saturation pulse is added in the delay between the adiabatic slice-selective inversion pulse and the spin echo modules.

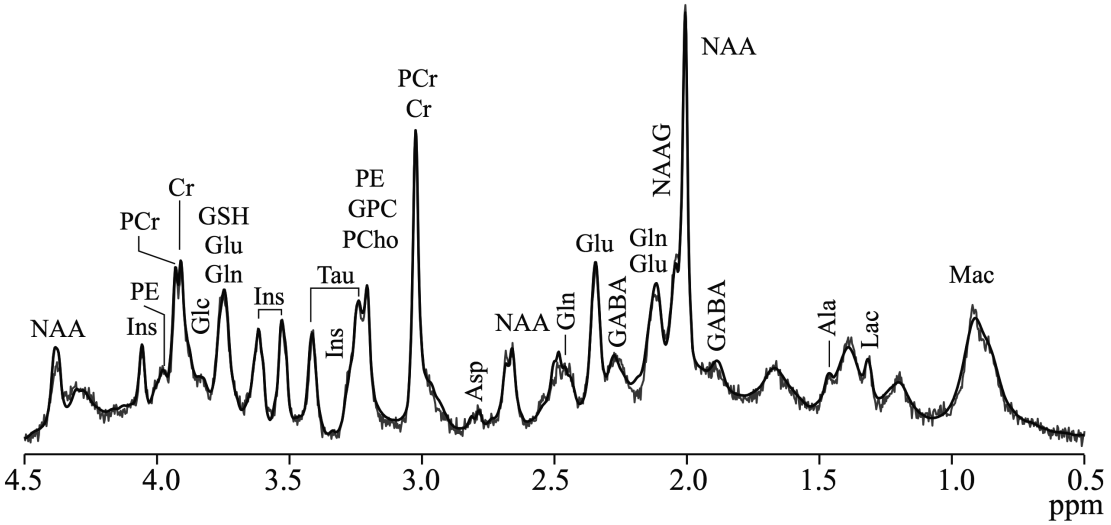

Figure 17 - ^{1}**H** NMR spectrum of the brain cortex of a rat acquired with SPECIAL (**TE = 2.8 ms**). Figure taken from Kunz (2010). NAA: N-acetyl aspartate; Ins: myo-inositol; PE: phosphorylethanolamine; PCr: phosphocreatine; Cr: creatine; Glc: D-glucose; GSH: glutathione; Glu: glutamate; Gln: glutamine; Tau: taurine; GPC: glycerophosphorylcholine; PCho: phosphorylcholine; Asp: aspartate; GABA: γ-aminobutyric acid; NAAG: N-acetylaspartylglutamate; Ala: alanine; Lac: lactate; Mac: macromolecules.

2.3.4. Metabolites and Biochemistry

Advances in MRS have made it possible to obtain, with continual improvements in resolution, non-invasive information about the biochemistry of the human brain. The resulting magnetic resonance spectrum is derived from a mixture of compounds (Figure 17), being of interest in the context of this thesis, the ones involved on osmoregulation,

neurotransmission, and antioxidant and energy metabolisms. However, the biochemical relationships that underlie changes in brain metabolites are fully interconnected and complex and, therefore, there are multiple possible causes for this modifications.

2.3.4.1. Osmoregulation

2.3.4.1.1. Choline-containing Compounds (Total Choline, tCho)

tCho give rise to a strong singlet resonance at 3.2 ppm originating from nine equivalent methyl protons, which contains contributions from free choline, glycerophosphorylcholine (GPC) and phosphorylcholine (PC, PCho). Small resonance differences between the compounds can be observed between 3.5 ppm and 4.3 ppm arising from the methylene protons signal (de Graaf, 2008).

Uptake of choline from extracellular fluids is essential, since brain cannot synthetize choline de novo. Choline is transported through the BBB by a carrier-mediated process that is unsaturated at physiological levels and is hence sensitive to alterations in plasma choline. In mammals, new choline is mostly produced by the liver, although it can be also supplied by the diet (Rae, 2014).

Requirement for choline is especially high under conditions of high growth, mainly during the development, such that choline supply affects brain development and is required for normal development of memory (Rae, 2014).

Correlations have been reported between the tCho resonance and brain function, namely in abstinent alcoholics, taking into account that the increase in tCho resonance correlated positively with mental performance, probably due to previous dietary deficiencies (Rae, 2014). Decreased choline

signals are further associated with liver disease. Choline-containing compounds are involved in pathways of phospholipid synthesis and degradation, thereby reflecting membrane turnover (de Graaf, 2008).

2.3.4.1.2. Cr

The ^{1}H NMR spectra of Cr and its phosphorylated product PCr, together often referred to as "total creatine", are very similar. While their methyl protons produce an undistinguishable singlet resonance at 3.03 ppm, the difference between the Cr (3.913 ppm) and PCr (3.930 ppm) methylene singlet resonances is large enough to separate the two compounds at magnetic fields equal or higher than 7T (de Graaf, 2008).

Cr and PCr are interconverted by the enzyme CK in reactions catalyzed in both mitochondria and cytosol by appropriate isoforms of the enzyme and through the use of ATP or adenosine diphosphate (ADP)+ ^{1}H, depending on the direction of the reaction. Cr in the body is derived both from diet, being present exclusively in meat, and from synthesis. The brain is capable of synthetizing Cr and the two main enzymes are present in neurons and glia. As mentioned in Chapter 1, Cr enters the brain via a Na^{+}-dependent transporter, SLC6A8, which also allows the passage of the precursor of Cr, guanidinoacetate. The regional distribution of Cr and of the Cr transporter follows the expression of CK, which is highest in areas of highest synaptic activity (Rae, 2014).

As also mentioned in Chapter 1, there is evidence for low Cr levels to play a role in HE. In fact, besides its energetic role, Cr acts as an organic osmolyte in the brain, serving a more dominant role as the brain matures. In addition, supplementation with Cr in rats is associated with an increase in the brain Ins signal, probably because of increased water retention. Besides, the many reported cognitive and neuroprotective effects of Cr may be related

with the neuronal activity modulation by acting at receptors, namely the NMDA and GABA ones (Rae, 2014).

2.3.4.1.3. Glutamine (Gln)

As mentioned in Chapter 1, Gln (2-amino-4-carbamoylbutanoic acid) markedly increases during hyperammonemia and, under those conditions, brain Gln is a good indicator of the liver disease HE. Gln is an amino acid present in relatively high concentrations in the brain and cerebrospinal fluid. Besides its previously addressed major role in the brain as a by-product of Glu neurotransmission, Gln is the main source of carbon backbone for synthesis of GABA (Rae, 2014).

Gln is structurally similar to Glu, resulting in similar chemical shifts and scalar coupling interactions represented by a methine proton resonance triplet at 3.76 ppm and multiplets between 2.12 ppm and 2.46 ppm, corresponding to the four-methylene protons resonance. In order to understand the important roles of Glu and Gln in intermediary metabolism, the separate detection of these compounds is essential and has been greatly benefited by the increase in magnetic field strength (de Graaf, 2008).

2.3.4.1.4. Myo-Inositol (Ins)

Ins is by far the most prevalent isomer of hexahydroxycyclohexane, comprising 95% of inositols in the human body. It is acquired both by synthesis (mainly in the kidney) and by ingestion, although it can be derived by de novo synthesis from Glc in the brain. It crosses the BBB by simple diffusion and by a stereospecific, saturable transport system. In cultured cells and immortal cell lines, the level of Ins in astrocytes is higher than in neurons. Ins is a cyclic sugar alcohol, constituent of phosphoglycerides and hence lipid component of biomembranes. Additionally, it is the major

component of intracellular second messenger system and an organic osmolyte, involved in the maintenance of cell volume. Dietary supplementation with inositol has been used to treat a range of psychiatric and behavioral conditions, although the precise mechanism of action remains undetermined (Rae, 2014). Altered levels of Ins have been encountered in patients with mild cognitive impairment and Alzheimer disease, and brain injury (de Graaf, 2008).

Ins contains six NMR detectable methine protons that give rise to four groups of resonances: a doublet-of-doublets centered at 3.52 ppm and triplets at 3.27 ppm, 3.61 ppm and 4.05 ppm (de Graaf, 2008).

2.3.4.1.5. Taurine (Tau)

The exact function of Tau is not known, but it has been proposed as an osmoregulator and a modulator of neurotransmitter action. Tau is present in all cells of the CNS, but is spatially heterogeneous, with higher levels in the olfactory bulb, retina and cerebellum. Its concentration is age-dependent, since it decreases from birth to adulthood. It is largely obtained through food, but it is an amino acid and it can be synthetized from other sulfur-containing amino acids (de Graaf, 2008).

At higher magnetic fields Tau gives two triplets centered at 3.25 and 3.42 ppm arising from the two methylene groups with non-equivalent protons (de Graaf, 2008).

2.3.4.2. Neurotransmission

2.3.4.2.1. Aspartate (Asp)

Asp is an amino acid that acts as an excitatory neurotransmitter. It does not cross the BBB, but is instead synthetized from Glc and possibly other precursors (de Graaf, 2008).

While the methine group gives a doublet-of-doublets at 3.89 ppm, the methylene group protons originate a pair of doublet-of-doublets at 2.65 and 2.80 ppm (de Graaf, 2008).

2.3.4.2.2. Glu

Glu (2-aminopentanedioic acid) is an amino acid present in the brain in relatively high concentrations and with multiple roles *in vivo*. Glu is the major excitatory neurotransmitter in mammalian brain. The central role of Glu in the Glu-Gln neurotransmitter cycle was previously addressed in Chapter 1. Glu has four major subtypes of neurotransmitter receptor: three ionotropic receptors named after the compounds originally used selectively to activate them (NMDA, AMPA and Kainate) and mGluR, some of which previously mentioned as treatment targets in HE (see Treatment Options for HE in Chapter 1). Furthermore, Glu is the direct precursor for the major inhibitory neurotransmitter, GABA, and is also an important component in the synthesis of other small metabolites (e.g. the redox peptide GSH), as well as larger peptides and proteins. Glu can be neurotoxic, mostly through its actions at NMDA receptors, where it can cause mitochondrial apoptosis through the release of Ca^{2+} (Rae, 2014).

Glu has a complex NMR spectrum with signal spread out over many low intensity resonances, with a doublet-of-doublets at 3.75 ppm, which

arises from the methine proton signal, and multiplets between 2.04 and 2.35 ppm, conferred by the two methylene protons resonances (de Graaf, 2008).

2.3.4.3. Energy Metabolism

2.3.4.3.1. Alanine (Ala)

Ala is an amino acid, and its concentration is found increased following ischemia (de Graaf, 2008). In fact, Ala and pyruvate are interchangeable by a transamination reaction, thus linking Ala to metabolic pathways, such glycolysis and gluconeogenesis. It also arises together with Lac in muscles during periods of decreased oxygen, and passes to the liver where it generates Glc from protein via the Ala cycle.

Its spectrum of resonances presents a doublet resonance at 1.47 ppm and a quartet at 3.78 ppm, both arising from the coupling of the three methyl protons to a single methine proton (de Graaf, 2008).

2.3.4.3.2. Cr and Phosphocreatine (PCr) (see above)

2.3.4.3.3. Lactate (Lac)

Lactic acid (2-hydroxypropanoic acid) exists mainly in anionic form (Lac) *in vivo*. It is the end-product of anaerobic glycolysis and is synthetized from pyruvate by the enzyme lactate dehydrogenase (Rae, 2014). Although it is normally present at low concentration, increased Lac concentrations have been observed under a wide variety of conditions in which blood flow (and hence oxygen supply) is restricted such as ischemic stroke and hypoxia. Transient increases in Lac levels have also been observed in human brain

during and following functional activation and hyperventilation (de Graaf, 2008).

Its spectrum resembles the Ala one, since the three equivalent methyl protons give rise to a doublet resonance at 1.31 ppm, while the single methine proton resonates as a quartet at 4.10 ppm (de Graaf, 2008).

2.3.4.4. Antioxidant Metabolism

2.3.4.4.1. Ascorbate (Asc)

Ascorbic acid (vitamin C) occurs physiologically as the Asc anion, a water-soluble antioxidant that is found throughout the body with the highest concentration and retention capacities in the brain, spinal cord and adrenal glands. Asc is heterogeneously distributed throughout the brain with higher concentrations in the cortex and hippocampus as compared with brain stem and spinal cord and is present in both neurons and astrocytes. It takes part in the intracellular antioxidant network and has neuroprotective properties (de Graaf, 2008).

The obtained spectrum yields a doublet at 4.49 ppm arising from a methine proton resonance, and multiplet resonances at 4.00 ppm and 3.73 ppm, associated, respectively, a methine and methylene protons (de Graaf, 2008).

2.3.4.4.2. Glutathione (GSH)

GSH (ι-γ-glutamyl-ι-cysteinylglycine) is a tripetide consisting of glycine, cysteine and Glu, and found ubiquitously throughout the body and in relatively high concentrations in the brain, as well as in the extracellular and cerebrospinal fluid. It can exist in reduced (GSH) or oxidized (glutathione disulfide, GSSG) forms and the rate GSH/GSSG is a useful indicator of the

cellular redox status. Astrocytes generally have higher GSH concentrations than neurons, although levels in some neurons are compatible with glia (Rae, 2014). GSH is an antioxidant, essential for maintaining normal red blood cell structure and keeping hemoglobin in the ferrous state. Other functions include that of an amino acid transport system, as well as storage form of cysteine (de Graaf, 2008). Furthermore, GSH depletion results in mitochondrial dysfunction and its levels decline with age.

It is problematic to measure *in vivo* concentration of GSH due to significant resonance overlap with other metabolites, which happens even at higher magnetic fields. However, it can be achieved through spectral editing methods. The spin system is characterized by a singlet resonance at 3.77 ppm derived from the methylene protons of the glycine moiety, which overlap with a doublet-of-doublets from the methine proton of the Glu moiety; multiplets at circa 2.15 and 2.55 ppm and three doublet-of-doublets at 2.93, 2.98 and 4.56 ppm (de Graaf, 2008).

2.3.5. Spectral Quantification

Spectra obtained by NMR spectroscopy can, in principle, be used to derive absolute concentrations in animal and human tissues *in vivo*. This originates from the fact that the thermal equilibrium magnetization M_0 is directly proportional to the number of spins n, according to Equation (2.18), which is proportional to the molar concentration.

There are numerous algorithms used for spectral quantification; however, in the context of this thesis, the explanation will be confined to the linear combination of model spectra of metabolites (LCModel) (Provencher, 2001), an iterative, user-dependent model fitting algorithm imposing various amounts of prior knowledge.

LCModel analyses MRS data in the frequency domain, taking into account that the total NMR signal obtained from a mixture of compounds can

be seen as a linear combination of the NMR signals from the pure or isolated compounds. Thereby, a basis set, composed by the metabolites spectral pattern, is provided as an input to LCModel. Afterwards, LCModel essentially adjust the amplitudes, frequencies, line widths and phases of the metabolite basis set to match the *in vivo* NMR spectrum as close as possible. The algorithm also imposes many soft constraints on the fitting parameters in order to achieve faster convergence. Most important is that the basis set is complete, i.e. all metabolites that are present in the *in vivo* NMR spectrum should be included in the basis set. Furthermore, the basis set should be acquired or quantum mechanically simulated under the same exact conditions as the data were, namely at the same magnetic field and with the same sequence and acquisition parameters.

The resonance area of a metabolite resonance is, in principle, proportional to the concentration, which makes the application of a reference compound with known concentration a convenient method of quantification. For ^{1}H MRS, water is often used as an internal reference, since its concentration in various part of the body is well documented. Therefore, a second spectrum containing the resonance of the calibration compound, i.e. possibly unsuppressed water, from the same VOI has to be acquired. Thereby, the resonance areas in the acquired spectrum are compared with that of a stable endogenous reference compound, by previously knowing its concentration.

CHAPTER 3

Materials and Methods

3.1. Aim

The aim of this thesis is to elucidate, separately, the protective effects of two promising therapeutic agents for CHE – VSL#3® and Cr – in BDL rats. For that purpose, *in vivo* metabolic effects on osmoregulation, neurotransmitter, and antioxidant and energy metabolisms using ^{1}H MRS were non-invasively and longitudinally analyzed.

3.2. Rationale

There is robust evidence for the pathogenesis of HE to be linked to alterations in gut microbiota and to be accompanied by a Cr deficiency. MRS techniques allow the investigation of the chronological involvement of metabolic events during the progression of CLD. Additionally, the use of *in vivo*, non-invasive and longitudinal magnetic resonance measurements is a promising tool for assessing the effects of treatments in CLD-induced HE without influencing it. This unique approach allows assessing *in vivo* and longitudinally the effects of VSL#3® and Cr on osmoregulation, neurotransmitters, and antioxidant and energy metabolisms, thereby opening new perspectives to offer appropriate treatments in HE.

3.3. Animals, Bile Duct Ligation and Treatment

All experimental procedures were performed according to both local and federal guidelines. Fourteen adult male Wistar rats (Charles River, France) were kept under a 12h light-dark cycle, with food (KLIBA NAFAG, Provimi Kliba AG, Kaiseraugst, Switzerland) and water provided ad libitum before the beginning of the treatment and afterwards.

The rats were divided into two treatment groups: VSL#3® and Cr. Animals treated with VSL#3® were housed individually, while the Cr treated ones were housed in three cages: two with two rats and one with three. To induce biliary cirrhosis, five animals in each of the groups underwent double ligation and section of the common bile duct under isoflurane anesthesia (Attane, Minrad, NY, USA), intubated and mechanically ventilated (2.5-4% isoflurane in O_2 and compressed air). In addition, two animals in each group were sham-operated. The mean body weights at the day of bile duct ligation were 197.3 ± 12.4 g and 199.9 ± 8.9 g for, respectively, the VSL#3® and Cr treated groups. The duration of the study was of eight weeks after surgery, after which rats were decapitated whilst anesthetized.

3.4. VSL#3® Treatment

The treatment with VSL#3® started two weeks prior the bile duct ligation and lasted until the end of the study, performing a total of ten weeks of treatment. Animals received a daily dose of VSL#3® of 50 billiards of bacteria/kg of body weight dissolved in water. The dose was prepared taking into account that a rat usually drinks 10 ml/day/100 g of body weight. The VSL#3® treatment was prepared freshly everyday and given to the rats in the evening, since they are naturally nocturnal animals. The VSL#3® solution intake was measured every day for each rat.

3.5. Cr Treatment

The group treated with Cr had free access to a Cr enriched diet (KLIBA NAFAG, Provimi Kliba AG, Kaiseraugst, Switzerland) at a concentration of 20g of Cr/kg of diet, which started at the bile duct ligation day and lasted until the end of the study, performing a total of eight weeks of treatment. The Cr enriched diet intake was measured once a week, per cage.

3.6. Biochemical and Histological Measurements

3.6.1. VSL#3® Treatment

Blood samples were collected from the retro-orbital plexus immediately before the surgery and two, four, six and eight weeks after surgery. Immediately after the collection, blood samples were analyzed for bilirubin and Glc levels (Reflotron Plus, Roche, Switzerland). Afterwards, blood samples were centrifuged and the plasma was collected and stored at -80 °C for further ammonia measurements at the Laboratoire de Chimie Clinique (CHUV, Lausanne), by Dr. Olivier Braissant. Ethylenediaminetetraacetic acid (EDTA) was used as anticoagulant.

Stool samples were collected before the beginning of the treatment and at the same time points as blood samples were for future measurements.

After rats' sacrifice, brain was extracted from the cranium and half of it was kept in paraformaldehyde (PFA), while the other half was stored at -80 °C for future histological studies in the Laboratoire de Chimie Clinique (CHUV, Lausanne), by Dr. Olivier Braissant. The liver was also collected, weighted and two samples of it stored in the same way as brains were for future histological studies at the same laboratory.

3.6.2. Cr Treatment

Blood samples were collected from the sublingual vein immediately before the surgery and four, six and eight weeks after surgery. Immediately after the collection, blood samples were analyzed for bilirubin and Glc levels (Reflotron Plus, Roche, Switzerland). Afterwards, blood samples were centrifuged and the plasma was collected and stored at -80 °C for further ammonia measurements in the laboratory Laboratoire de Chimie Clinique (CHUV, Lausanne), by Dr. Olivier Braissant. EDTA was used as anticoagulant.

After rats' sacrifice, brain was extracted from the cranium and half of it kept in PFA for future histological studies in the Laboratoire de Chimie Clinique (CHUV, Lausanne), by Dr. Olivier Braissant. The liver was also collected, weighted and two samples of it kept in PFA and stored at -80 °C for future histological studies at the same laboratory.

3.7. Behavioral Tests

Open Field – Novel Object behavioral tests were performed at six and eight weeks after surgery, in the morning and at the same time, in both groups of treatment. For the tests, a black arena of 100-cm diameter, divided in inner, intermediate and outer parts was used. The boundaries of the inner and intermediate parts were defined at, respectively, 12.5 and 37.5-cm radius from the center. The inner part was illuminated with 7-9 lux, while the outer part was illuminated with, approximately, 2 lux less than the one used in the center. Before starting and between tests, arena was cleaned with 5% ethanol and dried. Tests were recorded through a hardware-based realtime MPEG-2 (Moving Picture Experts Group-2) encoder secured to the ceiling above the center of the arena, and a frame-grabber software (MediaCruise, Canopus Corporation, San Jose, CA, USA).

The first part of the test, i.e. the open field task, had the duration of ten minutes and each rat was placed in the empty arena. Then, a cylindrical object was introduced in the center of the arena, yielding the second part of the test, i.e. the novel object task, which lasted five minutes. This test was performed to determine: (1) the distance moved, (2) the time spent under movement, (3) the time spent immobile, (4) the time spent in the inner part, (5) the time spent in the intermediate part and (6) the time spent in the outer part. While the first three measurements allow taking conclusions on locomotor activity, the last three allow the evaluation of the anxiety status.

3.8. *In vivo* ^{1}H MRS

^{1}H MRS was performed before and at two, four, six and eight weeks after surgery on the VSL#3® treated group. In the case of the Cr treated group, scans were performed at four, six and eight weeks after surgery.

The total duration of each scan per animal was approximately 1.5 hours. Rats were anesthetized with a dose of 4% of isoflurane and anesthesia was maintained between 1.5 and 2% until the end of the scan. The rat head was fixed in a stereotaxic system (bite bar and a pair of ear bars); then the animal was placed in an in-house-built holder and finally placed in the magnet. The vital signs of the animals were carefully monitored to provide a stable physiological condition. While an air pillow to monitor respiration was positioned under the rat, a thermosensor probe was inserted rectally.

All *in vivo* ^{1}H MRS experiments were carried out using a 9.4T MRI actively shielded system (horizontal bore diameter 31 cm) (Varian/Magnex, Palo Alto, CA). The system is equipped with an actively shielded 12-cm diameter high performance gradient insert (Varian/Magnex, Palo Alto, CA), which operates at a maximum strength of 400 mT/m, slew rate of 3000 mT/m/ms and, therefore, taking a rise time of 130 μs to achieve the maximum

strength, with eddy currents after adjustment below 0.01%. The second-order shim strengths are on the order of 3 kHz/cm^2. An home-built RF surface coil was used as transceiver coils, consisting of two single, 16-mm diameters, geometrically decoupled loops (Figure 18).

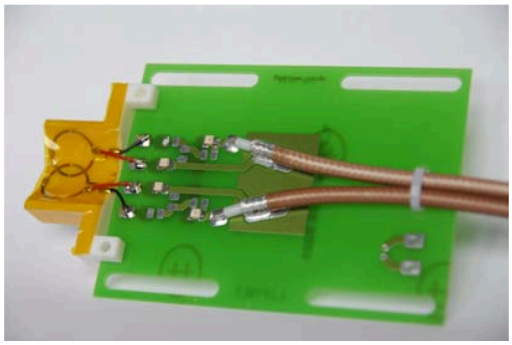

Figure 18 - An example of a proton quadrature surface coil built in laboratory.

3.8.1. Gradient Echo Sequence (GEMS)

To check the position of the rat inside the magnet, i.e. if the center of the head is close to the isocenter of the magnet and well oriented, an ultra-short gradient echo sequence was used. In each of three planes (axial, sagittal and coronal), three slices at the isocenter of the magnet were acquired. This sequence provides T_1-weighted images, since both TR and TE are short. Parameters: TE/TR: 2.99/18.91 ms, Field of View (FOV): 30 × 30 mm, acquisition matrix: 128 × 128, 3 slices, thickness = 2 mm, gap between slices = 2 mm, flip angle 20°.

3.8.2. Fast Spin Echo Sequence (FSEMS)

An FSEMS (RARE) sequence was used to provide anatomical high-resolution T_2-weighted images (long TR and TE) of the rat's brain in order to observe the position of the VOI and, therefore, place the voxel correctly for both shimming and spectroscopy experiments (Figure 19 and Figure 20).

Parameters: Effective TE/TR: 52/4000 ms, FOV: 23 × 23 mm, acquisition matrix: 256 × 256, 15 slices, thickness = 1.0 mm, gap between slices = 0.2 mm, Echo train length (ETL) = 8, Echo spacing (ESP) = 13.

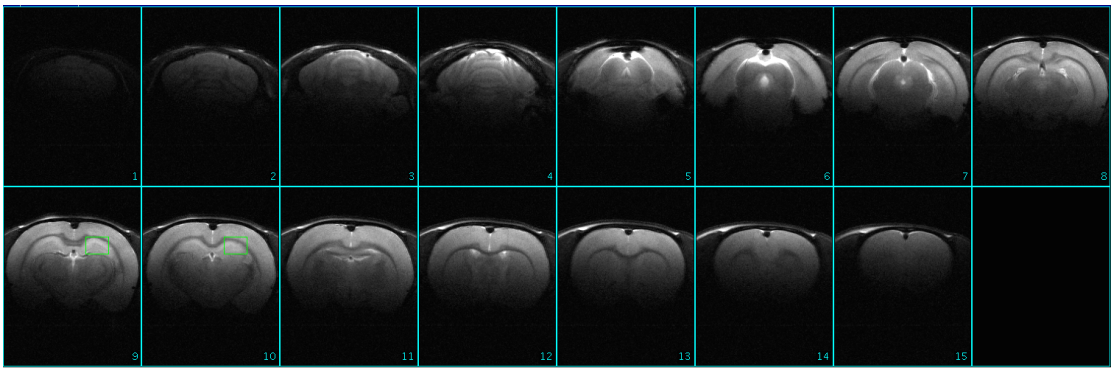

Figure 19 - Screenshot of axial images acquired with fast spin echo sequence (FSEMS), which were used for a 2 × 2.8 × 2 mm^3 voxel positioning in hippocampus. Parameters as in 3.8.2.

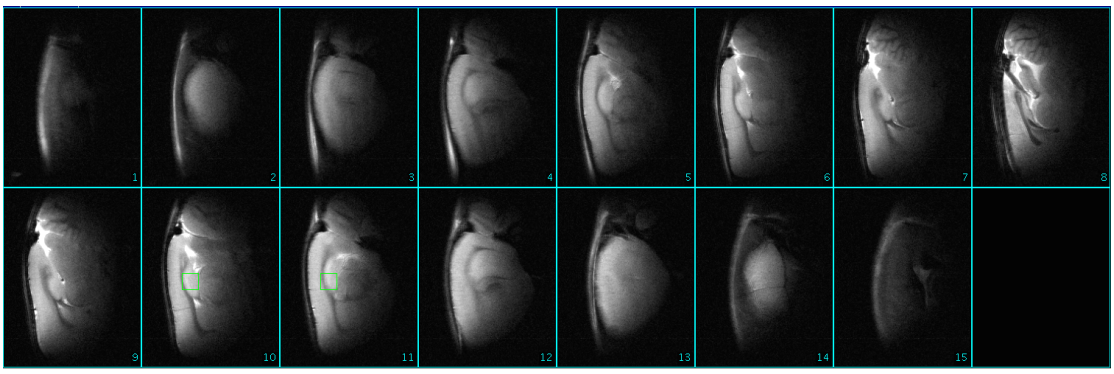

Figure 20 - Screenshot of sagittal images acquired with fast spin echo sequence (FSEMS), which were used for a 2 × 2.8 × 2 mm^3 voxel positioning in hippocampus. Parameters as in 3.8.2.

3.8.3. FAST(EST)MAP

A voxel of 2.5 × 3.2 × 2.5 mm^3 centered in the same position as the acquisition voxel was shimmed beforehand. Shimming of the voxel was done using the FASTMAP (Gruetter, 1993) , as previously introduced in Chapter 2. Firstly, $\overrightarrow{B_0}$ field is measured along *x*, *y* and *z* directions and the corrections for

$\overrightarrow{B_0}$ inhomogeneity are made by the first order shims (linear spherical harmonics). The second step does the same, but measures the magnetic field along *xy*, *yx*, *xz*, *zx*, *yz* and *zy* directions. The third step uses FAST(EST)MAP (Gruetter and Tkáč, 2000), a version of FASTMAP with performance and speed optimized. Using an approach based on asymmetric echo-planar readout gradient trains, multiple echoes are formed. Thereby, for N echoes recorded, N-1 phase maps are extracted for each projection. The third step measures the same projections as step two, the corrections are made this time by the second order shim coils (z^2, *zx*, *zy*, x^2-y^2, 2*xy*). The acquired water signal was used as an indicator of the $\overrightarrow{B_0}$ homogeneity and was decreased as much as feasibly possible.

3.8.4. SPECIAL Sequence

SPECIAL sequence (Mlynárik et al., 2006) was used for proton spectroscopy, as previously introduced in Chapter 2. The voxel used to acquire the signal was placed in the hippocampus, a region of the brain associated with memory, and had a volume of 2 × 2.8 × 2 mm^3. Parameters: TE/TR = 2.8/4000 ms, acquisition matrix = 256 × 128, 160 averages.

3.9. Quantification of Brain Metabolites

Quantification and computation of metabolite and macromolecular concentrations was performed using LCModel (Provencher, 2001), as previously introduced in Chapter 2. The basis set was measured *in vitro* using aqueous solutions of all metabolites and the same magnetic field, sequence, acquisition parameters and temperature as that *in vivo*. The internal reference used was the water signal, which was obtained during another scan

immediately after the acquisition of the metabolites spectrum with similar parameters but no water suppression. Since the concentration of water is known – 55 mol – as well as the percentage of tissue it makes up in the brain – 80% -, by comparison of the surface areas of the metabolite peaks with that of water, absolute concentration was achieved. Concentrations are given as µmol per gram of tissue. Peaks with chemical shift range between 0 and 4.3 ppm were acquired. Also calculated are the Cramer-Rao lower bounds (CRLBs). These are the lowest estimator-independent errors, and provide a measure of the reliability of each metabolite concentration result, quantitatively described as such:

for CRLB $< 10\% \Rightarrow$ sufficient precision;

for CRLB $< 20 - 30\% \Rightarrow$ consider with caution;

for CRLB $> 30\% \Rightarrow$ insufficient precision.

However, these should be taken as guideline, rather than an absolute set of rules, as the CRLB also increases with spectral overlap. Therefore, certain metabolites with similar chemical structures will always have slightly higher CRLBs.

3.10. Statistical Analysis

The two groups (animals treated with VSL#3® and Cr) were compared with previously obtained data on BDL and sham operated animals without any type of treatment. Sham-operated animals were used as controls in each group. Furthermore, individually for each rat, scans at later time points were compared with scan zero, i.e. the scan that took place before surgery. Statistical analysis was performed by student's t-test and statistical significance was taken to be $p < 0.05$. All data was presented as the mean ± standard deviation unless otherwise stated.

CHAPTER 4

Results

4.1. Treatment with VSL#3®

4.1.1. Animal Characterization

Seven adult male Wistar rats were treated with VSL#3®, five of which were BDL and two were sham-operated. Due to surgical complications, one rat died a few days after bile duct ligation. Furthermore, two rats died – one at seven and the other one at eight weeks after bile duct ligation, before the performance of the eighth MRS scan - due to cirrhotic complications.

Table 1 and Table 2 show the animal characteristics at six and eight weeks after bile duct ligation, respectively. Bilirubin levels were above the threshold associated with liver disease after bile duct ligation (0.5 mg/dl), thus confirming that the bile duct was properly ligated and that no rat recovered afterwards. With increasing time after surgery BDL rats showed a longitudinal trend of decrease of body weight and an increase of liver weight when comparing with sham-operated rats. A similar trend of decreased plasma Glc was noticed, reaching statistical significance ($p < 0.02$) at six weeks after surgery. Figure 21 shows images of two livers, taken immediately post-mortem: one from a BDL rats and the other from a sham-operated rat.

Table 1 - Characteristics of BDL and sham-operated rats treated with VSL#3®, at six weeks after surgery.

	Body Weight (g)	**Glc (mg/dl)** [#]	**Bilirubin (mg/dl)**
BDL (n=4)	316.3 ± 54.1	93.3 ± 15.8	8.5 ± 2.3
Sham (n=2)	348.5 ± 34.6	232.5 ± 64.3	< 0.5

[#] Statistically significant differences when comparing BDL and sham-operated rats ($p < 0.02$)

Table 2 - Characteristics of BDL and sham-operated rats treated with VSL#3®, at eight weeks after surgery.

	Body Weight (g)	Glc (mg/dl)	Bilirubin (mg/dl)	Liver Weight (g)
BDL (n=2)	308.0 ± 7.1	90.7 ± 24.5	5.7 ± 0.6	28.0 ± 5.7
Sham (n=2)	369.5 ± 40.3	161.0 ± 18.4	< 0.5	10.5 ± 2.1

A **B**

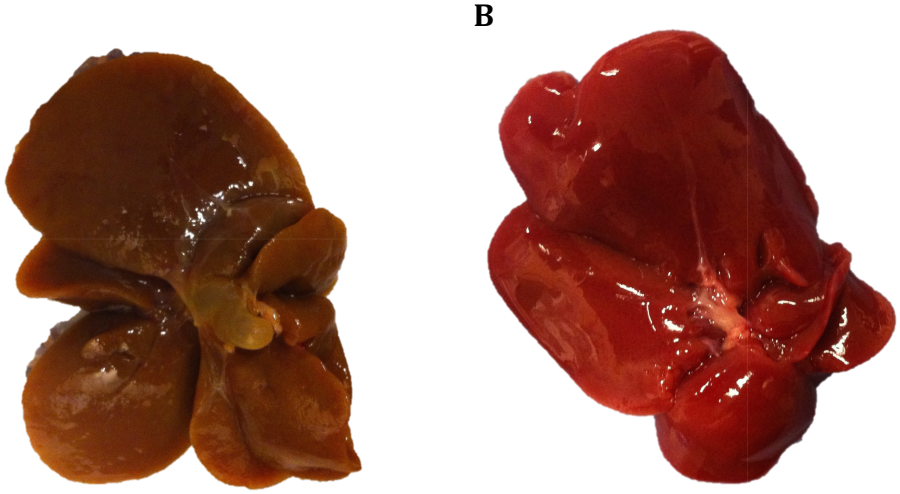

Figure 21 - Images of the liver of **(A)** BDL 139 and **(B)** sham 143. It is notorious the bile pouch formed by the bile duct ligation in the first photo, and also the difference of color and shape between the two livers, indicative of a cirrhotic liver in the first case. Images are not on the same scale.

4.1.2. Consumption of VSL#3®

A dose of 50 billiards of bacteria per kilogram of body weight was dissolved in water and given to each rat every day. The solution was prepared taking into account that a rat consumes 10 milliliters of water per 100 grams of body weight per day.

Figure 22 represents the VSL#3® solution intake per rat per day and Table 3 the body weight of each rat during the entire study. One can notice that:

1) BDL 142 did not consume, on average and based on its body weight, the expected amount of VSL#3® solution. BDL 142 was significantly heavier than the other BDL and one sham-operated rats;

2) BDL 139 significantly consumed more VSL#3® solution than the other BDL rats and one sham-operated rat;

3) BDL 141 significantly consumed more VSL#3® solution than BDL 140.

4) BDL 140 significantly weighted less and consumed less VSL#3® solution than the other animals.

No statistically significant differences were observed comparing BDL 139 with BDL 141 and sham-operated rats concerning body weight. Furthermore, sham-operated group was significantly ($p < 0.03$) heavier than BDL group during the study.

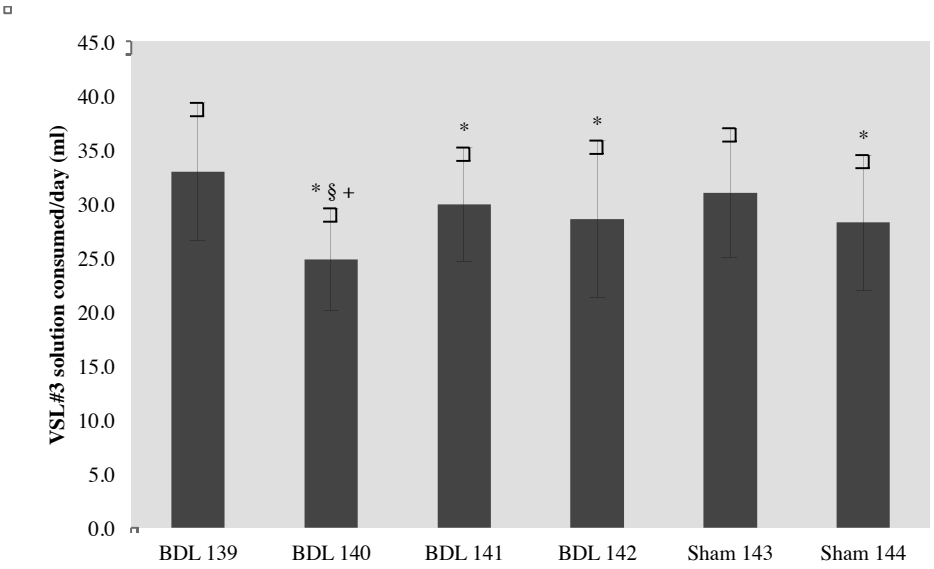

Figure 22 - Daily consumption of VSL#3® solution per rat. Bars represent de mean value ± standard deviation.

* Statistically significant lower value in comparison with BDL 139 ($\boldsymbol{p < 0.005}$)

§ Statistically significant lower value in comparison with BDL 141 ($\boldsymbol{p < 0.005}$)

+ Statistically significant lower value in comparison with BDL 142 ($\boldsymbol{p < 0.005}$)

Table 3 - Mean body weight of each VSL#3® treated rat over the entire study.

	BDL 139 [+]	BDL 140 [*§+]	BDL 141 [+]	BDL 142	Sham 143	Sham 144 [+]
Body Weight (g)[#]	259.8 ± 39.7	228.3 ± 30.4	268.4 ± 41.5	318.3 ± 63.4	307.4 ± 63.7	273.8 ± 47.0

[*] Statistically significant lower value in comparison with BDL 139 ($p < 0.005$)
[§] Statistically significant lower value in comparison with BDL 141 ($p < 0.0005$)
[+] Statistically significant lower value in comparison with BDL 142 ($p < 0.01$)
[#] Statistically significant differences when comparing BDL and sham-operated rats ($p < 0.03$)

It is, however, important to note that animals were not weighted every day to minimize their stress level, contrary to the VSL#3® intake measurements.

4.1.3. ^{1}H MRS Data

^{1}H MRS scans were performed just before surgery and two weeks after the beginning of treatment (scan 0), and at two, four, six and eight weeks after surgery (scans 2, 4, 6 and 8, respectively) in the hippocampus. Therefore, besides having the sham-operated group as control at matched time points, each rat was also his own control by comparison with scan 0. Eight weeks was the determined end point, as BDL rats do not usually survive much longer and it was necessary to perform histology on brain and liver tissues taken from animals a few minutes post-mortem.

^{1}H MRS data was acquired with a sufficiently high SNR (see Table 4 and Table 5) for the accurate detection of 21 metabolite resonances. The high quality data can also be observed on the spectra presented on Figure 23.

Table 4 - Mean signal-to-noise ratio (SNR) of each scan on VSL#3® treated BDL rats.

	Scan 0 (n=4)	Scan 2 (n=4)	Scan 4 (n=4)	Scan 6 (n=4)	Scan 8 (n=2)
SNR	25.0 ± 2.9	27.3 ± 2.6	27.5 ± 3.1	28.5 ± 5.7	26.5 ± 0.7

Table 5 - Mean signal-to-noise ratio (SNR) of each scan on sham-operated rats treated with VSL#3®.

	Scan 0	Scan 2	Scan 4	Scan 6	Scan 8
SNR (n=2)	34.0 ± 4.2	26.5 ± 0.7	26.0 ± 0.0	22.0 ± 4.2	19.0 ± 2.8

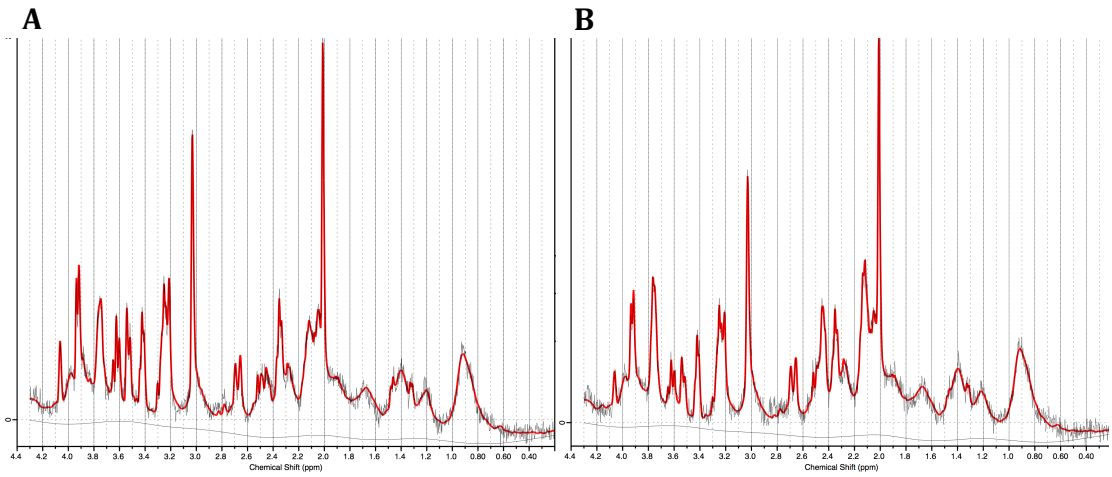

Figure 23 - Spectrum of metabolites of BDL 141 at **(A)** scan 0 and **(B)** scan 8. Spectra are of high resolution due to good quality shimming, perfect voxel localization (proven by the absence of lipids contamination at 0.9 ppm), good water suppression and baseline.

Figure 24 and Figure 25 represent the overall evolution of brain metabolism of, respectively, BDL and sham-operated groups treated with VSL#3®.

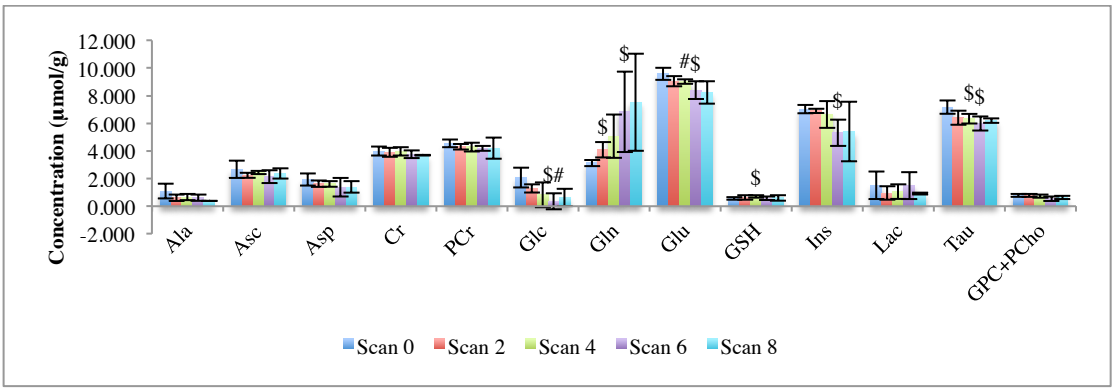

Figure 24 - Longitudinal evolution of brain metabolism of all BDL rats treated with VSL#3® (n=4, scan 0 – scan 6; n=2, scan 8). Bars represent de mean value ± standard deviation.

$ Statistically significant differences in comparison with scan 0 ($p < 0.05$)

Statistically significant differences when comparing BDL and sham-operated groups at matched time points ($p < 0.04$)

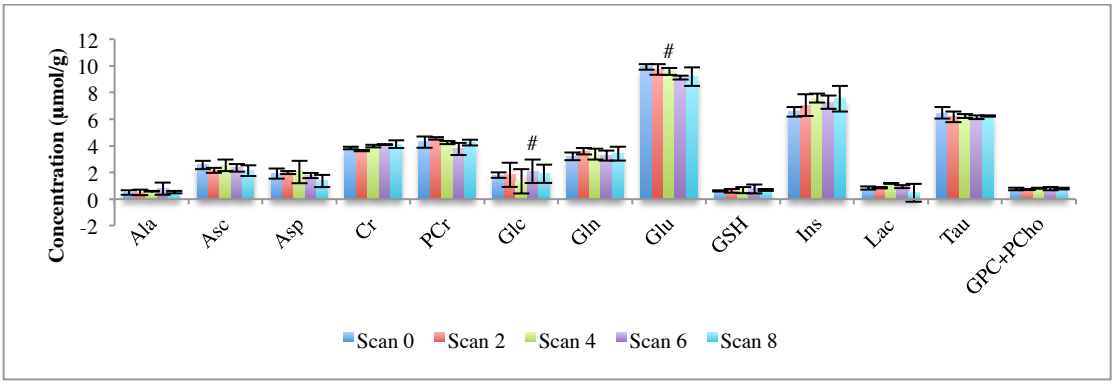

Figure 25 - Longitudinal evolution of brain metabolism of all sham-operated rats treated with VSL#3® (n=2). Bars represent de mean value ± standard deviation. # Statistically significant differences when comparing BDL and sham-operated groups at matched time points ($\boldsymbol{p < 0.04}$)

4.1.3.1. Osmoregulation

4.1.3.1.1. Gln

Table 6 shows the Gln concentrations of each rat over the entire study. For the BDL group, CRLBs (the quantification errors) ranged between 2 and 8% with a mean value of 4.5%. For the sham group, CRLBs ranged between 4 and 8%, with a mean value of 6.1%.

No statistically significant differences were observed by comparison between BDL and sham-operated groups at matched time points; however, BDL rats presented, in average, 108.5 and 120.7% higher Gln concentration levels at, respectively, scans 6 and 8. Furthermore, a longitudinal increase of Gln concentration was noticed in the BDL group, with a statistically significant average increase of 30.2 ($p < 0.02$), 118.1 ($p < 0.05$) and 140.5% ($p < 0.05$) at, respectively, scans 2, 6 and 8 in comparison with scan 0. Within BDL group, BDL 139 presented the lowest concentration levels of Gln. At scan 6, the Gln level of BDL 139 was, approximately, 2.9, 1.9 and 1.6-fold lower than the Gln levels of, respectively, BDL 140, 141 and 142. At scan 8, BDL 141

showed an approximately 2-fold higher Gln concentration level than BDL 139 did.

The mean standard deviations as a percentage for each week's average were 28.2 and 11.0% for, respectively, BDL and sham-operated groups.

Table 6 – Glutamine (Gln) concentrations obtained per rat over the entire study.

		BDL 139	**BDL 140**	**BDL 141**	**BDL 142**	**Sham 143**	**Sham 144**
Concentration (µmol/g)	**Scan 0**	2.80	3.20	3.20	3.31	3.42	3.00
	Scan 2	3.47	4.65	4.39	3.77	3.43	3.77
	Scan 4	3.50	7.23	5.01	4.54	3.07	3.65
	Scan 6	3.69	10.66	6.93	6.01	3.00	3.54
	Scan 8	5.04		10.01		3.04	3.77

4.1.3.1.2. Ins

Table 7 shows the Ins concentration levels of each rat over the entire study. For the BDL group, CRLBs ranged between 3 and 5% with a mean value of 3.4%. For the sham group, CRLBs ranged between 2 and 4%, with a mean value of 2.9%. Within BDL group, a longitudinal trend of decrease of Ins over time was noticed, reaching statistical significance at scan 6 ($p < 0.02$), with an average decrease of 24.1% in comparison with scan 0. Moreover, the decrease of Ins concentration was more accentuated in BDL rats expressing higher concentrations of Gln, and vice-versa.

Table 7 – *Myo*-Inositol (Ins) concentrations obtained per rat over the entire study.

		BDL 139	**BDL 140**	**BDL 141**	**BDL 142**	**Sham 143**	**Sham 144**
Concentration (µmol/g)	**Scan 0**	6.76	6.78	7.12	7.41	6.81	6.29
	Scan 2	6.99	6.91	7.05	6.68	7.64	6.47
	Scan 4	7.68	5.53	6.64	6.95	7.81	7.35
	Scan 6	6.26	3.98	5.56	5.49	7.62	6.92
	Scan 8	6.91		3.87		8.20	6.85

No statistically significant differences were observed by comparison between BDL and sham-operated groups at matched time points; however, BDL rats presented, in average, 26.8 and 28.4% lower Ins concentration levels at, respectively, scans 6 and 8.

The mean standard deviations as a percentage for each week's average were 15.9 and 8.2% for, respectively, BDL and sham-operated groups.

4.1.3.1.3. tCho (GPC + PCho)

Table 8 shows the tCho concentration levels of each rat over the entire study. For the BDL group, CRLBs ranged between 6 and 13% with a mean value of 8.9%. For the sham group, CRLBs ranged between 6 and 11%, with a mean value of 8.2%.

Table 8 – Total choline (tCho) concentrations obtained per rat over the entire study.

		BDL 139	BDL 140	BDL 141	BDL 142	Sham 143	Sham 144
Concentration (µmol/g)	**Scan 0**	0.82	0.86	0.78	0.64	0.69	0.82
	Scan 2	0.83	0.87	0.85	0.62	0.70	0.77
	Scan 4	0.90	0.73	0.68	0.63	0.79	0.85
	Scan 6	0.80	0.44	0.43	0.49	0.70	0.88
	Scan 8	0.73		0.54		0.75	0.83

Within BDL group, tCho concentration showed a trend of decrease of 30.2 and 18.2% at, respectively, scans 6 and 8, in comparison with scan 0. In the same way as the results obtained for Ins, a relation between tCho decrease and Gln increase was verified among BDL rats, since animals with higher Gln concentrations registered a more prominent decrease of tCho.

No statistically significant differences were observed by comparison between BDL and sham-operated groups at matched time points; however,

BDL rats presented, in average, 31.6 and 19.6% lower tCho concentration levels at, respectively, scan 6 and scan 8.

The mean standard deviations as a percentage for each week's average were 19.2 and 9.5% for, respectively, BDL and sham-operated rats.

4.1.3.1.4. Tau

No statistically significant differences were observed by comparison between BDL and sham-operated groups at matched time points. In fact, average Tau concentration values did not differ much between groups during the study. At scan 6 and 8, average Tau concentration levels of the BDL group were, respectively, 2.6 and 0.8% lower than in sham-operated group. A statistically significant decrease in Tau concentration levels was noticed in BDL group at scan 4 ($p < 0.04$) and scan 6 ($p < 0.02$) in comparison with scan 0, which corresponded, respectively, to 11.7 and 16.5% of decrease.

The mean standard deviations as a percentage for each week's average were 6.4 and 3.8% for, respectively, BDL and sham-operated rats. For the BDL group, CRLBs ranged between 3 and 4% with a mean value of 3.4%. For the sham group, CRLBs ranged between 3 and 4%, with a mean value of 3.7%.

4.1.3.1.5. Cr

When compared with sham-operated groups at matched time points BDL rats presented, in average, 8.4 and 10.3% lower Cr concentration values at, respectively, scan 6 and scan 8. However mainly due to small number of animals used in this pilot study, no statistically significant differences were observed by comparing with sham animals. In addition, a trend of decrease was noticed, with average decreases of 5.9 and 7.3% at, respectively, scan 6 and 8 in comparison with scan 0.

The mean standard deviations as a percentage for each week's average were 6.6 and 2.9% for, respectively, BDL and sham-operated groups. For the BDL group, CRLBs ranged between 4 and 7% with a mean value of 5.2%. For the sham group, CRLBs ranged between 5 and 7%, with a mean value of 5.6%.

The total osmolyte concentrations comprising Gln, Ins, tCho, Tau and Cr were monitored over the duration of the experiment and it was found that their sum remained approximately constant, with a standard deviation of 2.5 and 2.4% for BDL and sham-operated groups, respectively.

4.1.3.2. Neurotransmission

4.1.3.2.1. Asp

No statistically significant differences were observed by comparison between BDL and sham-operated groups at matched time points. At scan 6, BDL group had a 28.2% lower Asp average concentration value in comparison with sham-operated group; however, at scan 8, it was 1.4% higher. In addition, no statistical significance was achieved when comparing the longitudinal evolution of Asp in the BDL group; however, a trend of decrease was noticed, with average decreases of 29.2 and 28.5% at, respectively, scan 6 and 8 in comparison with scan 0. However, these results need to be handled with caution, since CRLBs, in the BDL group, ranged between 14.0% and 87.0%, with a mean value of 24.3%, and in the sham-operated group, they ranged between 11.0 and 45.0%, having a mean value of 20.9%.

The mean standard deviations as a percentage for each week's average were 25.9 and 22.9% for, respectively, BDL and sham-operated rats.

4.1.3.2.2. Glu

Statistically significant differences ($p < 0.03$) were observed by comparison between BDL and sham-operated groups at scan 4, where the BDL group presented, in average, 6% lower Glu concentration values. In addition, a longitudinal decrease of Glu concentration was noticed in the BDL group, with a statistically significant ($p < 0.03$) average decrease of 12.3% at scan 6 in comparison with scan 0.

The mean standard deviations as a percentage for each week's average were 5.7 and 3.7% for, respectively, BDL and sham-operated groups. For the BDL group, CRLBs ranged between 2.0 and 4.0% with a mean value of 3.0%. For the sham group, CRLBs ranged between 2.0 and 4.0%, with a mean value of 2.8%.

4.1.3.3. Antioxidant Metabolism

4.1.3.3.1. Asc

No statistically significant differences were observed by comparison between BDL and sham-operated groups at matched time points, neither when comparing each time point with scan 0. In fact, during the progression of the disease, fluctuations on the levels of Asc were observed. However, concentration decreases were of higher magnitude and, therefore, an overall trend of decrease remained in the BDL group; average decreases of 19.4 and 11.8% were obtained at, respectively, scan 6 and 8 in comparison with scan 0. Furthermore and in comparison with sham-operated group, BDL group presented an average Asc concentration 8.1% lower and 10.0% higher at, respectively, scans 6 and 8.

The mean standard deviations as a percentage for each week's average were 15.0% and 13.8% for, respectively, BDL and sham-operated rats. For the

BDL group, CRLBs ranged between 8.0 and 19.0% with a mean value of 11.0%. For the sham group, CRLBs ranged between 6.0 and 18.0%, with a mean value of 11.3%.

4.1.3.3.2. GSH

A trend of increase in GSH concentrations was observed, reaching statistical significance at scan 4 in comparison with scan 0 ($p < 0.05$), with an average difference of 28.8%. No statistically significant differences were observed by comparison between BDL and sham-operated groups at matched time points; however and until scan 4, GSH average concentration was higher in BDL group, reaching 6.2% at scan 4. A drop on GSH average concentration in BDL group occurred between scan 4 and 6, although an overall trend of increase prevailed, with an average increase of 4.7 and 10.1% in comparison with scan 0 at, respectively, scans 6 and 8. However and in comparison with sham-operated group, BDL group presented, at scans 6 and 8, 4.7 and 10.1% lower values that were below statistical significance.

These results need to be handled with caution, since CRLBs, in the BDL group, ranged between 15.0% and 32.0%, with a mean value of 21.6%, and in the sham-operated rats, they ranged between 13.0 and 27.0%, having a mean value of 20.2%. The mean standard deviations as a percentage for each week's average were 22.8% and 23.7% for, respectively, BDL and sham-operated rats.

4.1.3.4. Energy Metabolism

4.1.3.4.1. PCr

No statistically significant differences were observed by comparison between BDL and sham-operated groups at matched time points; however,

BDL rats presented, in average, 11.0% higher and 1.4% lower PCr concentration values at, respectively, scan 6 and scan 8. In addition, no statistical significance was achieved when comparing the longitudinal evolution of Cr in the BDL group; however, a trend of decrease was noticed, with average decreases of 8.0 and 7.8% at, respectively, scan 6 and 8 in comparison with scan 0. Taking into account that the average PCr concentration remained, approximately constant from scan 6 until scan 8, the dissimilar average differences observed between BDL and sham-operated groups at scans 6 and 8 might, therefore, be due to naturally occurring fluctuations.

The mean standard deviations as a percentage for each week's average were 8.2% and 6.5% for, respectively, BDL and sham-operated groups. For the BDL group, CRLBs ranged between 4.0 and 6.0% with a mean value of 4.8%. For the sham group, CRLBs ranged between 4.0 and 8.0%, with a mean value of 5.3%.

4.1.3.4.2. Ala

No statistically significant differences were observed by comparison between BDL and sham-operated groups at matched time points; however, BDL rats presented, in average, 21.2 and 27.3% lower Ala concentration values at, respectively, scan 6 and scan 8. In addition, no statistical significance was achieved when comparing the longitudinal evolution of Ala in the BDL group; however, a trend of decrease was noticed, with average decreases of 44.0 and 64.8% at, respectively, scan 6 and 8 in comparison with scan 0.

However, these results need to be handled with caution, since CRLBs, in the BDL group, ranged between 9.0% and 43.0%, with a mean value of 23.9%, and in the sham-operated rats, they ranged between 15.0 and 37.0%, having a mean value of 26.1%.

The mean standard deviations as a percentage for each week's average were 31.9% and 30.8% for, respectively, BDL and sham-operated rats.

4.1.3.4.3. Lac

No statistical significance was achieved when comparing the longitudinal evolution of Lac in the BDL group; however, a trend of decrease was noticed, with average decreases of 1.6 and 39.4% at, respectively, scan 6 and 8 in comparison with scan 0. In fact, a sharp decrease of the average Lac concentration occurred between scans 0 and 2; from scan 2 and until scan 6, a progressive increase was observed, after which a sharp drop occurred between scan 6 and 8. In addition, no statistically significant differences were observed by comparison between BDL and sham-operated groups at matched time points; however, BDL rats presented, in average, 56.9 and 95.0% higher Lac concentration values at, respectively, scan 6 and scan 8. The mean standard deviations as a percentage for each week's average were 48.3% and 35.4% for, respectively, BDL and sham-operated rats.

However, these results need to be handled with caution, since CRLBs (excluding those with null measured concentration), in the BDL group, ranged between 5.0% and 35.0%, with a mean value of 14.6%; in the sham-operated rats, they ranged between 12.0 and 19.0%, having a mean value of 14.3%.

4.1.3.4.4. Glucose (Glc)

As expected according to the longitudinal biochemical measurements performed in the blood, a longitudinal trend of decrease of brain Glc concentration was observed, reaching statistical significance at scan 6 ($p < 0.01$), with an average decrease of 82.9% in comparison with scan 0. Furthermore and comparing with the sham-operated group, BDL group

significantly ($p < 0.04$) showed, in average, a 83.1% lower Glc concentration at scan 6. These results, however, were, approximately, 1.5-fold higher than the body blood Glc levels measured by blood sampling. Furthermore, these results are considered imprecise, since CRLBs (excluding those with null measured concentration), in the BDL group, ranged between 14.0% and 434.0%, with a mean value of 82.8%, and in the sham-operated rats, they ranged between 14.0 and 55.0%, having a mean value of 25.1%. The mean standard deviations as a percentage for each week's average were 85.9% and 41.6% for, respectively, BDL and sham-operated groups.

4.2. Treatment with Cr

4.2.1. Animal Characterization

Seven male Wistar rats, five of which were BDL and two were sham-operated, were treated with Cr, starting immediately after surgery.

Table 9 - Characteristics of BDL and sham-operated rats treated with Cr, at eight weeks after surgery.

	Body Weight (g) [#]	**Glc (mg/dl)** [#]	**Bilirubin (mg/dl)**	**Liver Weight (g)** [#]
BDL (n=5)	293.4 ± 39.9	72.2 ± 20.1	6.3 ± 0.8	28.0 ± 6.0
Sham (n=2)	382.5 ± 7.8	188.0 ± 7.1	< 0.5	10.0 ± 0.0

[#] Statistically significant differences when comparing BDL and sham-operated rats ($p < 0.04$)

Table 9 shows the animal characteristics at eight weeks after bile duct ligation. Bilirubin levels were above the threshold associated with liver disease after bile duct ligation (0.5 mg/dl), thus confirming that the bile duct was properly ligated and that no rat recovered afterwards. With increasing time after surgery, BDL rats showed a longitudinal and statistically

significant decrease of body weight ($p < 0.04$) and Glc levels ($p < 0.001$), and an increase of liver weight ($p < 0.01$) when comparing with sham-operated rats at eight weeks after bile duct ligation. Figure 26 shows images of two livers, taken immediately post-mortem: one from a BDL rats and the other from a sham-operated rat.

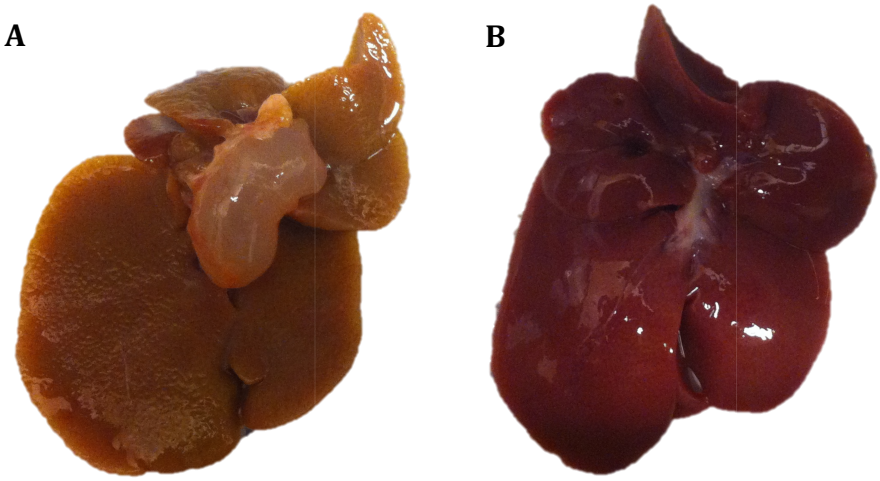

Figure 26 - Images of the liver of **(A)** BDL 154 and **(B)** sham 156. It is notorious the bile pouch formed by the bile duct ligation in the first photo, and also the difference of color and shape between the two livers, indicative of a cirrhotic liver in the first case. Images are not on the same scale.

4.2.2. Consumption of Cr

A diet enriched with a dose of 20 grams of Cr per kilogram of diet was given to animals. The dose was chosen taking into account that a rat consumes between 15 and 25 grams or 5% of its body weight per day. The diet intake was measured once per week per cage. BDL rats were divided in two cages – one with three rats (BDL 150 – 152) and the other one with two rats (BDL 154 and 155) – and sham-operated rats were housed together in one cage.

Table 10 - Mean daily consumption of Cr enriched diet per rat, depending on its cage.

	Cage 1	Cage 2 ¥	Cage 3
Diet consumed/rat/day (g)	22.4 ± 3.9	18.0 ± 4.3	21.4 ± 1.2

¥ Statistically significant lower value in comparison with cage 1 ($p < 0.05$)

Table 11 - Mean body weight of each Cr treated rat over the entire study.

	Cage 1			Cage 2 ¤		Cage 3	
	BDL 150	**BDL 151**	**BDL 152**	**BDL 153**	**BDL 154**	**Sham 155**	**Sham 156**
Body Weight (g) #	268.4 ± 46.0	268.3 ± 46.1	292.3 ± 51.7	242.8 ± 37.7	246.9 ± 30.9	298.4 ± 63.0	281.2 ± 60.4

¤ Statistically significant lower values in comparison with other cages ($p < 0.004$)

Statistically significant differences when comparing BDL and sham-operated rats ($p < 0.006$)

Table 10 represents the daily diet consumed per rat depending on its cage and Table 11 shows the body weight of each rat during the entire study. Thereby, one can deduce that, based on their body weight, every rat consumed more than the expected; however, diet intake measurements were performed per cage and not per animal. A statistically significant ($p < 0.05$) lower consumption was verified in cage 2, in comparison with cage 1. Correspondingly, the average weight of animals in cage 2 was significantly ($p < 0.0004$) lower in comparison with cage 1 over the study. Furthermore, sham-operated group was significantly ($p < 0.006$) heavier than BDL group during the study.

4.2.3. ^{1}H MRS Data

^{1}H MRS scans were performed at four, six and eight weeks after surgery (scans 4, 6 and 8, respectively). Time points four and six in particular were chosen as these had been noticed as significant time points for sharp

changes in metabolite concentrations in previous studies. Eight weeks was the determined end point, as BDL rats do not usually survive much longer and it was necessary to perform histology on brain and liver tissues taken from animals a few minutes post-mortem.

Table 12 - Mean signal-to-noise ratio (SNR) of each scan on Cr treated animals.

	BDL (n=5)			Sham (n=2)		
	Scan 4	**Scan 6**	**Scan 8**	**Scan 4**	**Scan 6**	**Scan 8**
SNR	24.6 ± 1.8	24.8 ± 3.3	22.8 ± 2.6	20.5 ± 0.7	23.5 ± 3.5	22.0 ± 1.4

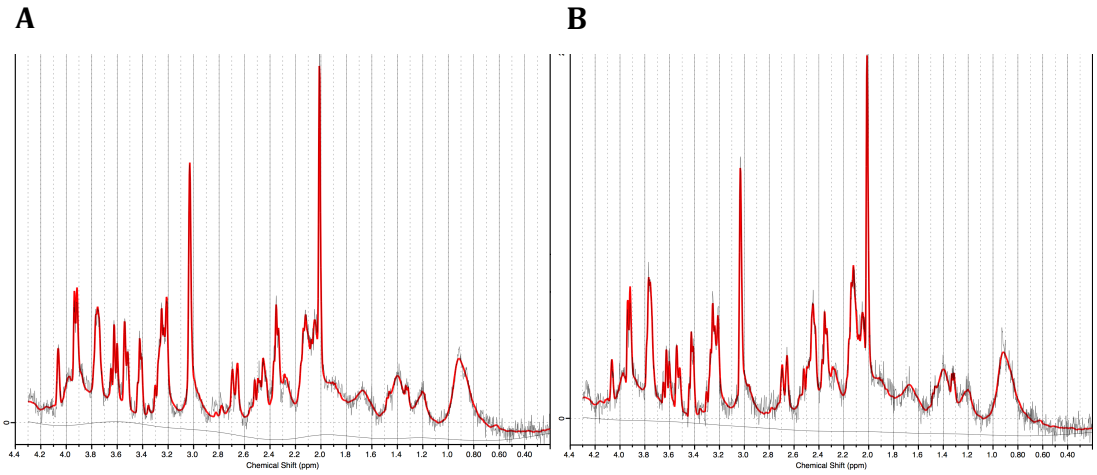

Figure 27 - Spectrum of metabolites of BDL 151 at **(A)** scan 4 and **(B)** scan 8. Spectra are of high resolution due to good quality shimming, perfect voxel localization (proven by the absence of lipids contamination at 0.9 ppm), good water suppression and baseline.

^{1}H MRS data was acquired with a sufficiently high SNR (see Table 12) for the accurate detection of 21 metabolite resonances. The high quality data can also be observed on the spectra presented on Figure 27.

Figure 28 and Figure 29 represent the overall evolution of brain metabolism of, respectively, BDL and sham-operated groups treated with Cr.

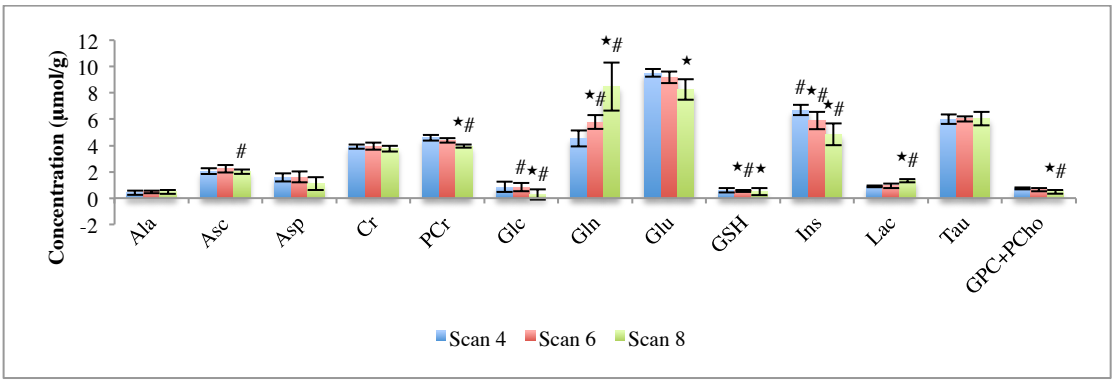

Figure 28 - Longitudinal evolution of brain metabolism of all BDL rats treated with Cr (n=5). Bars represent de mean value ± standard deviation. ⋆ Statistically significant differences in comparison with scan 4 ($\boldsymbol{p < 0.05}$) # Statistically significant differences when comparing BDL and sham-operated groups at matched time points ($\boldsymbol{p < 0.03}$)

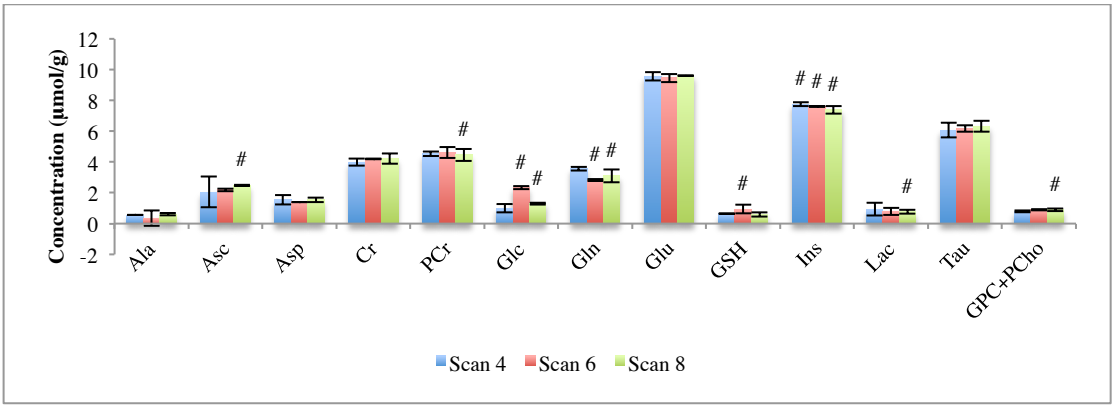

Figure 29 - Longitudinal evolution of brain metabolism of all sham-operated rats treated with Cr (n=2). Bars represent de mean value ± standard deviation. # Statistically significant differences when comparing BDL and sham-operated groups at matched time points ($\boldsymbol{p < 0.03}$)

4.2.3.1. Osmolytes

4.2.3.1.1.Gln

A statistically significant increase was longitudinally noticed in BDL group, reaching, in average, 27.3% ($p < 0.009$) at scan 6 and 86.6% ($p < 0.002$) at scan 8 in comparison with scan 4. Furthermore, statistically

significant differences were observed by comparison between BDL and sham-operated groups at scan 6 ($p < 0.0007$), where the BDL group presented, in average, 104.3% higher Gln concentration values; and at scan 8 ($p < 0.02$), with an average concentration 173.7% higher.

The mean standard deviations as a percentage for each week's average were 14.7% and 6.6% for, respectively, BDL and sham-operated groups. For the BDL group, CRLBs ranged between 2.0 and 5.0% with a mean value of 4.0%. For the sham group, CRLBs ranged between 6.0 and 9.0%, with a mean value of 8.0%.

4.2.3.1.2. Ins

A statistically significant decrease was longitudinally noticed in BDL group, reaching, in average, 12.1% ($p < 0.05$) at scan 6 and 27.7% ($p < 0.002$) at scan 8 in comparison with scan 4. Furthermore, statistically significant differences were observed by comparison with sham-operated group at scan 4 ($p < 0.02$), scan 6 ($p < 0.02$) and at scan 8 ($p < 0.01$), with, respectively, average Ins concentration values 13.7, 22.8 and 34.6% lower.

The mean standard deviations as a percentage for each week's average were 11.3% and 1.7% for, respectively, BDL and sham-operated groups. For the BDL group, CRLBs ranged between 3.0 and 5.0% with a mean value of 3.7%. For the sham group, all CRLBs had a value of 3.0%.

4.2.3.1.3. tCho (GPC + PCho)

An overall decrease in tCho concentration levels was noticed in BDL group, reaching statistical significance at scan 8 ($p < 0.006$), with an average 35.2% decrease in comparison with scan 4. Still at scan 8, statistically significant differences were observed by comparison with sham-operated group ($p < 0.01$), with average tCho concentration 48.0% lower.

The mean standard deviations as a percentage for each week's average were 19.7% and 7.4% for, respectively, BDL and sham-operated groups. For the BDL group, CRLBs ranged between 7.0 and 30.0% with a mean value of 11.1%. For the sham group, CRLBs ranged between 7.0 and 9.0% with an average value of 8.0%.

4.2.3.1.4. Tau

No statistical significance was achieved when comparing the longitudinal evolution of Tau in the BDL group; in fact, only an increase of low magnitude was registered, with an average value of 0.5% at scan 8 in comparison with scan 4. Likewise, no statistically significant differences were observed between BDL and sham-operated groups; at scan 8, BDL group presented, in average, a 4.6% lower value, which seems to be related with naturally occurring fluctuations.

The mean standard deviations as a percentage for each week's average were 5.9% and 5.6% for, respectively, BDL and sham-operated groups. For the BDL group, CRLBs ranged between 3.0 and 5.0% with a mean value of 3.7%. For the sham group, CRLBs ranged between 3.0 and 5.0% with an average value of 4.0%.

4.2.3.1.5. Cr

No statistical significance was achieved when comparing the longitudinal evolution of Cr in the BDL group, neither in comparison with sham-operated group at matched time points. It was registered an average 1% increase and 3.6% decrease at, respectively, scan 6 and 8 in comparison with scan 4. In addition, the BDL group showed lower concentration levels of Cr in comparison with the sham-operated group, which were in the order of 5.9 and 10.8% at, respectively, scan 6 and 8. A coincident statistically

significant 38.3% ($p < 0.02$) diminution on the consumption of Cr enriched diet in the cage 2 occurred between the sixth and eighth weeks after surgery. Furthermore, between the seventh and eighth weeks, cage 1 registered an approximate 31.1% reduced consumption in comparison with the previous week.

The mean standard deviations as a percentage for each week's average were 5.6 and 4.8% for, respectively, BDL and sham-operated groups. For the BDL group, CRLBs ranged between 5.0 and 7.0% with a mean value of 5.7%. For the sham group, CRLBs ranged between 4.0 and 6.0% with an average value of 5.3%.

The total osmolyte concentration comprising Gln, Ins, Tau, Cr and tCho were monitored over the duration of the experiment and it was found that their sum remained roughly constant, with standard deviations of 4.0% for the BDL group and 1.1% for the sham-operated one.

4.2.3.2. Neurotransmission

4.2.3.2.1. Asp

No statistical significance was achieved when comparing the longitudinal evolution of Asp in the BDL group, neither in comparison with sham-operated group at matched time points. However, a trend of decrease of Asp concentration was noticed in the BDL group, with a drop between scans 6 and 8. At scan 8, the BDL group presented a 31.8% average decrease in comparison with scan 4, and a 30.2% average lower value comparing with sham-operated group. However, these results need to be handled with caution, since CRLBs, in the BDL group, ranged between 17.0% and 53.0%, with a mean value of 27.8%, and in the sham-operated group, they ranged between 23.0 and 29.0%, having a mean value of 25.8%. The mean standard

deviations as a percentage for each week's average were 30.5% and 10.0% for, respectively, BDL and sham-operated groups.

4.2.3.2.2. Glu

In BDL group, a statistically significant ($p < 0.02$) longitudinal decrease of Glu concentrations, when comparing scans 4 and 8, was noticed. At scan 8, Glu concentrations were, in average, 13% diminished in comparison in scan 4. No statistically significant differences were observed between BDL and sham-operated groups; however, at scan 8, BDL group presented, in average, a 14.0% lower value.

The mean standard deviations as a percentage for each week's average were 5.8 and 2.0% for, respectively, BDL and sham-operated groups. For the BDL group, CRLBs ranged between 2.0 and 4.0% with a mean value of 3.1%. For the sham group, CRLBs ranged between 3.0 and 4.0% with an average value of 3.2%.

4.2.3.3. Antioxidant Metabolism

4.2.3.3.1. Asc

No statistical significance was achieved when comparing the longitudinal evolution of Asc in the BDL group; in fact, only a decrease of low magnitude was registered, with an average value of 2.4% at scan 8 in comparison with scan 4. On the other hand, statistically significant ($p < 0.02$) differences were obtained between BDL and sham-operated groups at scan 8, with a 19.5% lower average value in the BDL group.

The mean standard deviations as a percentage for each week's average were 10.7 and 18.2% for, respectively, BDL and sham-operated groups. For the BDL group, CRLBs ranged between 10.0 and 16.0% with a mean value of

12.9%. For the sham group, CRLBs ranged between 10.0 and 24.0% with an average value of 14.2%.

4.2.3.3.2. GSH

No statistical significance was achieved when comparing the longitudinal evolution of GSH in the BDL group; however, a trend of decrease was noticed, reaching, in average, 19.4% at scan 8, in comparison with scan 4. On the other hand, statistically significant ($p < 0.03$) differences were obtained between BDL and sham-operated groups at scan 6, with a 41.6% lower average value in the BDL group. These results need, however, to be handled with caution, since CRLBs, in the BDL group, ranged between 16.0% and 58.0%, with a mean value of 28.1%, and in the sham-operated group, they ranged between 14.0 and 32.0%, having a mean value of 22.0%. The mean standard deviations as a percentage for each week's average were 33.9% and 17.5% for, respectively, BDL and sham-operated groups.

4.2.3.4. Energy Metabolism

4.2.3.4.1. PCr

Overall decreases in PCr concentration levels were noticed in BDL group, reaching statistical significance at scan 8 ($p < 0.04$), with an average 13.6% decrease in comparison with scan 4. Still at scan 8, statistically significant differences were observed by comparison with sham-operated group ($p < 0.0005$), with average tCho concentration 11.4% lower.

The mean standard deviations as a percentage for each week's average were 3.9% and 6.7% for, respectively, BDL and sham-operated groups. For the BDL group, CRLBs ranged between 4.0 and 7.0% with a mean value of 5.2%.

For the sham group, CRLBs ranged between 4.0 and 6.0% with an average value of 5.0%.

4.2.3.4.2. Ala

No statistical significance was achieved when comparing the longitudinal evolution of Ala in the BDL group; however, a trend of increase was noticed, reaching, in average, 17.0% at scan 8, in comparison with scan 4. In average, this increase was, however, 22.9% lower comparing with the sham-operated group at scan 8. These results are considered, however, imprecise, since CRLBs, in the BDL group, ranged between 19.0% and 101.0%, with a mean value of 36.5%, and in the sham-operated group (excluding those with null measured concentration), they ranged between 21.0 and 31.0%, having a mean value of 26.2%. Furthermore, the mean standard deviations as a percentage for each week's average were 31.1% and 51.6% for, respectively, BDL and sham-operated groups.

4.2.3.4.3. Lac

Overall increases in Lac concentration levels were noticed in BDL group, reaching statistical significance at scan 8 ($p < 0.0004$), with an average 46.6% increase in comparison with scan 4. Still at scan 8, statistically significant differences were observed by comparison with sham-operated group ($p < 0.005$), with average Lac concentration 74.2% higher. These results need, however, to be handled with caution, since CRLBs, in the BDL group, ranged between 9.0% and 23.0%, with a mean value of 14.5%, and in the sham-operated group, they ranged between 12.0 and 27.0%, having a mean value of 20.8%. The mean standard deviations as a percentage for each week's average were 12.6% and 29.8% for, respectively, BDL and sham-operated groups.

4.2.3.4.4. Glc

As expected according to the longitudinal biochemical measurements performed in blood, longitudinal decreases in brain Glc concentration levels were noticed in BDL group, reaching statistical significance at scan 8 ($p < 0.05$), with an average 68.8% decrease in comparison with scan 4. Still at scan 8, statistically significant differences were observed by comparison with sham-operated group ($p < 0.02$), with average Glc concentration 79.8% lower. In addition, a statistically significant ($p < 0.002$) 64.2% lower average Glc concentration was obtained at scan 6, in comparison with the sham-operated group. These results are, however, imprecise, since CRLBs (excluding those with null measured concentration), in the BDL group, ranged between 29.0% and 160.0%, with a mean value of 59.9%, and in the sham-operated group, they ranged between 17.0 and 50.0%, having a mean value of 31.0%. In addition, these results were approximately, 1.5-fold higher than the body blood Glc levels measured by blood sampling. Furthermore, the mean standard deviations as a percentage for each week's average were 76.7% and 11.9% for, respectively, BDL and sham-operated groups.

4.3. Behavioral Tests

Open field-Novel object tests were performed at six and eight weeks after surgery, one day before the respective scan, in both groups of treatment.

4.3.1. Open Field Task

The results for the open field task are presented in terms of distance moved (Figure 30), time spent under movement (Figure 31) and percentage of

time spent in the inner part of the arena (Figure 32), and were compared between non-treated, VSL#3® and Cr treated BDL and sham-operated groups of animals.

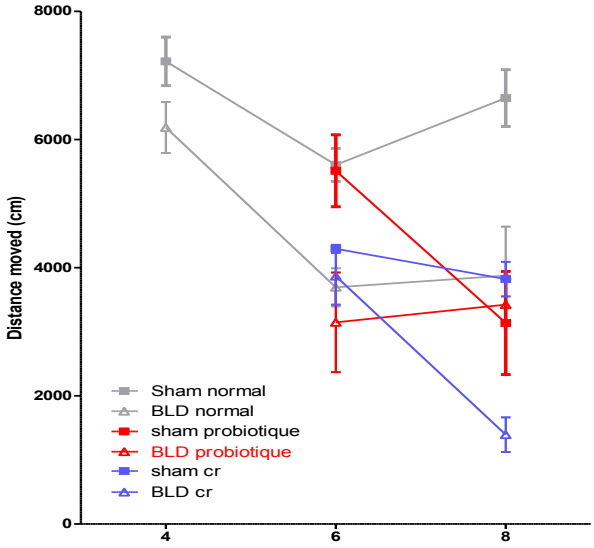

Figure 30 - Distance moved during the open field task of the non-treated sham (n=8), non-treated BDL (n=19), VSL#3®-treated sham (n=2), VSL#3®-treated BDL (n=4 at sixth weeks after surgery; n=2 at eighth weeks after surgery), Cr-treated sham (n=2) and Cr-treated BDL (n=5) groups of animals, at fourth, sixth and eighth weeks after surgery. normal: without treatment; probiotique: treated with VSL#3®.

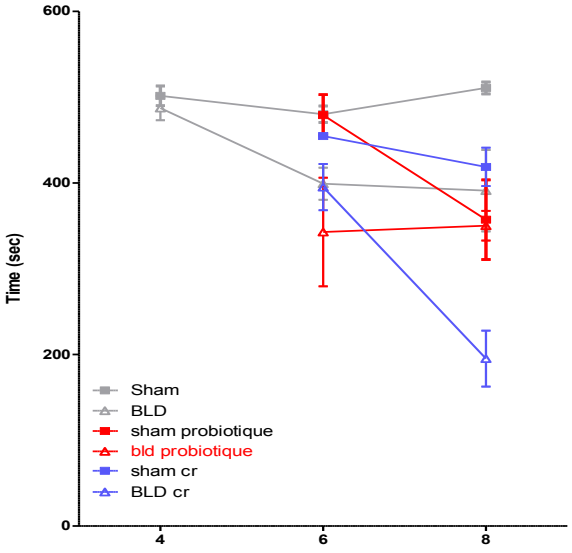

Figure 31 - Time spent under movement during the open field task of the non-treated sham (n=8), non-treated BDL (n=19), VSL#3®-treated sham (n=2), VSL#3®-treated BDL (n=4 at sixth weeks after surgery; n=2 at eighth weeks after surgery), Cr-treated sham (n=2) and Cr-treated BDL (n=5) groups of animals, at four, six and eight weeks after surgery. normal: without treatment; probiotique: treated with VSL#3®.

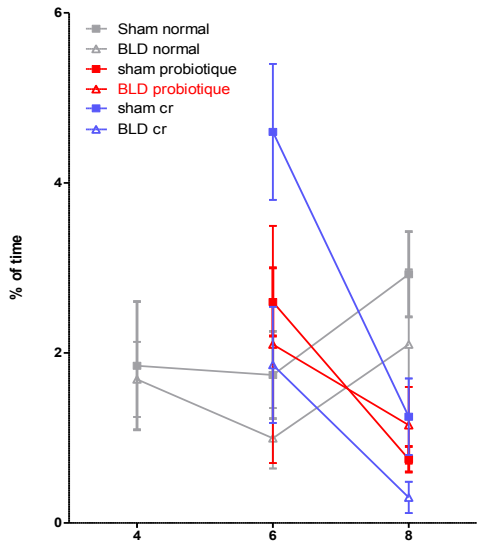

Figure 32 - Percentage of time spent in the inner part of the arena during the open field task of the non-treated sham (n=8), non-treated BDL (n=19), VSL#3®-treated sham (n=2), VSL#3®-treated BDL (n=4 at sixth weeks after surgery; n=2 at eighth weeks after surgery), Cr-treated sham (n=2) and Cr-treated BDL (n=5) groups of animals, at four, six and eight weeks after surgery. normal: without treatment; probiotique: treated with VSL#3®.

No statistical significant differences were found between groups, mainly due to the small sample size in both treated groups, which contributed to a high standard deviation. However, one can notice a trend to a lower distance moved, time spent under movement and percentage of time spent in the center of arena in BDL groups, in comparison with its correspondent sham-operated groups. This was significantly confirmed, however, with previous results from CIBM performed in a bigger sample of non-treated BDL and sham-operated animals.

Figure 33 shows previous results on distance moved during the open field task at four, six and eight weeks after surgery. The BDL group presented a statistically significant lower distance moved in comparison with sham-operated group, at both six ($p < 0.05$) and eight ($p < 0.01$) weeks after surgery.

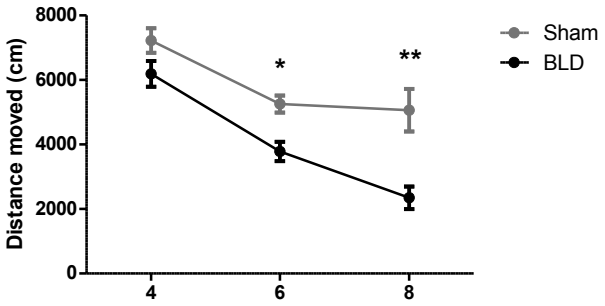

Figure 33 - Distance moved during the open field task of the non-treated sham (n=8) and non-treated BDL (n=19) groups, at four, six and eight weeks after surgery.
* Statistically significant differences between non-treated sham-operated and BDL groups at matched time points ($\boldsymbol{p < 0.05}$)
** Statistically significant differences between non-treated sham-operated and BDL groups at matched time points ($\boldsymbol{p < 0.01}$)

Figure 34 presents previous results on time spent under movement and immobile during the open field task at four, six and eight weeks after surgery. The BDL group presented a statistically significant less time spent in movement and a correspondingly higher immobile time, in comparison with sham-operated group, at both six ($p < 0.05$) and eight ($p < 0.001$) weeks after surgery.

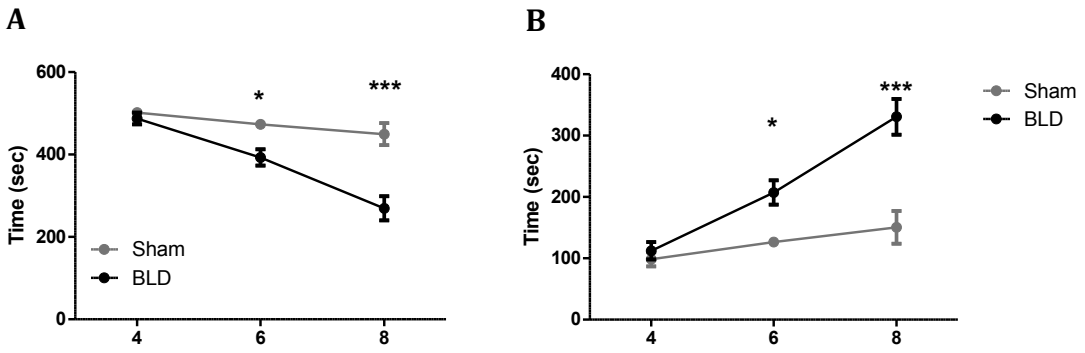

Figure 34 - Time spent **(A)** under movement and **(B)** immobile during the open field task of the non-treated sham (n=8) and non-treated BDL (n=19) groups, at four, six and eight weeks after surgery.
* Statistically significant differences between non-treated sham-operated and BDL groups at matched time points ($\boldsymbol{p < 0.05}$)
*** Statistically significant differences between non-treated sham-operated and BDL groups at matched time points ($\boldsymbol{p < 0.001}$)

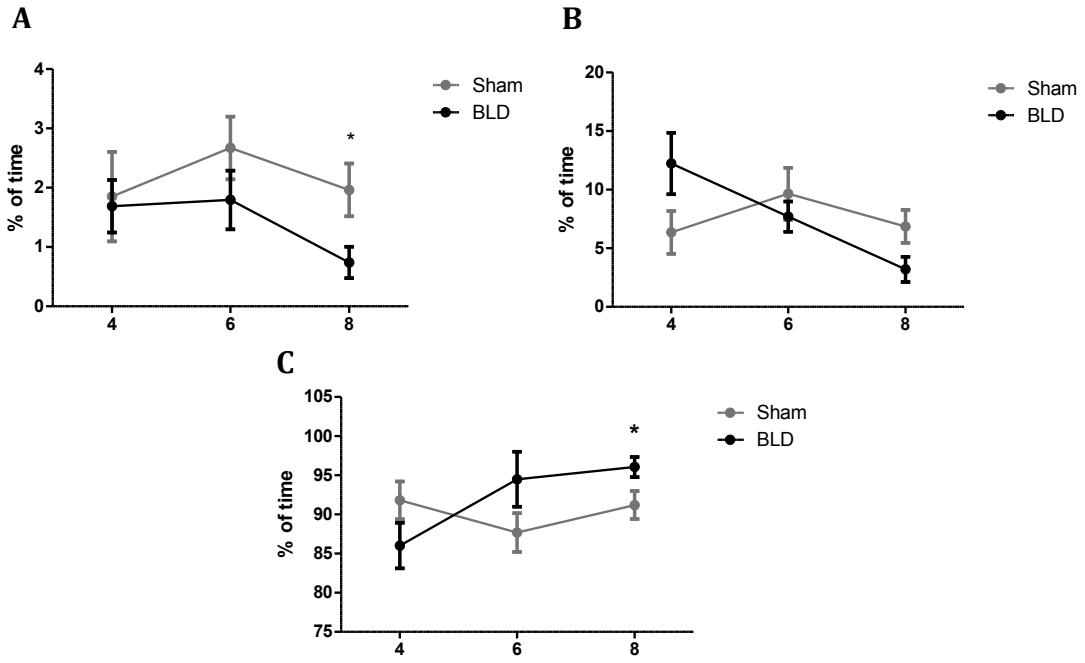

Figure 35 - Percentage of time spent in the **(A)** inner, **(B)** intermediate and **(C)** outer parts of the arena during the open field task of the non-treated sham (n=8) and non-treated BDL (n=19) groups, at four, six and eight weeks after surgery. * Statistically significant differences between non-treated sham-operated and BDL groups at matched time points ($p < 0.05$)

Figure 35 shows previous results on percentage of time spent in the inner, intermediate and outer parts of the arena during the open field task at four, six and eight weeks after surgery. The BDL group presented a statistically significant lower time spent in the inner and higher time spent in the outer parts of the arena, in comparison with sham-operated group at eight ($p < 0.05$) weeks after surgery.

4.3.2. Novel Object Task

The previously obtained results with non-treated animals and under novel object task, in terms of distance moved (Figure 36) and time spent under movement and immobile (Figure 37) were, in general, similar to those related to the open field task. Results differed, however, in the percentage of

time spent in each region of the arena (Figure 38). Statistically significant differences between non-treated sham and BDL groups were observed six weeks after surgery, with the BDL spending less time in the inner and intermediate areas, and more time in the outer part of the arena. No significant differences were observed at eight weeks after surgery due to the learning effect; animals recognize the introduced object from previously performed behavioral tests and, consequently, spend less time exploring it, near to the center of the arena.

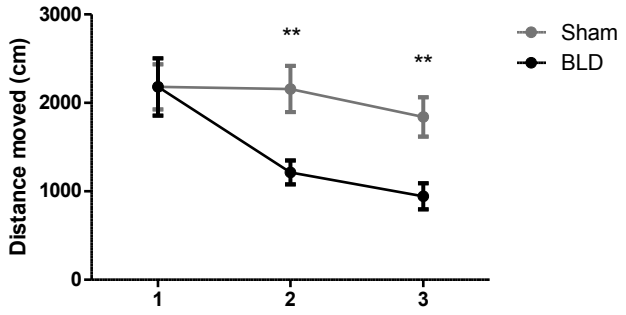

Figure 36 - Distance moved during the novel object task of the non-treated sham (n=8) and non-treated BDL (n=19) groups, at four (1), six (2) and eight (3) weeks after surgery.
** Statistically significant differences between non-treated sham-operated and BDL groups at matched time points ($\boldsymbol{p < 0.01}$)

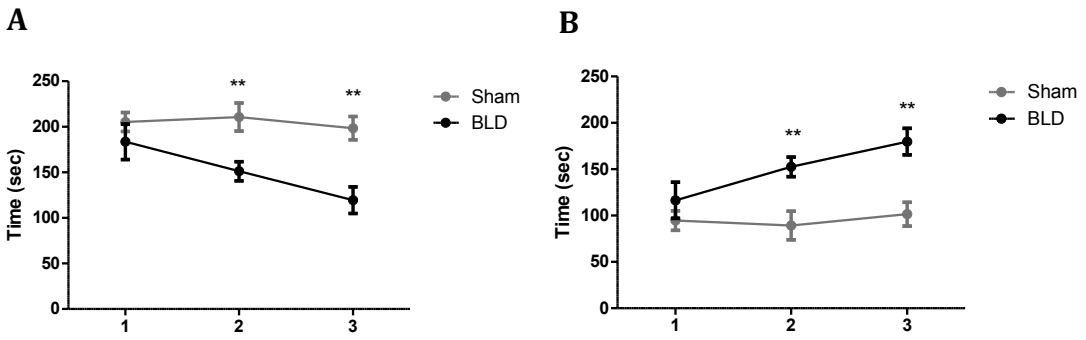

Figure 37 - Time spent **(A)** under movement and **(B)** immobile during the novel object task of the non-treated sham (n=8) and non-treated BDL (n=19) groups, at four (1), six (2) and eight (3) weeks after surgery.
** Statistically significant differences between non-treated sham-operated and BDL groups at matched time points ($\boldsymbol{p < 0.01}$)

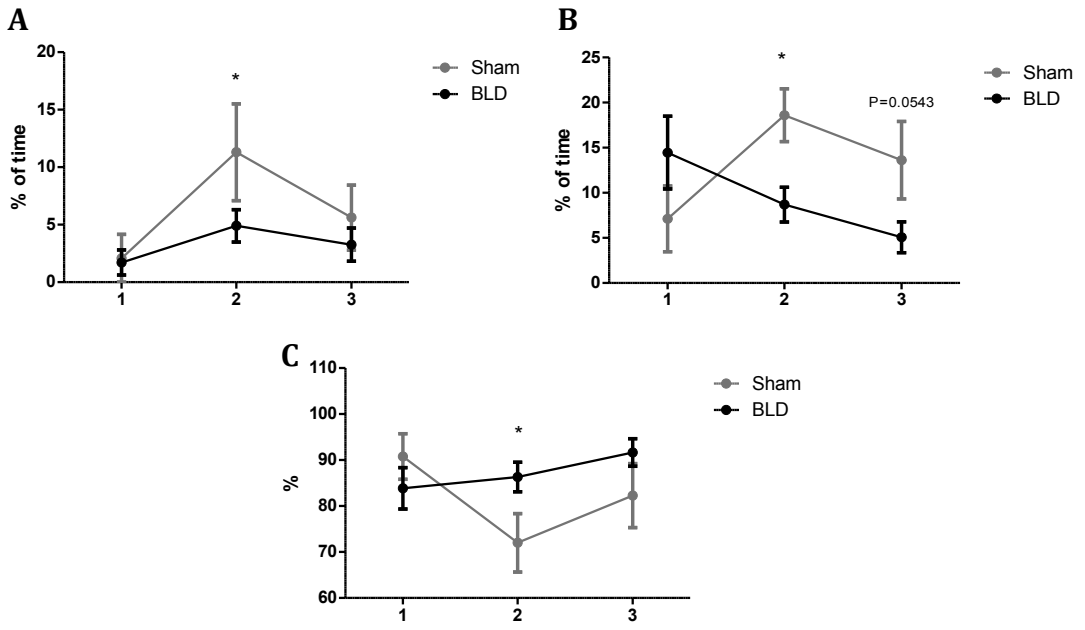

Figure 38 - Percentage of time spent in the **(A)** inner, **(B)** intermediate and **(C)** outer parts of the arena during the novel object task of the non-treated sham (n=8) and non-treated BDL (n=19) groups, at four (1), six (2) and eight (3) weeks after surgery.

* Statistically significant differences between non-treated sham-operated and BDL groups at matched time points ($\boldsymbol{p < 0.05}$)

CHAPTER 5

Discussion and Conclusions

Treatment strategies of HE over the years have been generally based on clinical experience, instead of scientific foundations. Therefore, efficacy and safety are still a matter of debate. It is, however, clear that there is not a miraculous cure and treatment may rely on a conjunct of agents. Among them, VSL#3® and Cr arose recently as promising treatment options for CHE.

To the best of our knowledge, this is the first time that studies on efficacies of VSL#3® and Cr are carried out in a rat model of CHE, through a longitudinal study of brain metabolism. Concerning VSL#3®, only one study has been performed so far in BDL rats, which was confined to assessing the effects of VSL#3® in endothelial dysfunction (Rashid et al., 2014). Regarding Cr, studies have been carried out in an *in vitro* model of cultured embryonic rat brain cell aggregates (Braissant et al., 2008). Furthermore, except for studies carried out in CIBM/LIFMET, only one longitudinal MRS study was performed in BDL rats to investigate brain edema in liver failure (Chavarria et al., 2013). However, it was performed at lower magnetic field strength (7T), reporting changes in very few metabolites, and only between four and six weeks after bile duct ligation.

The present thesis is, therefore, based on two pertinent and preliminary studies, which may contribute to the definition of a new and more satisfactory treatment approach in CHE.

5.1. ^{1}H MRS

5.1.1. Osmoregulation

The present study has indicated a statistically significant increase in brain Gln concentration, accompanied by significant decreases (Ins and Tau in the VSL#3®-treated group; Ins and tCho in the Cr-treated group) and trends of decrease (tCho and Cr in the VSL#3®-treated group; Cr in the Cr-treated group) in brain osmolyte concentration within BDL groups. The substantial increase in Gln concentration levels coupled with the constant total concentration of osmolytes (Gln, Tau, Ins, tCho and Cr) indicates that there is an osmoregulatory response proportional to the augmentation in Gln concentration, as expected to compensate for the osmotic imbalance induced by astrocytic Gln accumulation due to ammonia detoxification in these cells, as previously reported (Heins and Zwingmann, 2010; Cudalbu, 2013). Moreover, Ins seems to be the osmolyte showing the most important decrease as a compensatory effect for the Gln increase, which is in accordance with previously published data (Laubenberger et al., 1997; Cudalbu, 2013).

Cr is involved in energy metabolism, but recently its involvement in osmoregulation and neuroprotection was reported (Braissant, 2010a). The Cr decrease was more evident in the VSL#3®-treated group, as expected due to Cr supplementation to the other group. The decrease of Cr concentration is in agreement with results obtained by the group of Prof. Olivier Braissant in brain cell 3D cultures under hypperammonemia (Braissant et al., 2008).

5.1.2. Neurotransmission

A statistically significant reduction in Glu concentration was observed, accompanied by a trend of decrease for Asp in both VSL#3® and Cr-treated

groups of animals. As mentioned in Chapter 1, hyperammonemia induces alterations in neurotransmission. Furthermore, an adequate supply of the neurotransmitter Glu is maintained in the CNS by the Glu – Gln cycle: Gln effluxes from astrocytes and enters neurons through the Gln transporter (SNAT) where it is hydrolyzed in mitochondria by PAG to yield Glu; Glu is released by neurons and taken up by astrocytes via the glutamate transporter (GLT-1), thus completing the cycle. This decrease observed in Glu may, therefore, underlie an alteration in the efflux of Gln from astrocytes, through a partial suppression of SNAT, as previously shown for acute HE (Kanamori and Ross, 2005). Moreover, chronic hyperammonemia inactivates the GLT-1 in astrocytes (Albrecht and Jones, 1999), resulting in increased extracellular Glu. Collectively, these factors may interfere with Glu synthesis.

5.1.3. Antioxidant Metabolism

Longitudinal decreases were registered for GSH in the Cr-treated group and for Asc in both groups of treatment. In fact, a diminution in antioxidants correlates with the potential presence of oxidative stress due to ammonia exposure, as previously noticed (Braissant, 2010b; Bosoi et al., 2012).

5.1.4. Energy Metabolism

Statistically significant decreases of Glc were longitudinally reported in both groups of treatment, being in accordance with Glc measurements performed in blood samples throughout the study.

Furthermore, in the VSL#3®-treated group, overall trends of decrease for PCr and Ala concentrations were observed; for the Cr-treated group, a statistically significant decrease of PCr was longitudinally noticed, accompanied by a statistically significant increase of Lac concentrations.

Accordingly, cerebral energy metabolism might be altered in chronic models of HE and hyperammonemia and MPT seems to play a crucial role in the bioenergetic failure associated with HE and hyperammonemia (Rama Rao and Norenberg, 2012). Further studies are needed in order to establish the potential role of energy dysfunction in BDL rats.

This thesis relies on two pivotal studies and, therefore, they were designed based on a small sample of animals. The low number of sham-operated rats underlies the lack of statistical significance that was generally observed when comparing BDL and sham-operated groups at later time points.

In the case of the VSL#3® treated group and in addition to the small sample size, we had a high mortality rate throughout the study; due to cirrhotic complications, we obtained a 25% mortality rate at seven weeks after surgery and a 50% of mortality at the eighth week in the BDL group, which significantly reduced the sample size.

Moreover, high CRLBs were obtained specially for low concentrated and overlapping metabolite resonances. In those cases quantification is difficult and may lead to unexpected results, especially for small sample studies. Hence, future studies are needed to validate some measurements.

Treatments were further compared with previously obtained results in BDL rats without treatment, at matched time-points. Figure 39 and Figure 40 compare brain metabolisms of all BDL rats treated with VSL#3® and BDL rats without treatment at, respectively, scans 6 and 8. Figure 41 and Figure 42 represent the same, but for the Cr-treated group. No statistically significant differences were obtained between treatment and no treatment groups. However and at scan 6, animals treated with Cr seemed to show better response to the treatment, represented by a slightly smaller increase in Gln, in comparison with non-treated animals.

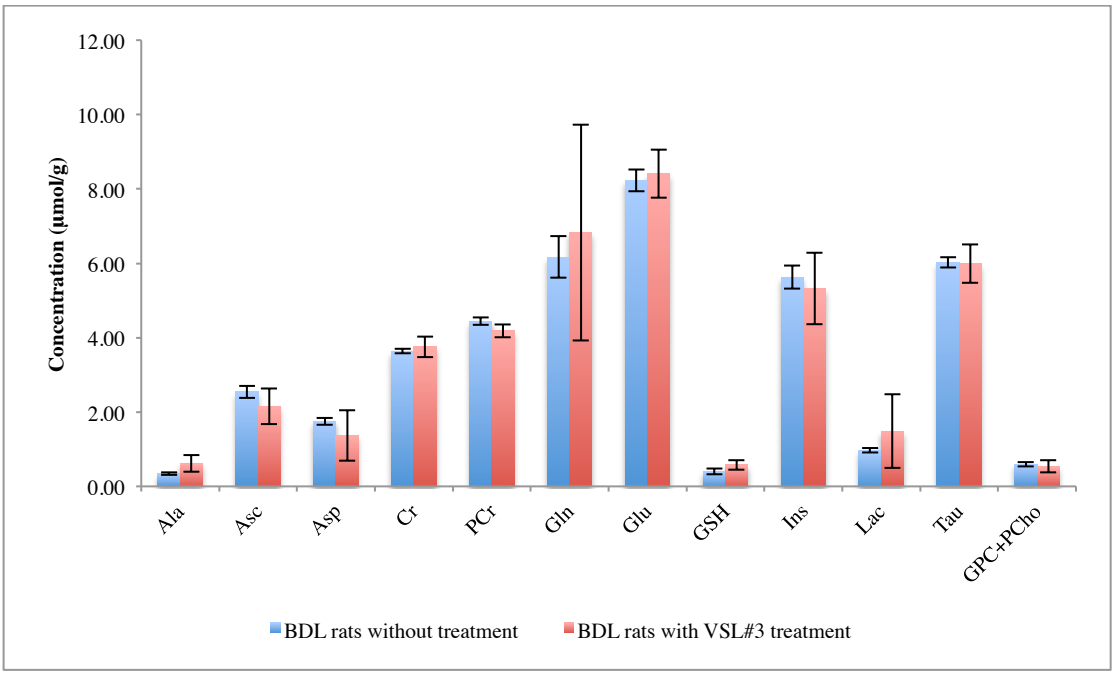

Figure 39 - Brain metabolism comparison between all BDL rats treated with VSL#3® (n=4) and BDL rats without treatment (n=10) at scan 6. Bars represent de mean value ± standard deviation.

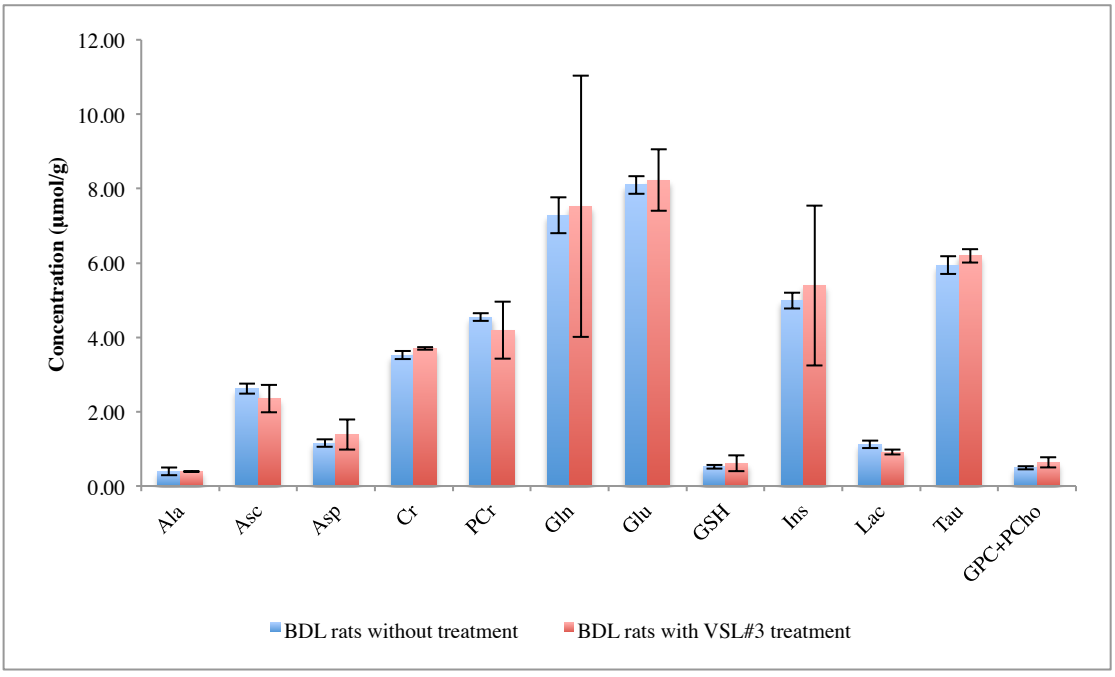

Figure 40 - Brain metabolism comparison between all BDL rats treated with VSL#3® (n=2) and BDL rats without treatment (n=10) at scan 8. Bars represent de mean value ± standard deviation.

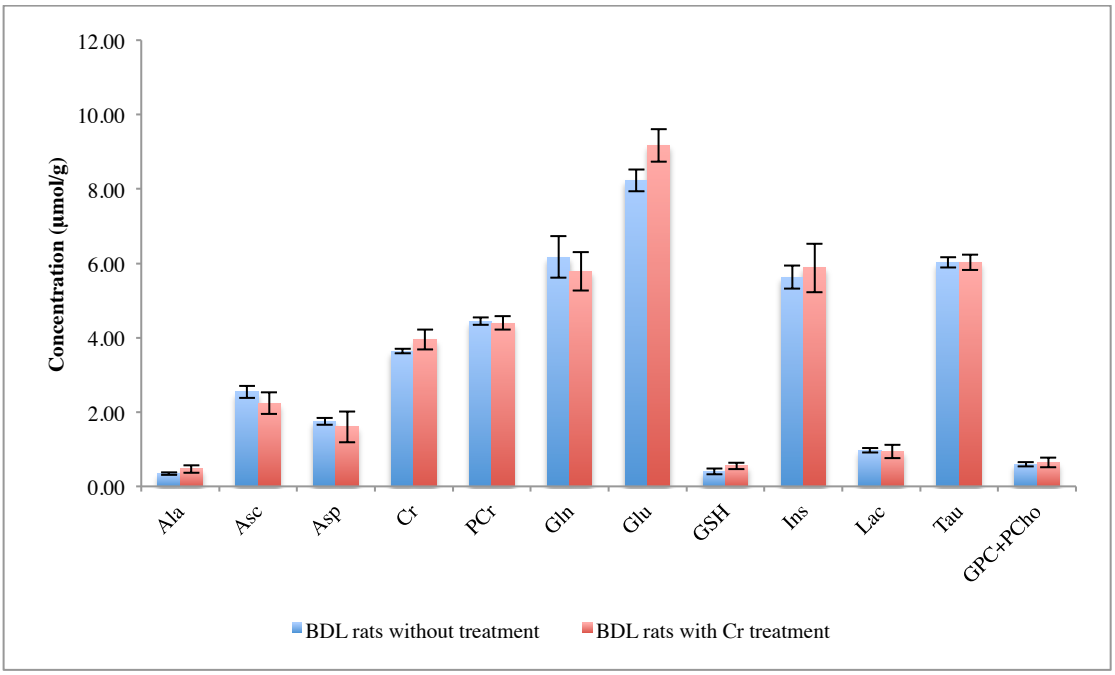

Figure 41 - Brain metabolism comparison between all BDL rats treated with Cr (n=5) and BDL rats without treatment (n=10) at scan 6. Bars represent de mean value ± standard deviation.

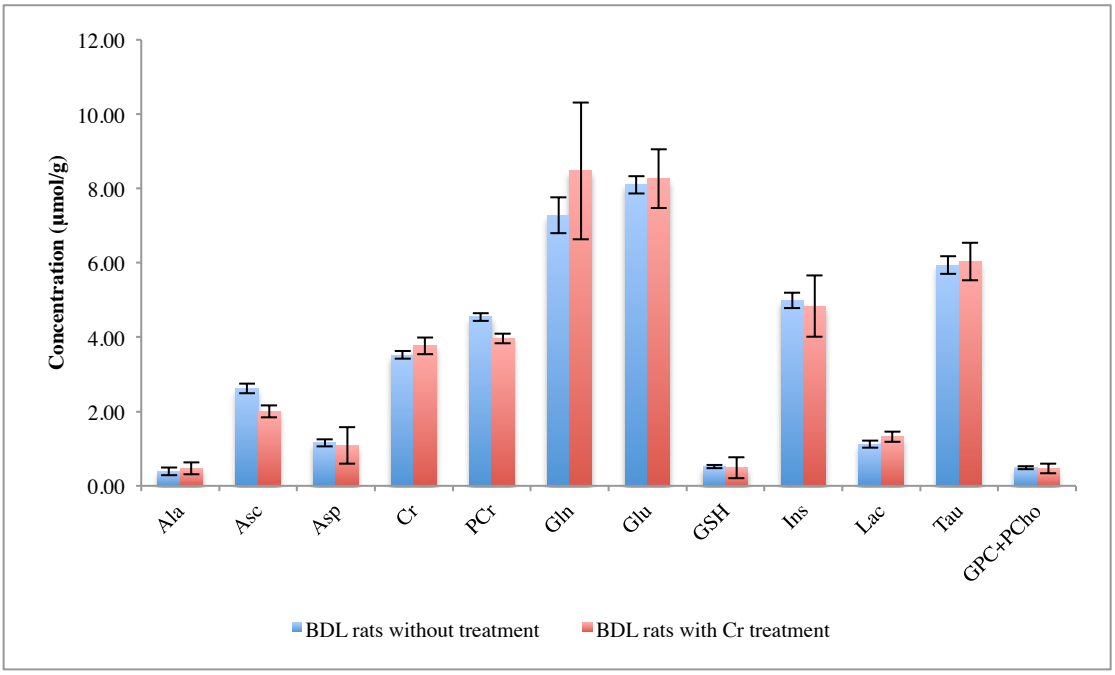

Figure 42 - Brain metabolism comparison between all BDL rats treated with Cr (n=5) and BDL rats without treatment (n=10) at scan 8. Bars represent de mean value ± standard deviation.

5.2. Treatment with VSL#3®

Due to the small number of animals in the VSL#3® treated group, no statistically significant difference was noticed. In addition, a big variability in the animals' response to VSL#3® was noticed (i.e. the increase of Gln concentration ranged from 5 to 10 mmol). Therefore, for now on, we will discuss the results obtained at six weeks after surgery, when all the animals were still alive. From these data (values at six weeks after bile duct ligation) we can notice that BDL rats that drank more also survived longer: BDL 139 and BDL 141. These two rats also had smaller brain Gln concentrations at six weeks after bile duct ligation. We also noticed that, at the beginning of the treatment, animals drank slightly more than they were supposed to – the amount of water was supposed to be 10 ml/100 g of weight. But at the end of the study the animals drank only the necessary or even maybe less, based on their weight. This might suggest that the dose should be increased for the next group of rats.

5.3. Treatment with Cr

Apparently, Cr exerted a neuroprotective effect at scan 6, when the reported brain Gln concentrations were slightly lower than the ones obtained in the non-treated BDL group. However, this beneficial effect was not evident at scan 8. Animals consumed, in average, the Cr dose expected: between 15 and 25 grams or 5% of its body weight per day. However, BDL animals coincidently reduced their diet intake from week six until the end of the study. This preliminary study helped us in elucidating an important number of issues related to the planning of the study (diet intake, etc.) and showed promising results related to the neuroprotective role of Cr in BDL rats, however the number of rats has to be increased in future experiments.

5.4. Behavioral Tests

Due to the small sample size, we didn't obtain statistically significant results with treatments, since high standard deviations were observed. However, from previously performed behavioral tests in a bigger sample, one can note a lower locomotor activity (deduced from lower distance moved and time spent under movement, and higher time spent immobile) and higher anxiety status (lower time spent in the inner part of the arena and higher time spent in the outer part) of BDL rats in comparison with sham-operated rats.

5.5. Pinworms

During these studies, an unexpected pinworm infection was detected in the rats of CIBM. Therefore, a post-mortem direct examination of the caecum and colon content, using warm saline, a technique found in literature (Effler et al., 2008), allowed the observation of adult pinworms in 75% of the rats treated with VSL#3®, and 100% treated with Cr. This might have influence the results obtained, since pinworms highly influence immunologic and nutrients absorption parameters.

In conclusion, we characterized for the first time the *in vivo* and longitudinal progression of VSL#3® and Cr treatments for HE in a model of CLD using ^{1}H MRS. Our preliminary results are promising, showing the feasibility of the study and opening the way to improve our experimental protocol. To increase the number of animals and the VSL#3® dose, as well as give the treatment through gavation to assure that all the animals consume the same amount are possible protocol ameliorations for future new and more precise measurements.

REFERENCES

Albrecht J, Jones EA (1999) Hepatic encephalopathy: molecular mechanisms underlying the clinical syndrome. J Neurol Sci 170:138–146.

Albrecht J, Norenberg MD (2006) Glutamine: a Trojan horse in ammonia neurotoxicity. Hepatology (Baltimore, Md) 44:788-794.

Almeida LS, Salomons GS, Hogenboom F, Jakobs C, Schoffelmeer AN (2006) Exocytotic release of creatine in rat brain. Synapse (New York, NY) 60:118-123.

Als-Nielsen B, Gluud LL, Gluud C (2004a) Benzodiazepine receptor antagonists for hepatic encephalopathy. The Cochrane database of systematic reviews Cd002798.

Als-Nielsen B, Gluud LL, Gluud C (2004b) Nonabsorbable disaccharides for hepatic encephalopathy. The Cochrane database of systematic reviews Cd003044.

Amodio P, Bemeur C, Butterworth R, Cordoba J, Kato A, Montagnese S, Uribe M, Vilstrup H, Morgan MY (2013) The nutritional management of hepatic encephalopathy in patients with cirrhosis: International Society for Hepatic Encephalopathy and Nitrogen Metabolism Consensus. Hepatology (Baltimore, Md) 58:325-336.

Bai M, Yang Z, Qi X, Fan D, Han G (2013) l-ornithine-l-aspartate for hepatic encephalopathy in patients with cirrhosis: a meta-analysis of randomized controlled trials. Journal of gastroenterology and hepatology 28:783-792.

Bajaj JS, Heuman DM, Wade JB, Gibson DP, Saeian K, Wegelin JA, Hafeezullah M, Bell DE, Sterling RK, Stravitz RT, Fuchs M, Luketic V, Sanyal AJ (2011) Rifaximin Improves Driving Simulator Performance in a Randomized Trial of Patients With Minimal Hepatic Encephalopathy. Gastroenterology 140:478-487.e471.

Bajaj JS, Heuman DM, Hylemon PB, Sanyal AJ, White MB, Monteith P, Noble NA, Unser AB, Daita K, Fisher AR, Sikaroodi M, Gillevet PM (2014) Altered profile of human gut microbiome is associated with cirrhosis and its complications. J Hepatol 60:940–947.

Balasubramaniyan V, Wright G, Sharma V, Davies NA, Sharifi Y, Habtesion A, Mookerjee RP, Jalan R (2012) Ammonia reduction with ornithine phenylacetate restores brain eNOS activity via the DDAH-ADMA pathway in bile duct-ligated cirrhotic rats. American journal of physiology Gastrointestinal and liver physiology 302:G145-152.

Bass NM, Mullen KD, Sanyal A, Poordad F, Neff G, Leevy CB, Sigal S, Sheikh MY, Beavers K, Frederick T, Teperman L, Hillebrand D, Huang S, Merchant K, Shaw A, Bortey E, Forbes WP (2010) Rifaximin treatment in hepatic encephalopathy. The New England journal of medicine 362:1071-1081.

Blei AT, Cordoba J (2001) Hepatic Encephalopathy. The American journal of gastroenterology 96:1968-1976.

Bosoi CR, Parent-Robitaille C, Anderson K, Tremblay M, Rose CF (2011) AST-120 (spherical carbon adsorbent) lowers ammonia levels and attenuates brain edema in bile duct-ligated rats. Hepatology (Baltimore, Md) 53:1995-2002.

Bosoi CR, Yang X, Huynh J, Parent-Robitaille C, Jiang W, Tremblay M, Rose CF (2012) Systemic oxidative stress is implicated in the pathogenesis of brain edema in rats with chronic liver failure. Free radical biology & medicine 52:1228-1235.

Bothwell JH, Styles P, Bhakoo KK (2002) Swelling-activated taurine and creatine effluxes from rat cortical astrocytes are pharmacologically distinct. The Journal of membrane biology 185:157-164.

Braissant O, Henry H, Villard AM, Zurich MG, Loup M, Eilers B, Parlascino G, Matter E, Boulat O, Honegger P, Bachmann C (2002) Ammonium-induced impairment of axonal growth is prevented through glial creatine. The Journal of neuroscience: the official journal of the Society for Neuroscience 22:9810-9820.

Braissant O, Cagnon L, Monnet-Tschudi F, Speer O, Wallimann T, Honegger P, Henry H (2008) Ammonium alters creatine transport and synthesis in a 3D culture of developing brain cells, resulting in secondary cerebral creatine deficiency. The European journal of neuroscience 27:1673-1685.

Braissant O (2010a) Ammonia toxicity to the brain: Effects on creatine metabolism and transport and protective roles of creatine. Mol Genet Metab 100, Suppl:S53–S58.

Braissant O (2010b) Current concepts in the pathogenesis of urea cycle disorders. Mol Genet Metab 100:S3–S12.

Braissant O, McLin VA, Cudalbu C (2013) Ammonia toxicity to the brain. Journal of inherited metabolic disease 36:595-612.

Brigidi P, Swennen E, Vitali B, Rossi M, Matteuzzi D (2003) PCR detection of Bifidobacterium strains and Streptococcus thermophilus in feces of human subjects after oral bacteriotherapy and yogurt consumption. International journal of food microbiology 81:203-209.

Brusilow SW, Koehler RC, Traystman RJ, Cooper AJ (2010) Astrocyte glutamine synthetase: importance in hyperammonemic syndromes and potential target for therapy. Neurotherapeutics : the journal of the American Society for Experimental NeuroTherapeutics 7:452-470.

Butterworth RF, Norenberg MD, Felipo V, Ferenci P, Albrecht J, Blei AT (2009) Experimental models of hepatic encephalopathy: ISHEN guidelines. Liver international : official journal of the International Association for the Study of the Liver 29:783-788.

Cauli O, Llansola M, Erceg S, Felipo V (2006) Hypolocomotion in rats with chronic liver failure is due to increased glutamate and activation of metabotropic glutamate receptors in substantia nigra. Journal of hepatology 45:654-661.

Chang B, Sang L, Wang Y, Tong J, Zhang D, Wang B (2013) The protective effect of VSL#3 on intestinal permeability in a rat model of alcoholic intestinal injury. BMC gastroenterology 13:151.

Chavarria L, Oria M, Romero-Gimenez J, Alonso J, Lope-Piedrafita S, Cordoba J (2013) Brain magnetic resonance in experimental acute-on-chronic liver failure. Liver international : official journal of the International Association for the Study of the Liver 33:294-300.

Chavez-Tapia N, Cesar-Arce A, Barrientos-Gutierrez T, Villegas-Lopez F, Mendez-Sanchez N, Uribe M (2013) A systematic review and meta-analysis of the use of oral zinc in the treatment of hepatic encephalopathy. Nutrition Journal 12:74.

Chermesh I, Eliakim R (2006) Probiotics and the gastrointestinal tract: where are we in 2005? World journal of gastroenterology : WJG 12:853-857.

Cudalbu CR, Braissant O, Lepore M, Gruetter R, McLin V (2012) Brain osmolytes and brain edema in a rat model of chronic liver failure: in vivo longitudinal 1H Spectroscopic imaging and Diffusion tensor imaging studies at 9.4T. In: The 15th International Society of Hepatic Encephalopathy and Nitrogen Metabolism, Symposium May 29 - June 2, 2012, Denmark.

Cudalbu C (2013) In vivo studies of brain metabolism in animal models of Hepatic Encephalopathy using 1H Magnetic Resonance Spectroscopy. Metab Brain Dis 28:167-174.

de Graaf RA (2008) In vivo NMR spectroscopy: principles and techniques. John Wiley & Sons.

Desjardins P, Du T, Jiang W, Peng L, Butterworth RF (2012) Pathogenesis of hepatic encephalopathy and brain edema in acute liver failure: role of glutamine redefined. Neurochemistry international 60:690-696.

Dhiman RK (2013) Gut microbiota and hepatic encephalopathy. Metab Brain Dis 28:321-326.

Ding X, Zhang F, Wang Y (2014) Letter: probiotics vs. lactulose for minimal hepatic encephalopathy therapy. Alimentary pharmacology & therapeutics 39:1000-1000.

Effler JC, Hickman-Davis JM, Erwin JG, Cartner SC, Schoeb TR (2008) Comparison of methods for detection of pinworms in mice and rats. Lab Anim (NY) 37:210–215.

Ferenci P, Lockwood A, Mullen K, Tarter R, Weissenborn K, Blei AT (2002) Hepatic encephalopathy--definition, nomenclature, diagnosis, and quantification: final report of the working party at the 11th World Congresses of Gastroenterology, Vienna, 1998. Hepatology (Baltimore, Md) 35:716-721.

Gluud LL, Dam G, Borre M, Les I, Cordoba J, Marchesini G, Aagaard NK, Risum N, Vilstrup H (2013a) Oral branched-chain amino acids have a beneficial effect on manifestations of hepatic encephalopathy in a systematic review with meta-analyses of randomized controlled trials. The Journal of nutrition 143:1263-1268.

Gluud LL, Dam G, Borre M, Les I, Cordoba J, Marchesini G, Aagaard NK, Vilstrup H (2013b) Lactulose, rifaximin or branched chain amino acids for hepatic encephalopathy: what is the evidence? Metab Brain Dis 28:221-225.

Gruetter R (1993) Automatic, localized in Vivo adjustment of all first-and second-order shim coils. Magn Reson Med 29:804–811.

Gruetter R, Tkáč I (2000) Field mapping without reference scan using asymmetric echo-planar techniques. Magn Reson Med 43:319–323.

Hassanein TI, Tofteng F, Brown RS, Jr., McGuire B, Lynch P, Mehta R, Larsen FS, Gornbein J, Stange J, Blei AT (2007) Randomized controlled study of extracorporeal albumin dialysis for hepatic encephalopathy in advanced cirrhosis. Hepatology (Baltimore, Md) 46:1853-1862.

Heins J, Zwingmann C (2010) Organic osmolytes in hyponatremia and ammonia toxicity. Metab Brain Dis 25:81–89.

Holmes E, Kinross J, Gibson GR, Burcelin R, Jia W, Pettersson S, Nicholson JK (2012) Therapeutic modulation of microbiota-host metabolic interactions. Science translational medicine 4:137rv136.

Homayouni Rad A, Torab R, Ghalibaf M, Norouzi S, Mehrabany EV (2013) Might patients with immune-related diseases benefit from probiotics? Nutrition 29:583-586.

Imani Fooladi AA, Mahmoodzadeh Hosseini H, Nourani MR, Khani S, Alavian SM (2013) Probiotic as a novel treatment strategy against liver disease. Hepatitis monthly 13:e7521.

Jiang Q, Jiang G, Shi KQ, Cai H, Wang YX, Zheng MH (2013) Oral acetyl-L-carnitine treatment in hepatic encephalopathy: view of evidence-based medicine. Annals of hepatology 12:803-809.

Jones EA, Weissenborn K (1997) Neurology and the liver. Journal of Neurology, Neurosurgery & Psychiatry 63:279-293.

Jover-Cobos M, Noiret L, Lee K, Sharma V, Habtesion A, Romero-Gomez M, Davies N, Jalan R (2014) Ornithine phenylacetate targets alterations in the expression and activity of glutamine synthase and glutaminase to reduce ammonia levels in bile duct ligated rats. Journal of hepatology 60:545-553.

Jover-Cobos M, Noiret L, Sharifi Y, Jalan R (2013) Ornithine phenylacetate revisited. Metab Brain Dis 28:327-331.

Junker AE, Als-Nielsen B, Gluud C, Gluud LL (2014) Dopamine agents for hepatic encephalopathy. The Cochrane database of systematic reviews 2:Cd003047.

Kanamori K, Ross BD (2005) Suppression of glial glutamine release to the extracellular fluid studied in vivo by NMR and microdialysis in hyperammonemic rat brain. Journal of neurochemistry 94:74-85.

Klein AM, Ferrante RJ (2007) The neuroprotective role of creatine. Sub-cellular biochemistry 46:205-243.

Kunz N (2010) Biophysical Basis of the Diffusion-Weighted Magnetic Resonance Signal in the Rat Brain.

Lanz B (2012) Mathematical Modeling of Brain Energy Metabolism, Measured with PET and MRS in Rodents.

Laubenberger J, Haussinger D, Bayer S, Gufler H, Hennig J, Langer M (1997) Proton magnetic resonance spectroscopy of the brain in symptomatic and asymptomatic patients with liver cirrhosis. Gastroenterology 112:1610-1616.

Leke R, de Oliveira DL, Mussulini BH, Pereira MS, Kazlauckas V, Mazzini G, Hartmann CR, Silveira TR, Simonsen M, Bak LK, Waagepetersen HS, Keiding S, Schousboe A, Portela LV (2012) Impairment of the organization of locomotor and exploratory behaviors in bile duct-ligated rats. PloS one 7:e36322.

Leke R, Oliveira DL, Forgiarini LF, Escobar TD, Hammes TO, Meyer FS, Keiding S, Silveira TR, Schousboe A (2013) Impairment of short term memory in rats with hepatic encephalopathy due to bile duct ligation. Metab Brain Dis 28:187-192.

Lighthouse J, Naito Y, Helmy A, Hotten P, Fuji H, Min CH, Yoshioka M, Marotta F (2004) Endotoxinemia and benzodiazepine-like substances in compensated cirrhotic patients: a randomized study comparing the effect of rifaximine alone and in association with a symbiotic preparation. Hepatology research : the official journal of the Japan Society of Hepatology 28:155-160.

Lunia MK, Sharma BC, Sharma P, Sachdeva S, Srivastava S (2014) Probiotics prevent hepatic encephalopathy in patients with cirrhosis: a randomized controlled trial. Clinical gastroenterology and hepatology : the official clinical practice journal of the American Gastroenterological Association 12:1003-1008.e1001.

Malaguarnera M, Gargante MP, Cristaldi E, Vacante M, Risino C, Cammalleri L, Pennisi G, Rampello L (2008) Acetyl-L-carnitine treatment in minimal hepatic encephalopathy. Digestive diseases and sciences 53:3018-3025.

Malaguarnera M, Bella R, Vacante M, Giordano M, Malaguarnera G, Gargante MP, Motta M, Mistretta A, Rampello L, Pennisi G (2011) Acetyl-L-carnitine reduces depression and improves quality of life in patients with minimal hepatic encephalopathy. Scandinavian journal of gastroenterology 46:750-759.

Manning TS, Gibson GR (2004) Prebiotics. Best Practice & Research Clinical Gastroenterology 18:287-298.

McGee RG, Bakens A, Wiley K, Riordan SM, Webster AC (2011) Probiotics for patients with hepatic encephalopathy. The Cochrane database of systematic reviews Cd008716.

Misel ML, Gish RG, Patton H, Mendler M (2013) Sodium benzoate for treatment of hepatic encephalopathy. Gastroenterology & hepatology 9:219-227.

Mlynárik V, Gambarota G, Frenkel H, Gruetter R (2006) Localized short-echo-time proton MR spectroscopy with full signal-intensity acquisition. Magn Reson Med 56:965–970.

Morgan M, Blei A, Grüngreiff K, Jalan R, Kircheis G, Marchesini G, Riggio O, Weissenborn K (2007) The treatment of hepatic encephalopathy. Metab Brain Dis 22:389-405.

Mountzouris KC, McCartney AL, Gibson GR (2002) Intestinal microflora of human infants and current trends for its nutritional modulation. The British journal of nutrition 87:405-420.

Nicholson JK, Holmes E, Kinross J, Burcelin R, Gibson G, Jia W, Pettersson S (2012) Host-Gut Microbiota Metabolic Interactions. Science 336:1262-1267.

Norenberg MD, Rao KVR, Jayakumar AR (2005) Mechanisms of Ammonia-Induced Astrocyte Swelling. Metab Brain Dis 20:303-318.

Phillips GB, Schwartz R, Gabuzda GJ, Davidson CS (1952) The Syndrome of Impending Hepatic Coma in Patients with Cirrhosis of the Liver Given Certain Nitrogenous Substances. New England Journal of Medicine 247:239-246.

Pockros P, Hassanein T, Vierling J, Heuman D, Hillebrand D, Chojkier M, Resler M, LaPlaca C, Harris M (2009) 105 phase 2, multicenter, randomized study of ast-120 (spherical carbon adsorbent) vs. lactulose in the treatment of low-grade hepatic encephalopathy (he). J Hepatol 50:S43–S44.

Provencher SW (2001) Automatic quantitation of localized in vivo1H spectra with LCModel. NMR Biomed 14:260–264.

Rae CD (2014) A guide to the metabolic pathways and function of metabolites observed in human brain 1H magnetic resonance spectra. Neurochem Res 39:1–36.

Rama Rao KV, Norenberg MD (2012) Brain energy metabolism and mitochondrial dysfunction in acute and chronic hepatic encephalopathy. Neurochem Int 60:697–706.

Rama Rao KV, Jayakumar AR, Norenberg MD (2012) Glutamine in the pathogenesis of acute hepatic encephalopathy. Neurochemistry international 61:575-580.

Rashid SK, Khodja NI, Auger C, Alhosin M, Boehm N, Oswald-Mammosser M, Schini-Kerth VB (2014) Probiotics (VSL#3) prevent endothelial dysfunction in rats with portal hypertension: role of the angiotensin system. PloS one 9:e97458.

Rodrigo R, Monfort P, Cauli O, Erceg S, Felipo V (2006) Pharmacological manipulation of cyclic GMP levels in brain restores learning ability in animal models of hepatic encephalopathy: therapeutic implications. Neuropsychiatric disease and treatment 2:53-63.

Rose CF (2014) Ammonia: more than a neurotoxin? Liver International 34:649-651.

Sanchez E, Nieto JC, Boullosa A, Vidal S, Sancho FJ, Rossi G, Sancho-Bru P, Oms R, Mirelis B, Juarez C, Guarner C, Soriano G (2014) VSL#3 probiotic treatment decreases bacterial translocation in rats with carbon tetrachloride-induced cirrhosis. Liver international : official journal of the International Association for the Study of the Liver.

Sanders ME (2003) Probiotics: considerations for human health. Nutrition reviews 61:91-99.

Sanyal A, Younossi ZM, Bass NM, Mullen KD, Poordad F, Brown RS, Vemuru RP, Mazen Jamal M, Huang S, Merchant K, Bortey E, Forbes WP (2011) Randomised clinical trial: rifaximin improves health-related quality of life in cirrhotic patients with hepatic encephalopathy - a double-blind placebo-controlled study. Alimentary pharmacology & therapeutics 34:853-861.

Schuppan D, Afdhal NH (2008) Liver cirrhosis. Lancet 371:838-851.

Sekhar MS, Unnikrishnan MK, Rodrigues GS, Mukhopadhyay C (2013) Synbiotic formulation of probiotic and lactulose combination for hepatic encephalopathy treatment: a realistic hope? Medical hypotheses 81:167-168.

Sestili P, Martinelli C, Colombo E, Barbieri E, Potenza L, Sartini S, Fimognari C (2011) Creatine as an antioxidant. Amino acids 40:1385-1396.

Shawcross DL, Balata S, Olde Damink SWM, Hayes PC, Wardlaw J, Marshall I, Deutz NEP, Williams R, Jalan R (2004) Low myo-inositol and high glutamine levels in brain are associated with neuropsychological deterioration after induced hyperammonemia.

Shukla S, Shukla A, Mehboob S, Guha S (2011) Meta-analysis: the effects of gut flora modulation using prebiotics, probiotics and synbiotics on minimal hepatic encephalopathy. Alimentary pharmacology & therapeutics 33:662-671.

Shukla S, Mahl TC, Guha S (2014) Letter: probiotics vs. lactulose for minimal hepatic encephalopathy therapy--authors' reply. Alimentary pharmacology & therapeutics 39:1001.

Sidhu SS, Goyal O, Mishra BP, Sood A, Chhina RS, Soni RK (2011) Rifaximin improves psychometric performance and health-related quality of life in patients with minimal hepatic encephalopathy (the RIME Trial). The American journal of gastroenterology 106:307-316.

Solga S (2003) Probiotics can treat hepatic encephalopathy. Medical hypotheses 61:307-313.

Tajiri K, Shimizu Y (2013) Branched-chain amino acids in liver diseases. World journal of gastroenterology : WJG 19:7620-7629.

Therrien G, Rose C, Butterworth J, Butterworth RF (1997) Protective effect of L-carnitine in ammonia-precipitated encephalopathy in the portacaval shunted rat. Hepatology (Baltimore, Md) 25:551-556.

Tranah TH, Vijay GK, Ryan JM, Shawcross DL (2013) Systemic inflammation and ammonia in hepatic encephalopathy. Metab Brain Dis 28:1-5.

Vogels BA, Maas MA, Daalhuisen J, Quack G, Chamuleau RA (1997) Memantine, a noncompetitive NMDA receptor antagonist improves hyperammonemia-induced encephalopathy and acute hepatic encephalopathy in rats. Hepatology (Baltimore, Md) 25:820-827.

Wright G, Vairappan B, Stadlbauer V, Mookerjee RP, Davies NA, Jalan R (2012) Reduction in hyperammonaemia by ornithine phenylacetate prevents lipopolysaccharide-induced brain edema and coma in cirrhotic rats. Liver international : official journal of the International Association for the Study of the Liver 32:410-419.